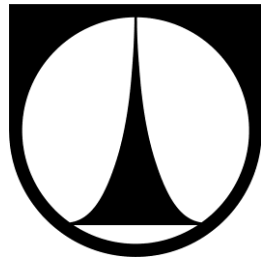


TECHNICKÁ UNIVERZITA V LIBERCI
HOCHSCHULE ZITTAU/GÖRLITZ
FRAUNHOFER INSTITUTE FÜR SOLARE
ENERGIESYSTEME ISE



DIPLOMA THESIS

**FEM modeling of astigmatism corrected heliostat with
deflectometry validation**

Bc. Alexey Kruchenko

TECHNICAL UNIVERISTY OF LIBEREC

Faculty of Mechatronics, Informatics and Interdisciplinary Studies

Study program: N2612 – Electrical engineering and informatics

Field of study: 3906T001 – Mechatronics

HOCHSCHULE ZITTAU / GÖRLITZ

Faculty of Electrical Engineering and Computer Sciences

Study course: Mechatronics

Registration no.: 207016

FEM modeling of astigmatism corrected heliostat with deflectometry validation

Diploma thesis

Author: **Bc. Alexey Kruchenko**

Scientific supervisor: MSc. De Wet van Rooyen (Fraunhofer ISE)

Second supervisor: Prof. Dr. rer. nat Stefan Bischoff (Hochschule Zittau/Görlitz)

Consultant: MSc. Gregor Bern (Fraunhofer ISE)

DIPLOMA THESIS ASSIGNMENT

(PROJECT, ART WORK, ART PERFORMANCE)

First name and surname: **Bc. Alexey Kruchenko**
Study program: **N2612 Electrical Engineering and Informatics**
Identification number: **M12000269**
Specialization: **Mechatronics**
Topic name: **FEM modeling of astigmatism corrected heliostat with deflectometry validation**
Assigning department: **Institute of Mechatronics and Computer Engineering**

Rules for elaboration:

Goal:

In a novel heliostat development project at Fraunhofer ISE a reflector material sheet is required which can withstand continuous elastic deformation in 2 dimensions to various extents. This improved heliostat device will lead to a focal spot of higher concentration (lower diameter) independent of the direction on solar incidence. Within the project several heliostat prototypes will be constructed in laboratory scale.

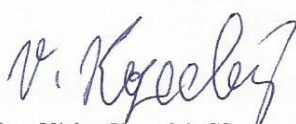
Assignment:

1. Familiarization with basic principles of the heliostat.
2. Implementation of mathematical model of reflective surface of the heliostat for astigmatism effect elimination.
3. FEM modeling of elastic deformation of heliostat's mirror plate.
4. Installation of heliostat prototype on basis of results obtained from FEM model optimization.
5. Development of photogrammetry principle for evaluation of deformed shape of reflective surface of the heliostat prototype.
6. Performing the validation of shape deformation of the prototype with use of deflectometry technique and implemented photogrammetry algorithm.
7. Data management and comparison of measured and FEM simulated results with theoretical approximation.
8. Documentation of performed analysis.


Scope of graphic works: **In respect to the documentation needs**
Scope of work report
(scope of dissertation): **c. 40–50 pages**
Form of dissertation elaboration: **printed/electronical**
Language of dissertation elaboration: **English**
List of specialized literature:

- [1] **K.-K. Chong and M. H. Tan, "Comparison Study of Two Different Sun-Tracking Methods in Optical Efficiency of Heliostat Field," International Journal of Photoenergy, no. Panagiotis Lianos, 2012.**
- [2] **A. Heimsath, P. Werner, T. Bothe and W. Li, "Characterisation of optical components for linear fresnel collectors by fringe reflection method". 14th Biennal SolarPACES Symposium, 2008.**
- [3] **T. Luhmann, S. Robson, S. Kyle and I. Harley, in Close Range Photogrammetry, Dunbeath, Whittles Publishing, 2006.**
- [4] **J. Duffie, W.A. Beckman, "Solar Engineering of Thermal Processes". Wiley Publishing, 2013, ISBN: 978-0-470-87366-3.**

Tutor for dissertation: **prof. RNDr. Stefan Bischoff**
Hochschule Zittau/Görlitz, IPM, Germany
Dissertation Counsellor: **De Wet Van Rooyen, M.Sc.**
Fraunhofer Institute of Solar Energy Systems, Freiburg,
Germany
Date of dissertation assignment: **10 October 2014**
Date of dissertation submission: **15 May 2015**


prof. Ing. Václav Kopecký, CSc.
Dean




doc. Ing. Milan Kolář, CSc.
Department Manager

Liberec, dated: 10 October 2014

Declaration

I hereby certify that this diploma thesis is my own work and I have written my diploma thesis by myself using literature listed therein and consulting it with my supervisors.

This diploma thesis is part of the Heliopack project of Fraunhofer ISE; the content of this work is therefore confidential. The disclosure or publication of data of Fraunhofer ISE may be prosecuted.

In Liberec 2nd January 2015

Alexey Kruchenko

Acknowledgements

First of all I would like to sincerely thank to my supervisor De Wet van Rooyen. During the thesis work this person taught me many things, which, I am sure, help me in future to succeed in my engineer's activity. It was great pleasure to be your student. Thank you very much, De Wet!

Also, I would like to thank following persons at the Fraunhofer ISE for their help in writing this paper:

Gregor Bern

Marco Perger

Anna Heimsath

I want to convey words of gratitude to students and trainees with whom I worked side by side in Fraunhofer ISE for seven glorious months:

Vidya Shree

Stella Joos

Shaon Sutradhar

I want to thank to Pavel Mokry, a student of whom I was for several years. Thanks to this person, were obtained the knowledge that helped me at certain stages of this work.

To Stefan Bischoff I express appreciation for leading of my diploma thesis.

Last but not least I would like to thank to my whole family for their everyday support. Without you, this work would never have been finalized.

Abstract

A model of a heliostat device is presented in this work. An astigmatism problem, which impacts on efficiency through enlargement of the focal spot at the target in dependence of the incident angle of the sunlight of the heliostat, leads to detrimental effect for high temperature applications. It introduces spillage losses for fixed aperture receivers. In order to combat astigmatism the shape of the heliostat has to change in dependence to the incident angle of the solar radiation on the heliostat, a mathematical model of this shape changing heliostat's reflecting surface is created to avoid such losses and concentrate solar rays in a dense focal spot irrespective of incident angle. A 'target-aligned' tracking method is applicable to this type of heliostat.

With use of finite element method (FEM) a structural mechanics model of the heliostat is designed to compare with the ideal shape requirements described by the mathematical model. The result of comparison of these two models allows it to determine limits in which a heliostat construction has to be deformed.

For determining of quality of heliostat a prototype, which has been dimensioned implementing the FEM model, deflectometry measurements are performed on a constructed prototype. The measurement returns a shape quality and spatial coordinates of reflective surface of the heliostat.

The second technique that is used in heliostat validation is photogrammetry. This technique is able to determine spatial coordinates of marked points on the object of interest with use of image processing.

Keywords: Heliostat, Astigmatism, Target-aligned tracking method, Finite element method (FEM), Photogrammetry, Deflectometry measurement.

Content

Declaration.....	4
Acknowledgements	5
Abstract.....	6
Content.....	7
List of figures	9
List of tables.....	13
Nomenclature	14
List of addendums	17
1 Introduction.....	19
2 Theoretical aspects of the heliostat device	20
2.1 Principle of the heliostat device	20
2.2 Astigmatism	24
2.3 Shape of the reflector	26
2.4 Deformation of reflectors shape.....	32
3 Methods	38
3.1 FEM.....	38
3.1.1 Mesh elements	39
3.1.2 Mechanical properties of solid materials.....	41
3.2 Deflectometry	44
3.3 Photogrammetry.....	46
3.3.1 Camera.....	47
3.3.2 Triangulation.....	48
3.3.3 Resection	49
3.3.4 Bundle adjustment.....	50
4 Implementation	52
4.1 FEM model of heliostat	52
4.1.1 Geometry	52
4.1.2 Material properties	54
4.1.3 Initial physical conditions.....	55
4.1.4 Mesh	57

4.1.5	Post processing.....	58
4.1.6	Parameterization	60
4.2	Deflectometry laboratory.....	62
4.3	Photogrammetry technique implementation.....	63
4.3.1	Algorithm implementation in GUI.....	67
4.3.2	Validation of photogrammetry algorithm functionality	70
5	Analysis of measurements and simulations	74
5.1	Optimization of the model with FEM simulations (prototype model).....	74
5.2	Measurement of quality of the heliostat	79
5.2.1	FRT validation	80
5.2.2	Photogrammetry validation	81
5.3	Comparison of measured and simulated results.....	84
6	Conclusion	88
	Bibliography	90
	Addendum.....	92

List of figures

Figure 1: Concentrating Solar Thermal Power plant installation [2]	20
Figure 2: Illustration of angle of incidence θ on a flat mirror of directed solar radiation .The angle of incidence is always positive and measured from the normal of the surface by definition	21
Figure 3: Fixed horizontal heliostat	22
Figure 4: Azimuth-elevation sun-tracking method [4].....	23
Figure 5: Target-aligned tracking method [4].....	23
Figure 6: Ideal focusing of a concave mirror.....	24
Figure 7: Ray focusing in tangential plane	25
Figure 8: Ray focusing in sagittal plane	25
Figure 9: Astigmatism effect of concave mirror	26
Figure 10: Rotational paraboloid with depicted focal point	27
Figure 11: Schematic representation of reflection of solar ray from the surface of heliostat in tangential plane.....	27
Figure 12: Parabola as a forming of vertical axis of the mirror a). Ellipse as a forming of horizontal axis of the reflector's surface b)	28
Figure 13: Representation of shape of the mirror surface as a segment of a parabola in xz-plane	30
Figure 14: Major diameter of ellipse a). Minor diameter of ellipse b).....	30
Figure 15: Segment of ellipse that presents a shape of the mirror surface in elliptic plane.....	31
Figure 16: Shape of the reflector formed by a few segments of ellipse	32
Figure 17: Shapes of parabolas with respect to incident angle ($\theta_1 = 30^\circ$, $\theta_2 = 45^\circ$, $\theta_3 =$ 60° and slant range $S = 29,15$ m)	33
Figure 18: Center points of the mirror surface for two different parabolas ($\theta_i = 30^\circ$, $\theta_f =$ 45° and slant range $S = 29,15$ m)	33
Figure 19: Placement of parabolas segments at the same center point by rotation of angle γ	34
Figure 20: Deviation of curves in normalized system of coordinates.....	35
Figure 21: Projection of curves on sagittal plane.....	36
Figure 22: Normalized shapes of reflective surface with $\theta = 30^\circ$ a), with $\theta = 60^\circ$ b) ...	36

Figure 23: Physical simulation process [7].....	39
Figure 24: Mesh elements: a) tetrahedral b) hexahedral c) prismatic triangular and d) pyramid	40
Figure 25: Cylindrical shell a) represented by the first b) and the second-order c) Lagrangian element	40
Figure 26: Idealized stress in a straight bar	42
Figure 27: Determination of the strain	42
Figure 28: Example of stress-strain curve	43
Figure 29: Lateral resolution of deflectometry system	44
Figure 30: Measurement principle of deflectometry.....	45
Figure 31: Simplified measurement model (2D) of the FRT setup	45
Figure 32: Principle of photogrammetry.	46
Figure 33: Relationship between chip size, lens focal length and field of view	47
Figure 34: Targeting the objects by pin-hole camera.....	48
Figure 35: Single a) and multiple b) target triangulations.....	49
Figure 36: Coordinate system of camera.....	50
Figure 37: Basic structure of 3D model of the heliostat device.....	52
Figure 38: Frame elements of the heliostat model.....	53
Figure 39: Non-linear elevation axis.....	53
Figure 40: Geometry of mirror plate as a product of intersection of rotational paraboloid and parallelepiped.	54
Figure 41: Geometric domains of the FEM model with assigned materials	55
Figure 42: Direction of applied force and rotation axis of the model.....	55
Figure 43: Ball joint physics (rotation with respect to three degrees for freedom and fixed external boundary)	56
Figure 44: Reflective surface profile a) with force directed toward to the mirror a) from the mirror b)	56
Figure 45: Mesh quality of part of the model	57
Figure 46: Model displacement in Z component	58
Figure 47: Comparison of theoretical (gray) and simulated (pink) surface	59
Figure 48: Normal vectors (blue arrows) of interpolated surface a) and angle difference ω of theoretical (red) and simulated (green) normal vectors at the same point on reflective surface in x and y direction b).	59

Figure 49: Flow chart of Matlab scripting for comparison procedure of surfaces with parameterized model.....	61
Figure 50: Deflectometry measurement setup	62
Figure 51: Relative arrangement of objects of FRT measurement	63
Figure 52: Transformation of 3D coordinates into 2D with use of pinhole camera principle	64
Figure 53: Simplified photogrammetry algorithm	65
Figure 54: Photographing (right) of variously oriented chessboard pattern (left) [19]..	65
Figure 55: Binary coded markers with ID number	66
Figure 56: Example of output results of photogrammetry algorithm (spatial coordinates are given in meters).	67
Figure 57: Detailed structure of photogrammetry algorithm.....	68
Figure 58: Processing of the image in camera calibration	69
Figure 59: Example of an input file for automatic mode of photogrammetry function.	69
Figure 60: Output xml file structure of processed photographs	70
Figure 61: Photogrammetry measurement setup	71
Figure 62: Sketch of marker pattern with circled reference markers. Scale is defined by user-defined units	72
Figure 63: Square cross-sectional profile of the tube.....	75
Figure 64: Tubes with designated cross-sectional module index	75
Figure 65: Maximal and average standard deviations with respect to geometric ratio of cross-sectional modules. Green bars indicate the optimal ratio of maximal and average standard deviations	76
Figure 66: Non-linear axis adjustment. Red orthogonal axes illustrate the center of the central tube and joint axis level. The blue system defines a location of the axis of rotation in rotation rod	77
Figure 67: Dependence of maximal and average standard deviations on increasing distance of rotation bar to the center of the central tube. Green bars indicate the optimal ratio of maximal and average standard deviations	77
Figure 68: Dependence of maximal and average standard deviations on the changing position of rotation bar relative to the level of ball joint axis. Green bars indicate the optimal ratio of maximal and average standard deviations	78
Figure 69: Layout of connectors	79
Figure 70: Heliostat prototype in deflectometry laboratory	80

Figure 71: Registration of the fringe pattern through the prototype reflective surface .	80
Figure 72: Photogrammetry measurement setup. Total station device determines spatial coordinates of reference markers (on the wall and locker).....	82
Figure 73: Example of partially overlapping measurement of segment of the mirror plate.....	83
Figure 74: Difference in standard deviations in x-direction between FEM and FRT validation.....	84
Figure 75: Difference in standard deviations in y-direction between FEM and FRT validation.....	84
Figure 76: Curves of the heliostat surface in sagittal plane (blue) and tangential plane (red) a) circle fit with use of surface curves b)	85
Figure 77: Effective focal length in sagittal plane	86
Figure 78: Effective focal length in tangential plane	86

List of tables

Table 1: Input data for FEM model.....	74
Table 2: Standard deviation of measured specular surface of the heliostat measured with FRT method.....	81

Nomenclature

Greek symbols

α	deg	Angle of ellipse arc
β	deg	Difference angle between initial and final incident angle
γ	deg	Double incident angle
ϵ	-	Mechanical strain
θ	deg	Incident angle
θ_i	deg	Initial incident angle
θ_f	deg	Final incident angle
ν	-	Poisson's ratio
ξ	deg	Angle of incident between camera optical axis and target
σ	GPa	Mechanical stress
σ_{sd}	-	Standard deviation
$\sigma_{sd,avg}$	mrad	Average standard deviation
$\sigma_{sd,max}$	mrad	Maximal standard deviation
$\sigma_{sd,x}$	mrad	Standard deviation of angle difference in x-direction
$\sigma_{sd,y}$	mrad	Standard deviation of angle difference in y-direction
φ	pixel	Sinusoidal pattern phase in pixels
ω_x	deg	Angle difference of normal vectors in x component
ω_y	deg	Angle difference of normal vectors in y component

Latin symbols

A	m ²	Area of straight bar profile
D	m	Distance to the receiver/target
$D_{1,2,3}$	m	Differences between flat and deformed mirror
E	Pa	Young's modulus (elastic modulus)
F	m	Focal length
F_{app}	N	Applied force
$F_{sagittal}$	m	Focal length in sagittal plane

$F_{tangential}$	m	Focal length in tangential plane
H	m	Height to the receiver/target
L	m	Mirror length in tangential and sagittal plane
$L_{1,2}$	m	Distances between connectors
R	m	Circle fit radius
S	m	Slant range
W	mm	Tube width
Z	m ³	Cross-section modulus
a	m	Major ellipse radius
b	m	Minor ellipse radius
c	mm	Width of tube cavity
d	mm	Distance from camera to target
d_1	mm	Distance of rotation bar to the central tube center
d_2	mm	Height of rotation bar to the ball joint center
e	-	Ellipse eccentricity
f_x	pixel	Focal length in x-component of pixel coordinates
f_y	pixel	Focal length in y-component of pixel coordinates
\vec{n}_i	-	Initial normal vector
\vec{n}_f	-	Final normal vector
r_i	-	Component of rotation matrix
s	-	Scale factor
t_i	-	Component of translation vector
u	pixel	Component of pixel system of coordinates
u_0	pixel	Principal point (u -component)
v	pixel	Component of pixel system of coordinates
v_0	pixel	Principal point (v -component)

Abbreviations

CCD	Charge-coupled device
CST	Concentrating Solar Thermal Power plant
EOS	Electronic and Optical system
FEM	Finite element method

FRT	Fringe reflection technique
GUI	Graphical user interface
ISE	Institute of Solar Energy
OpenCV	Open computer vision library
PnP	Perspective-n-point method
TFT	Thin film transistor
XGA	Extended graphics array

List of addendums

Addendum 1: Model builder tree with definition of parameters used materials	92
Addendum 2: Mesh statistics (left) of the heliostat surface (right)	92
Addendum 3: Visualization of segment of sinusoidal pattern through the mirror [21].	93
Addendum 4: Total station device (left) with remote controller (right)	93
Addendum 5: Calibration settings in Fringe Processor software. (TFT expresses the position of center point of the fringe pattern) [21]	94
Addendum 6: Camera calibration settings	94
Addendum 7: Graphical user interface with photogrammetry tool submenu	95
Addendum 8: Positions of the camera relative the target. Pairs of images composed relative position with zero angle is tested	95
Addendum 9: Camera position with respect to incident angle ξ and distance to the target d	95
Addendum 10: Table of measurement results of implemented photogrammetry technique. Green row indicates the best result achieved with use of ITERATIVE perspective-n-point method.....	96
Addendum 11: a) Narrow, b) medium and c) wide geometric layout	97
Addendum 12: Set of dimensions of the tubes used in optimization procedure. Symbol W is a width of the tube, T – tube thickness	97
Addendum 13: Standard deviations at extreme points (angle of incidence) with respect to cross-sectional modules ratio	98
Addendum 14: Standard deviations at extreme points with respect to distance of rotation bar to the center of central tube	98
Addendum 15: Standard deviations at extreme points with respect to distance between joint and rotation bar height level.....	98
Addendum 16: Standard deviations at extreme points with respect to connector's layout	99
Addendum 17: Connection of mirror, frame and stand of the heliostat	99
Addendum 18: Fixation of heliostat's frame in inclined position	100
Addendum 19: Deflectometry measurement setup with heliostat prototype	100

Addendum 20: Example of photographs of completely overlapping measurement. All reference markers (on the wall and locker) are visible in each image	101
Addendum 21: Standard deviation of the heliostat specular surface of FEM model and heliostat prototype with FRT validation	101
Addendum 22: Effective focal lengths of numerically calculated (theoretical), FEM simulated and FRT measured surfaces	101

1 Introduction

All kinds of solar plants use solar radiation as an alternative energy source. Solar radiation can be used for the needs of heating and electricity generation. The advantages of solar energy can be attributed the renewability of the energy source, noiseless and no harmful emissions into the atmosphere in the processing of solar radiation into other forms of energy. The disadvantages of solar energy are the dependence of the intensity of solar radiation on the daily and seasonal rhythms, as well as the need for large areas for the construction of solar power plants. In this regard, to be able to increase the efficiency of the system, the amount of energy received per unit time has to be increased.

At the first part of this work, a modified heliostat device, which is one of the main elements of the solar tower power plane, is presented. The main idea and problem associated with this device is described in details in the first part of this paper. Also, in this part a solution of how to avoid undesirable effect, caused during operation, is delineated. The solution is given in form of mathematical model of reflective surface of the heliostat device, which has been written in Matlab software.

The second chapter is aimed to introduce different techniques and tools that are used in creation and analysis of an optimal model of the heliostat device. The model is created in finite element software COMSOL Multiphysics. Further, theoretical aspects of two techniques, which are used in validation of the heliostat prototype, are written. These techniques are deflectometry and photogrammetry.

Next part of work is devoted to detailed description of practical using of methods mentioned above. A description of main steps in realization of three-dimensional model of the heliostat is written. In each subsection, the basic principles will be described by which the model will be created. Further, a procedure of validation of heliostat prototype, with use of non-contact optical methods, is given.

Lastly, analysis of performed FEM simulations and measurements is performed in form of comparison of computed results.

2 Theoretical aspects of the heliostat device

2.1 Principle of the heliostat device

In order to have an understanding of what a heliostat device and what its function is, the solar tower technology that converts sunshine into electricity for the world's electricity grids is introduced. Such system can be divided into four main elements:

- Concentration system (field of mirrors and tower)
- Receiver (boiler)
- Thermodynamic cycle (turbine, alternator)
- Storage system

Knowing the efficiency of these four principal elements enables the quantification of electrical power produced by the power station. Since the main objective is to get the maximum energy from the sun's rays at the lowest possible cost, it is necessary to analyze the sensitivity of various parameters [1]. As an example of solar power plant, Figure 1 illustrates a Concentrating Solar Thermal Power (CST) plant with molten salt storage.

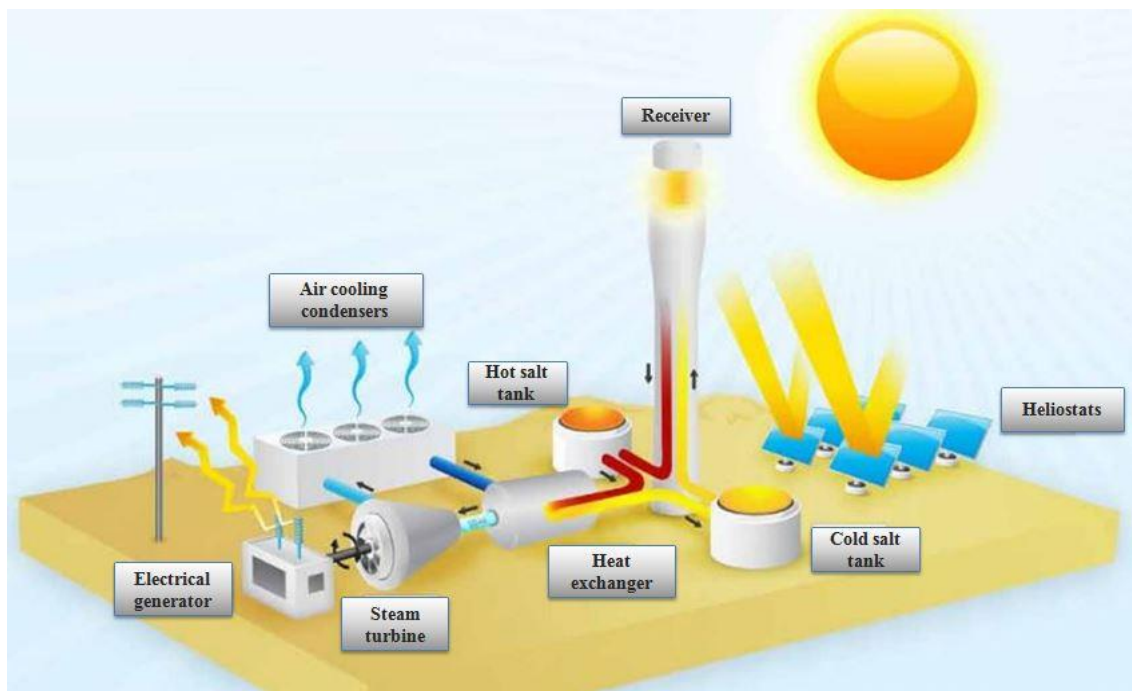


Figure 1: Concentrating Solar Thermal Power plant installation [2]

From illustration above, we can observe how six heliostats tracking mirrors (in reality there are thousands of heliostats) reflects onto the receiver placed at the top of the tower. The temperature of about 565-650 °C can be achieved in the receiver (from [3] temperature of above 1200 °C can be reached). At the receiver, heated molten salt flows down (path of flowing depicted in red) into the hot salt tank. Further, the water heated in heat exchanger by passing the hot molten salt through it. The generated steam is piped to the steam turbine that in turn spins an electric generator. Lastly, hot molten salt cools down in heat exchanger and returns to the cold tank (illustrated in yellow) from where the salt will be reheated again in the tower. More detailed description of described technology is given in [2].

As we can see from Figure 1, software-controlled heliostats (as components of the concentration system) have to always reflect light from the sun as it moves across the sky towards the target/receiver. The light is reflected and concentrated from the heliostats' curved mirror surfaces onto a receiver placed at the top of the tower. The heliostats are 'tracked' by use of sun position algorithms and tracking error correction functions.

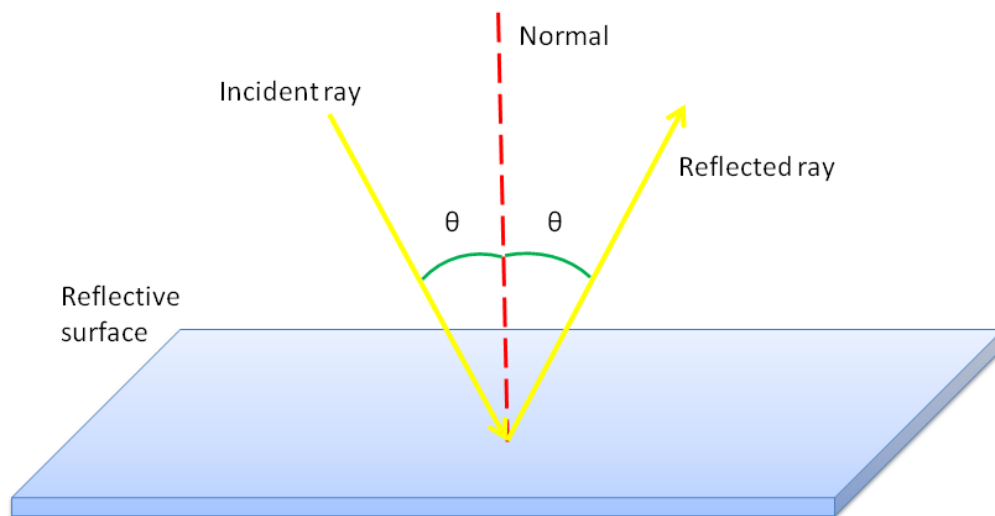


Figure 2: *Illustration of angle of incidence θ on a flat mirror of directed solar radiation .The angle of incidence is always positive and measured from the normal of the surface by definition*

The angle of incidence θ on the heliostat is the angle between the normal of the reflector at a certain point on the mirror (for most part the center of the heliostat surface) and the solar sun position vector. The figure above presents an example of specular reflection, when the incident angle and reflected angle are the same. It is important to

note that as the mirror moves through a certain angle, the reflected ray turns through twice that angle.

There are different types of heliostats. The types differ in terms of the orientation of two tracking axes (the axes about which the heliostat is rotated into the required position in dependence of the sun's and the target's -receiver at the top of the tower- position). The rotational tracking axes are perpendicular to each other. One of the axis is always fixed in its orientation (called the primary axis) whilst the other (secondary axis) is rotated about the primary axis. The different types of heliostat, which are described in this text, are the fixed-horizontal heliostat, the azimuth-elevation heliostat and the target-aligned heliostat. They differ with regard to the primary axis orientation.

In Figure 3 a conventional fixed horizontal heliostat is depicted.

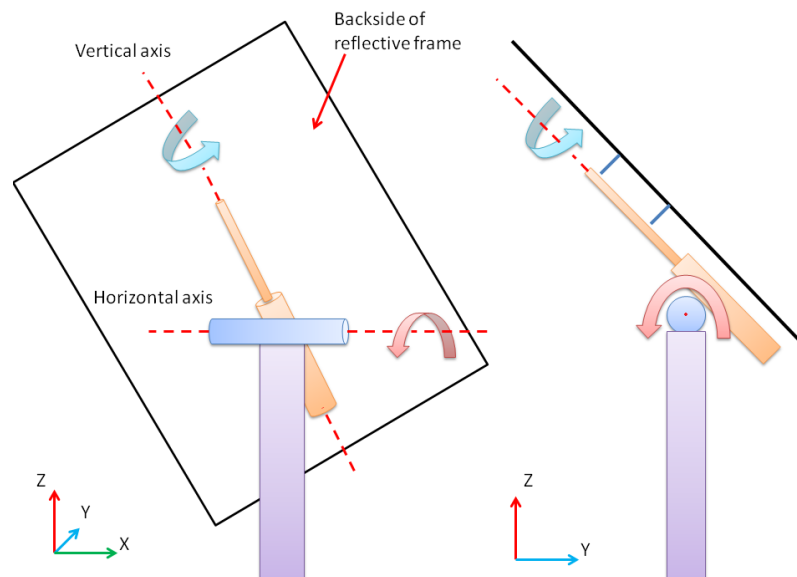


Figure 3: *Fixed horizontal heliostat*

Fixed horizontal heliostat is given as a structure with a reflected frame of different shapes (in Figure 3 a rectangular shape is presented) and two rotational axes that are perpendicular one to another. Primary axis (horizontal) is in fixed position. The second axis is attached to the frame of reflector and it moves around the primary axis.

The most common type of heliostat tracking is so called azimuth-elevation tracking. The scheme of use of this technique is shown in figure below.

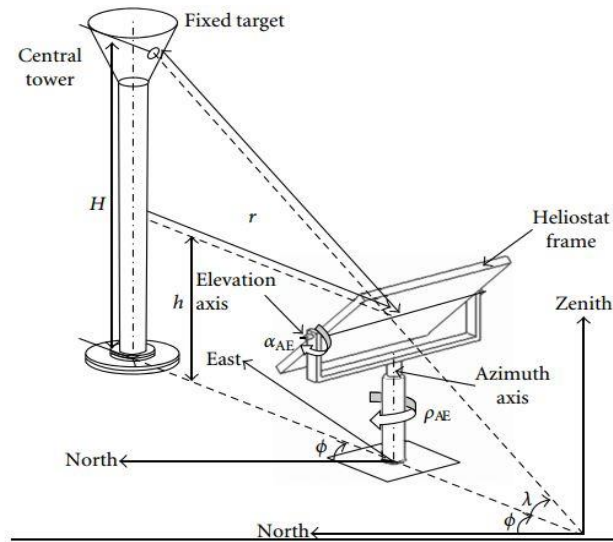


Figure 4: Azimuth-elevation sun-tracking method [4]

In such technique of tracking, azimuth axis is the primary axis, which is directed towards the zenith. The elevation axis (secondary) is perpendicular to azimuth axis and tangent to heliostat frame.

Another, sun-tracking technique is so called target-aligned method (in [4] spinning-elevation term is used).

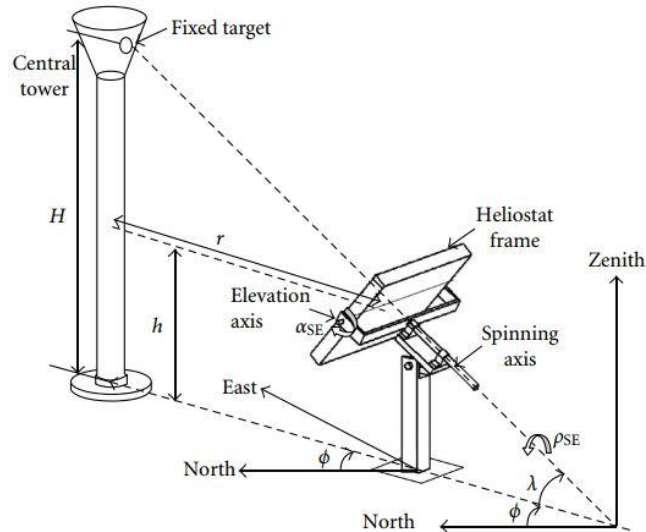


Figure 5: Target-aligned tracking method [4]

In this tracking method primary axis (named spinning axis) is oriented towards to the fixed target. Such construction allows us to maintain the heliostat normal within tangential plane (concept “tangential plane” will be explained further).

These three types of heliostats all have in common that the reflective surface is curved in order to achieve a concentration of sunlight at the receiver.

Because the sunlight is incident on the heliostat mirror at an angle, an optical aberration called astigmatism occurs. Astigmatism leads to an enlargement of the focal spot at the target.

2.2 Astigmatism

In this work, an astigmatic corrected target-aligned heliostat for high concentration will be developed and described in more detail.

At the beginning a non-astigmatism example with concave mirror is shown.

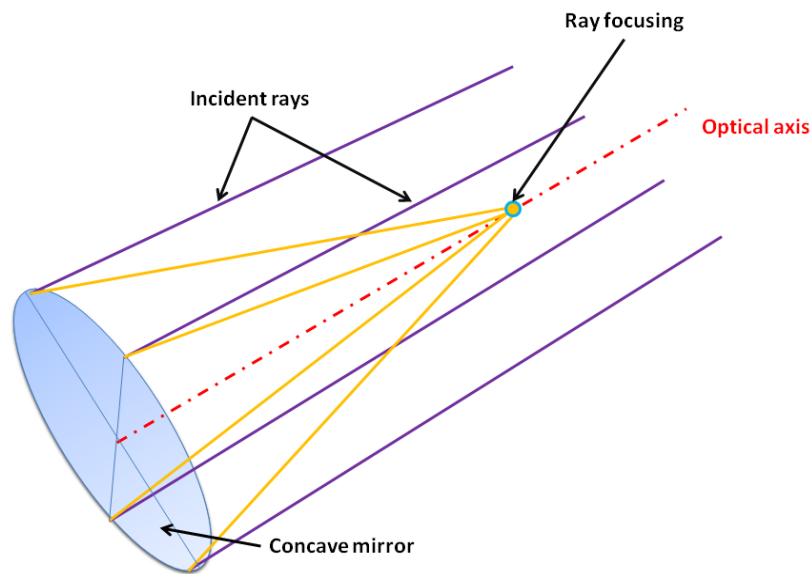


Figure 6: *Ideal focusing of a concave mirror*

In sketch above, an ideal ray focusing case is presented. Incident sunlight rays are parallel to optical axis of the mirror. Focusing of rays reflected from the mirror is located at one point. An example with incident rays, which are not parallel to the optical axis, is given in description further.

Astigmatism, due to off normal incidence of sunlight on the curved heliostat surface, introduces a spread in the focal spot at the target. This is detrimental for high concentration – high temperature applications because it also limits subsequent secondary concentration and introduces spillage losses for fixed aperture receivers [5]. Figures below illustrate the astigmatism effect.

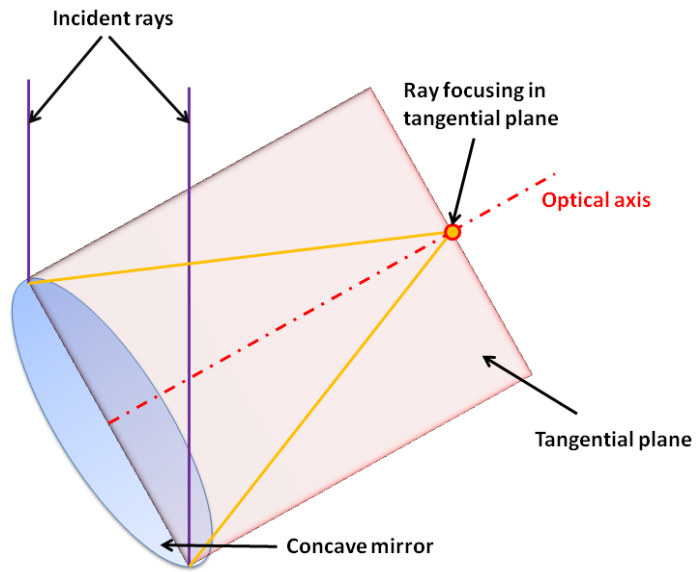


Figure 7: *Ray focusing in tangential plane*

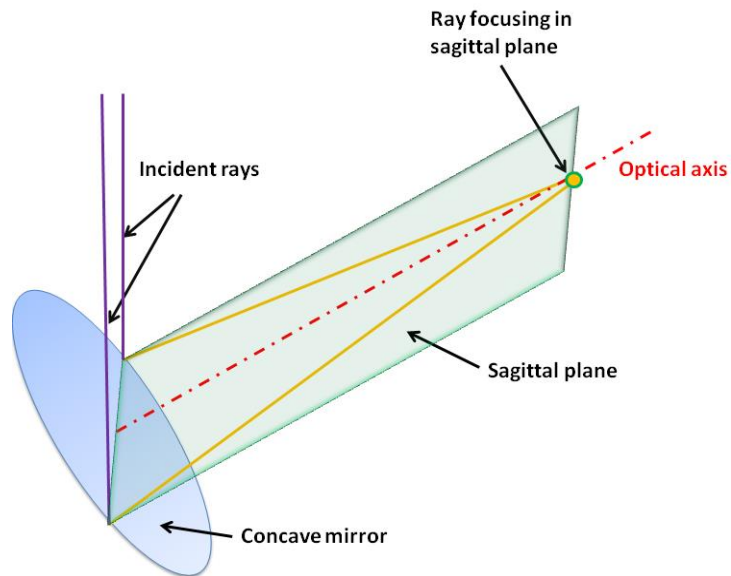


Figure 8: *Ray focusing in sagittal plane*

Figure 7 and Figure 8 illustrates a ray focusing in two planes called tangential and sagittal. These planes are perpendicular one to another. In Figure 9 we can observe complete astigmatism representation.

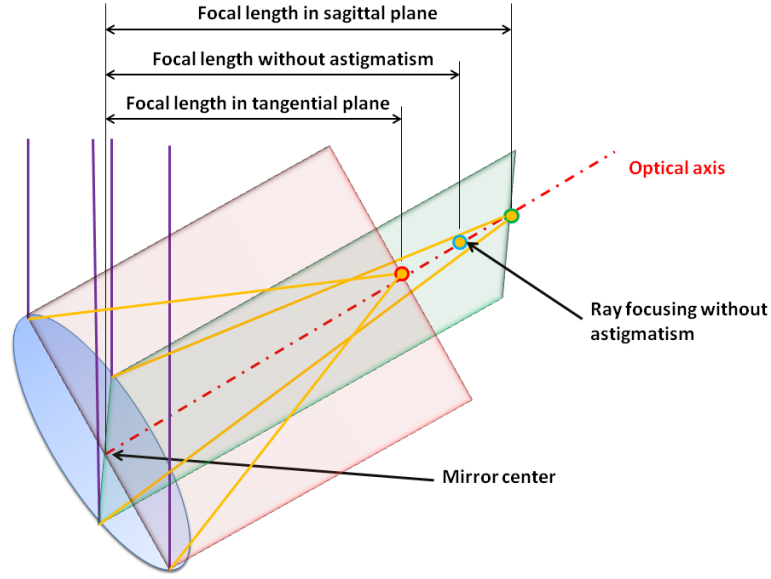


Figure 9: *Astigmatism effect of concave mirror*

From figure above, we can see how astigmatism affects on heliostat efficiency. Focal length (distance from center of the reflector to focusing location on optical axis) in sagittal plane is longer than focal length in case without astigmatism effect presented in Figure 6. For tangential plane, sunlight rays form shorter focal length than it shown in ideal case. That leads to enlargement of the focal spot at receiver. For astigmatism compensation a non-symmetric heliostat has to be devised. Such heliostat has two different main radii of curvature and has different tracking axes, such that sagittal and tangential directions remain stationary in the reflector plane and coincide with its major axis of curvature [5].

Next section presents a mathematical reproduction of the shape, which has to be achieved through deformation of the surface of the heliostat for astigmatism compensation.

2.3 Shape of the reflector

This section focuses on the determination of the reflective surface shape of an astigmatic corrected heliostat in three-dimensional space. Equation (2.1) gives the expression of a rotational paraboloid of which the reflector's surface is a segment.

$$f(x, y) = \frac{x^2}{4 \cdot F(\theta, S)} + \frac{y^2}{4 \cdot F(\theta, S)} - F(\theta, S), \text{ for } x, y \in \mathbb{R} \quad (2.1)$$

In this formulation the focal point of the paraboloid corresponds to the origin of the Cartesian coordinate system. Focal length F is a function of an incidence angle θ and slant range S . A graphical representation of equation (2.1) is shown below.

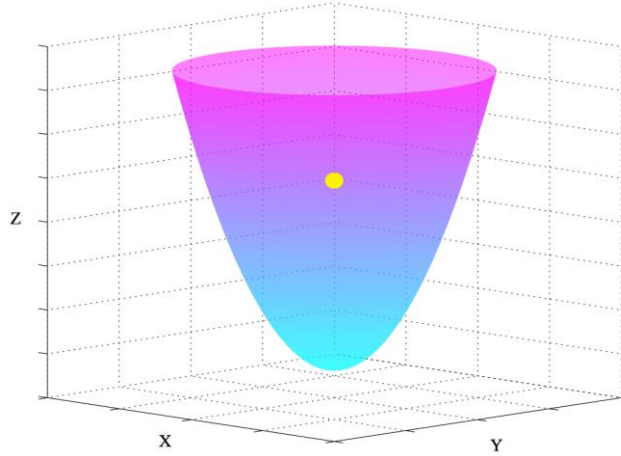


Figure 10: Rotational paraboloid with depicted focal point

The focal length function is given by following equation.

$$F = S \cdot \cos^2(\theta) \quad (2.2)$$

Argument S is given with respect to Pythagorean equation.

$$S = \sqrt{H^2 + D^2} \quad (2.3)$$

Parameters H and D are respectively the altitude to the receiver and distance from the center of reflector surface to the tower center axis (see **Figure 11**).

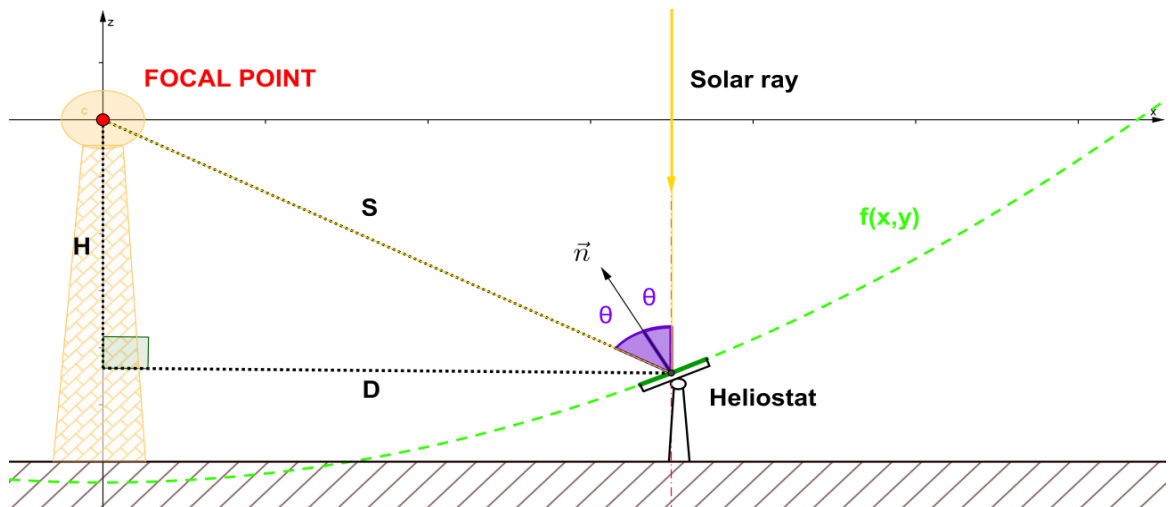


Figure 11: Schematic representation of reflection of solar ray from the surface of heliostat in tangential plane

As mentioned at the beginning of this section, the shape of the reflector is a section of paraboloid. To find out a position of that surface on a rotational paraboloid, the center point of mirror must be expressed in the local paraboloid coordinate system. The center point of the heliostat is always at a fixed slant range distance S from the target center (Cartesian coordinate origin). The center point can be calculated by solving equation (2.4) for x , assuming that parabola is in the tangential plane (setting $y = 0$).

$$S = \sqrt{x^2 + y^2 + \left(\frac{x^2}{4 \cdot F(\theta)} + \frac{y^2}{4 \cdot F(\theta)} - F(\theta) \right)^2} \quad (2.4)$$

The real positive root of equation above corresponds to the x -coordinate of the center point of the mirror. By substituting x and y coordinate of the center point in equation (2.1), z -coordinate can be calculated.

To describe a surface of reflection, calculation of vertical and horizontal components of the reflector (components cross each other at the center point) has to be performed. Figure 12 illustrates the components on paraboloid.

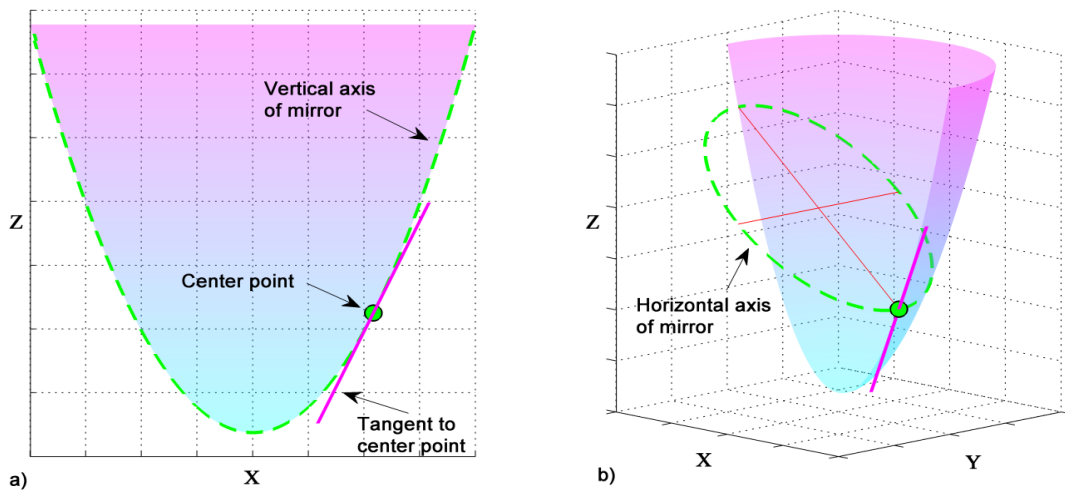


Figure 12: Parabola as a forming of vertical axis of the mirror a). Ellipse as a forming of horizontal axis of the reflector's surface b)

As can be observed from the figure above, segments of parabola and ellipse will form the shape of reflector. It should be clarified that elliptic frame and parabola are located in sagittal and tangential plane of the ray reflector, respectively.

Coordinates determination of these segments with given size of the reflector's plate will be performed. For that purpose it is necessary to resort to equation (2.5).

$$\text{Curve's length} = \int \sqrt{1 + \left(\frac{d(f(x))}{dx}\right)^2} dx \quad (2.5)$$

That equation allows length calculation of an irregular arc segment (is also called rectification of a curve) defined by arbitrary function $f(x)$. Let's see how this equation will be used in our case.

At the beginning, case with parabola will be considered. In accordance to the center point coordinates and given mirror length L in vertical axis, equation (2.5) will transform in following equation

$$L = \int_{x_{min}}^{x_{max}} \sqrt{1 + \left(\frac{d\left(\frac{x^2}{4 \cdot F(\theta, S)} - F(\theta, S)\right)}{dx}\right)^2} dx \quad (2.6)$$

This equation has two unknown parameters x_{max} and x_{min} . To be able to solve it, mathematical expression (2.6) can be presented as a system of two equations with two unknown variables.

$$\begin{cases} L = 2 \cdot \int_{x_{cent}}^{x_{max}} \sqrt{1 + \left(\frac{d\left(\frac{x^2}{4 \cdot F(\theta, S)} - F(\theta, S)\right)}{dx}\right)^2} dx \\ L = 2 \cdot \int_{x_{min}}^{x_{cent}} \sqrt{1 + \left(\frac{d\left(\frac{x^2}{4 \cdot F(\theta, S)} - F(\theta, S)\right)}{dx}\right)^2} dx \end{cases} \quad (2.7)$$

Parameter x_{cent} is a real positive root of equation (2.4). Result of system of equations above is shown in Figure 13.

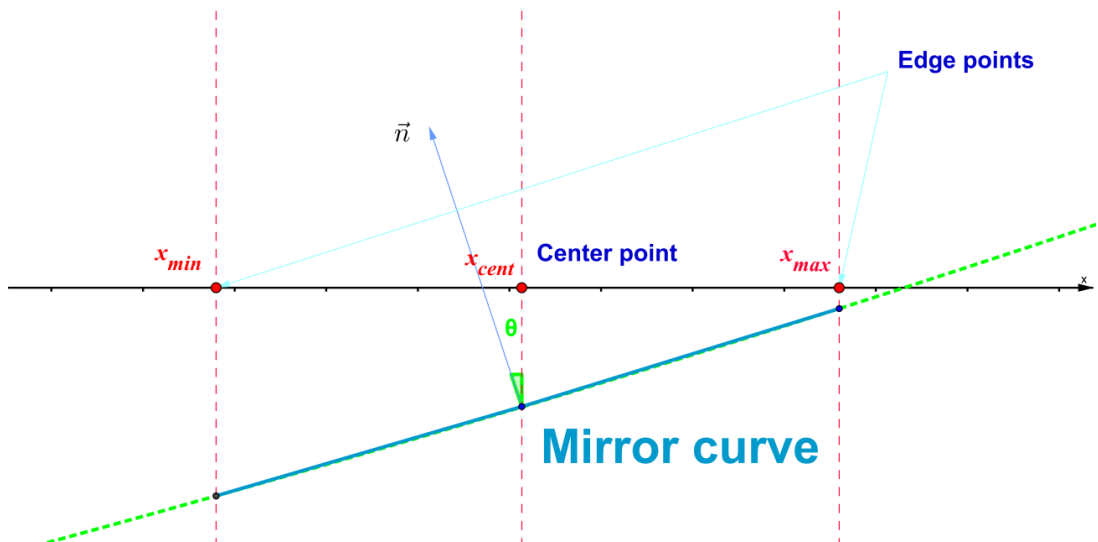


Figure 13: Representation of shape of the mirror surface as a segment of a parabola in xz -plane

Case with elliptic frame will be considered further. Before determination of segment on ellipse will be performed, it is necessary to ascertain parameters that forms ellipse. Equation of an ellipse is

$$\left(\frac{x}{a}\right)^2 + \left(\frac{y}{b}\right)^2 = 1 \quad (2.8)$$

Parameter a and b correspond to major and minor radius of ellipse, respectively. Figure 14 shows the main idea how to calculate these parameters for our task.

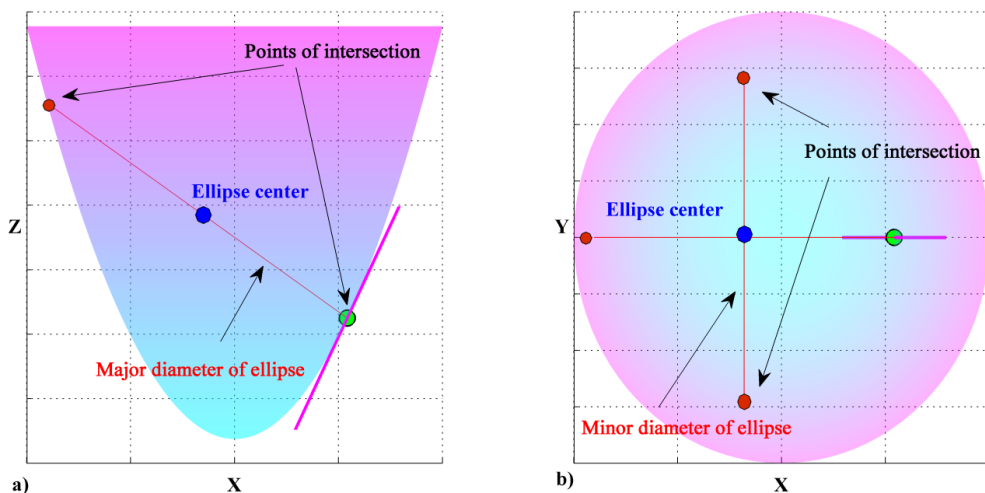


Figure 14: Major diameter of ellipse a). Minor diameter of ellipse b)

From Figure 14 a) it is clear that for determination of coordinates of intersection it is necessary to equate equation of paraboloid and equation of line that is formed by

the intersection of sagittal and tangential plane. From Figure 14 b) coordinates of intersection can be found out by the equating of paraboloid equation and line that goes through the ellipse center (on sagittal plane). These two lines (equations of which compared with paraboloid equation) are orthogonal to each other.

When coordinates of intersection points are found out, distance between appropriate points can be calculated. It should be noted that major and minor diameters are two times bigger than radius a and b , respectively.

With known parameters of ellipse, determination of segment on ellipse curve will be performed. For ellipse, equation (2.5) has following modified form

$$\text{Arc length} = b \cdot \int \sqrt{1 - e^2 \cdot \sin^2(\alpha)} d\alpha \quad (2.9)$$

Angle α has been obtained due to trigonometric substitution of argument x of equation (2.5).

$$x = a \cdot \sin(\alpha) \quad (2.10)$$

Eccentricity e is given by equation (2.11).

$$e = \sqrt{1 - \left(\frac{b}{a}\right)^2} \quad (2.11)$$

Figure 15 illustrates how can be found curvature of the heliostat surface in elliptic frame.

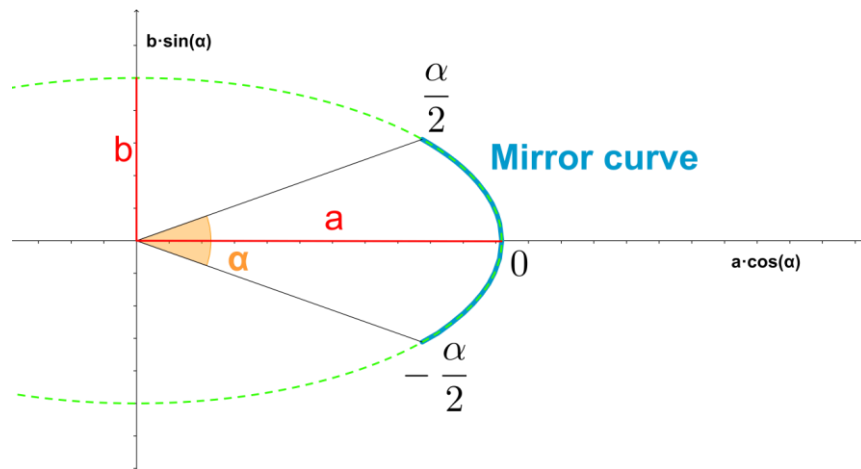


Figure 15: Segment of ellipse that presents a shape of the mirror surface in elliptic plane

It is clear that mirror curve will be calculated in same way as for case with parabola. With given length L , it is possible to find out argument α by equation below

$$L = 2 \cdot \int_0^{\frac{\alpha}{2}} \sqrt{1 - e^2 \cdot \sin^2(\alpha)} d\alpha \quad (2.12)$$

Due this last equation, mathematical description of the surface for horizontal components is done.

The whole shape of the reflector can be obtained as it is specified in Figure 16.

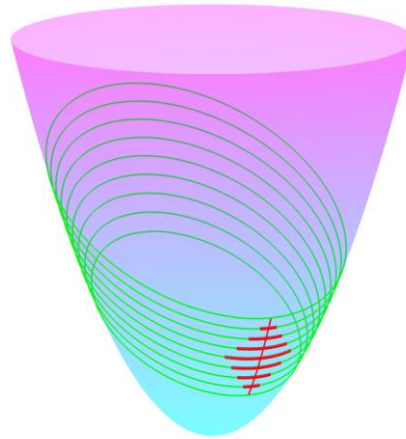


Figure 16: Shape of the reflector formed by a few segments of ellipse

From figure above it is clear that each point on parabola segment has its own arc of ellipse. In such a way, it is possible to identify coordinates of the whole reflective surface.

Mathematical model of reflector surface has a few tasks that must be solved. Next section of work describes these tasks and presents their solution.

2.4 Deformation of reflectors shape

In previous section, a model of reflective surface of heliostat has been presented. The model can be used for observing changes of reflective shape with respect to different parameters. Also, model description allows determine the deformation range of surface shape of the reflector with required size. Such information is important to use when finite element model of heliostat construction is being created.

To observe shape changes of heliostat reflector, shape difference of paraboloid in tangential plane will be considered. Figure 17 shows how different angles of incidence of focal length function change the shape of parabola.

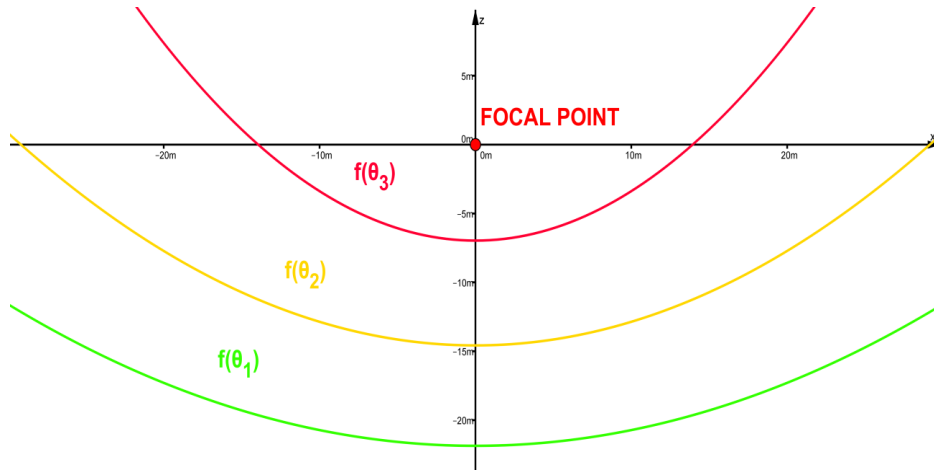


Figure 17: Shapes of parabolas with respect to incident angle ($\theta_1 = 30^\circ$, $\theta_2 = 45^\circ$, $\theta_3 = 60^\circ$ and slant range $S = 29,15$ m)

As we can see, parabolas differ with change of incident angle. The figure above is a starting point of deformation shape determination. For that purpose, center point coordinates of the mirror will be ascertained in the same manner as it was done in previous section. Coordinates of center point on parabolas will have different values for the same slant range (see **Figure 18**).

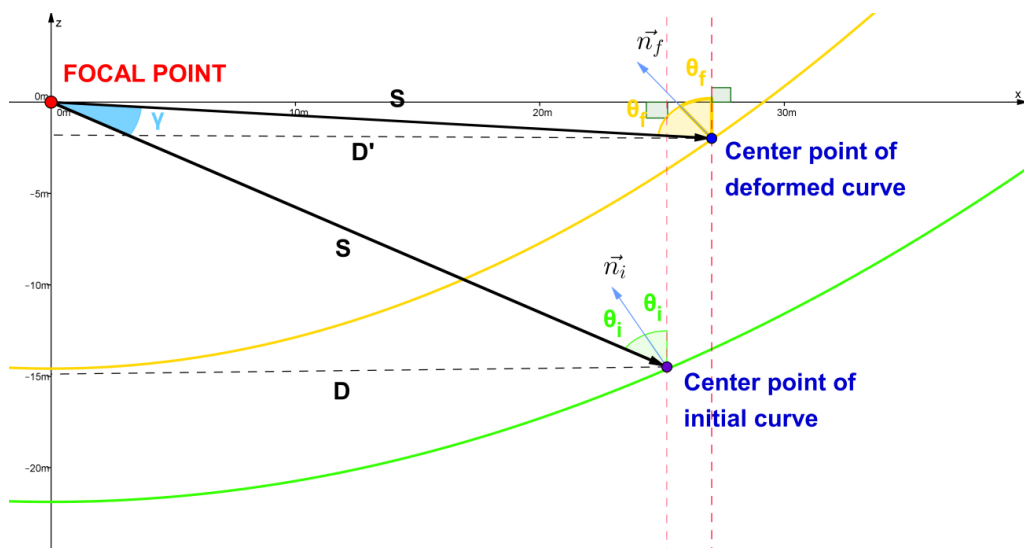


Figure 18: Center points of the mirror surface for two different parabolas ($\theta_i = 30^\circ$, $\theta_f = 45^\circ$ and slant range $S = 29,15$ m)

Angle γ corresponds to spatial angle between the center points with respect to origin of Cartesian coordinate system. To be able to compare segments of parabolas with their own center point, angle γ is used. From the scheme above it is clear that angle can be deduced as

$$\gamma = |90^\circ - 2 \cdot \theta_i - 90^\circ + 2 \cdot \theta_f| \quad (2.13)$$

$$\gamma = 2 \cdot |(\theta_i - \theta_f)| \quad (2.14)$$

The segments of parabolas have to be placed at the same point. Thus, deformed curve will be placed at the center point of initial curve by rotational angle calculated in equation (2.14). Result of such manipulation illustrated in figure below.

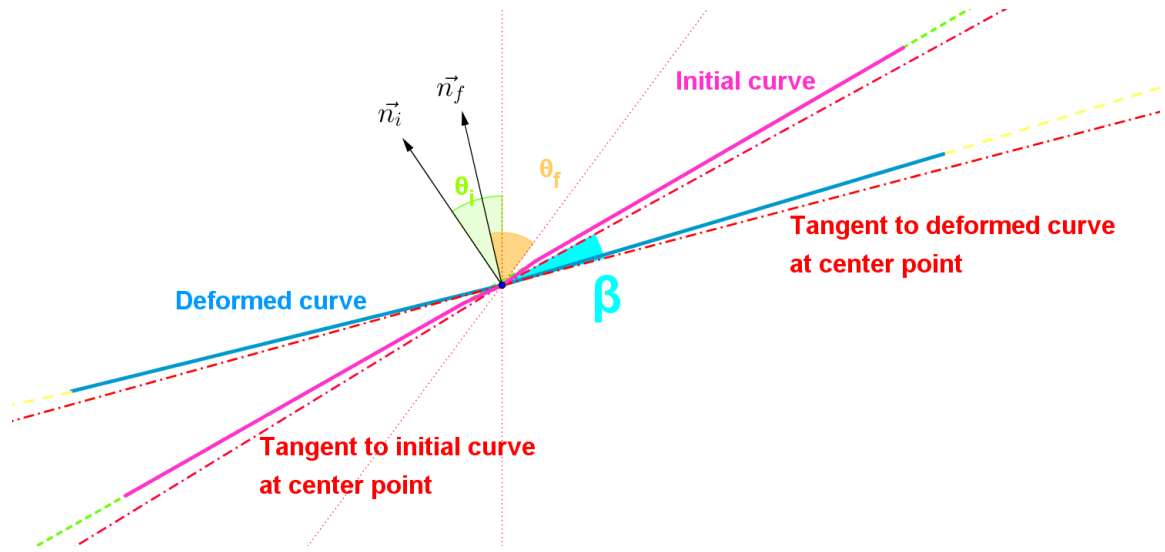


Figure 19: Placement of parabolas segments at the same center point by rotation of angle γ

Angle β occurred in Figure 19 is an angle between tangents of curves. Assignment of that angle will be described further.

With respect to heliostat functionality, the transformation of initial curve of reflector into deformed can be performed in two steps. The first one is rotation of initial curve around center point. Angle β is aimed to perform that rotation. Normal vectors \vec{n}_i and \vec{n}_f makes a right angle with the tangent of initial and deformed curve respectively. It means that angle β can be found as an absolute value of difference of incident angles.

$$\beta = |\theta_i - \theta_f| \quad (2.15)$$

Rotation of two curves by the angle β allows compensation of certain part of difference between curves without deformation of initial shape of the mirror.

Next step of transformation assumes deformation of the reflector surface. It is necessary in situation when there is no possibility to achieve a deformed curve by only rotation of initial curve. Therefore, when initial curve was rotated, deviation between two curves can be calculated. For that point is very important to normalize our curves with respect to the length of the mirror plate. Normalization calculates differences of curves at the same points on the length of the reflector. Figure 20 shows the deviation in normalized system of coordinates.

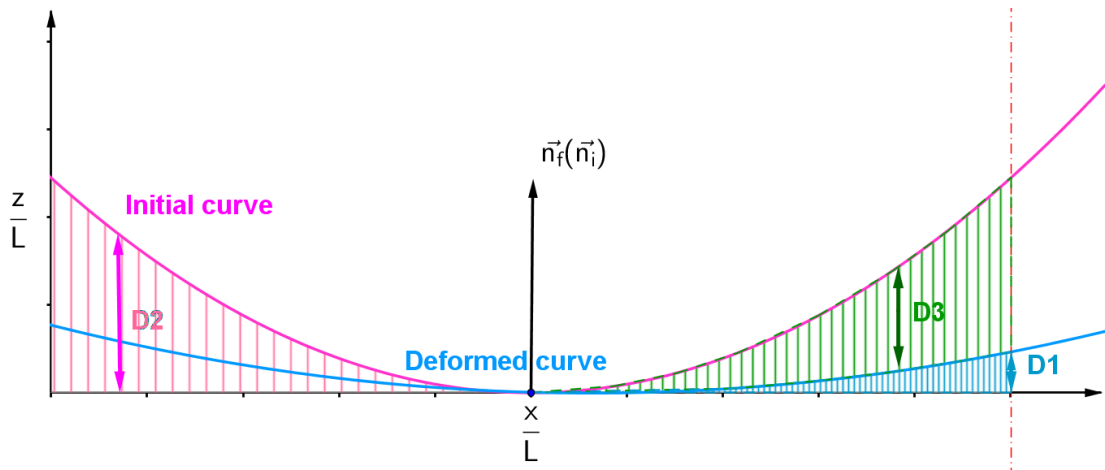


Figure 20: *Deviation of curves in normalized system of coordinates*

Deviation D_1 corresponds to difference between flat mirror and initial curve, D_2 represents difference between deformed curve and flat plate of the reflector. Lastly D_3 is an absolute difference between D_2 and D_1 .

Ascertained deviations are valid for vertical component of the reflective plate. In the same way a horizontal component can be determined. That assumes calculations on sagittal plane (ellipse frame) and compared curves correspond to arcs of ellipses (see **Figure 21**).

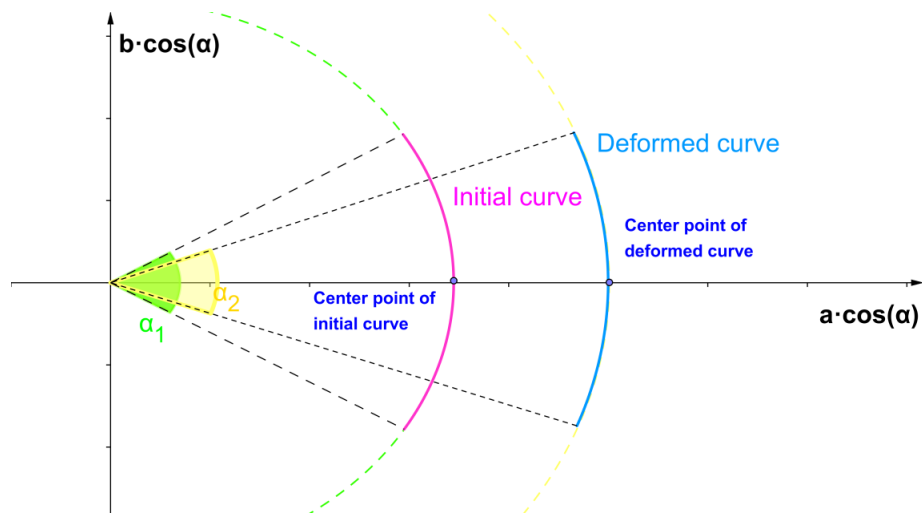


Figure 21: Projection of curves on sagittal plane

By the same way as for parabolas, deviation of elliptic arcs can be determined.

As a result of all computations defined in that this section, we can observe three-dimensional models of two surfaces parameterized by different angles of incidence (see **Figure 22**).

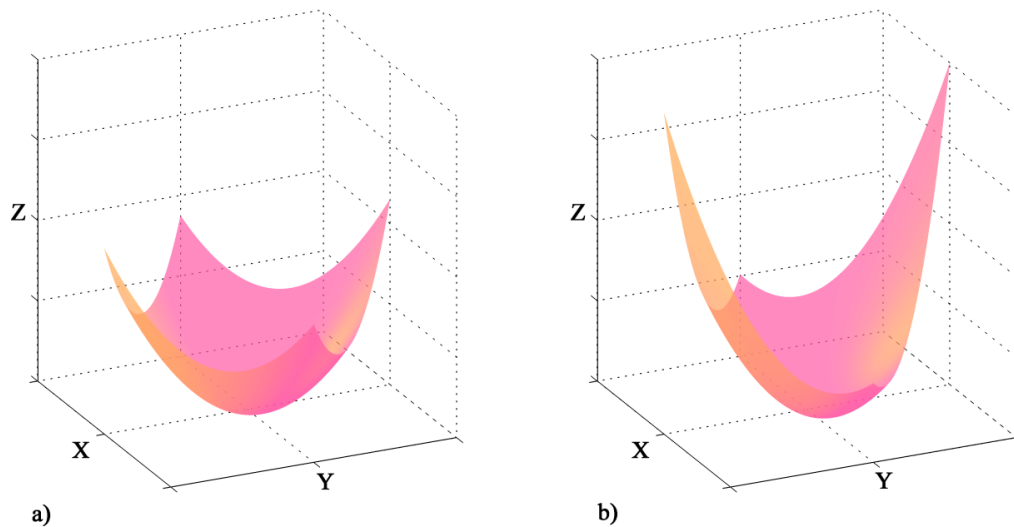


Figure 22: Normalized shapes of reflective surface with $\theta = 30^\circ$ a), with $\theta = 60^\circ$ b)

The change in mirror surface curvature has to be achieved without additional (apart from the required two drives for tracking) actuators through distributing stress in the heliostat frame correctly.

It is necessary that changes in shape are comparable with linear elastic deformation of heliostat construction. Reflective surface of finite element model of

heliostat (described in subchapter 4.1) will be compared with model of surface performed above. On basis of that comparison, an optimal model of heliostat's reflector will be found.

3 Methods

This part of work gives an overview of tools and techniques that have been used in heliostat issue described in previous chapter. In first section a description of finite element method, which will be used in investigation of deformation of heliostat surface, is given. Following two subchapters present main principles of two non-contact optical methods such as deflectometry and photogrammetry.

3.1 FEM

Computer modeling and simulation have become an important part of engineering and science. The main idea of these virtual tools is based in creation of a system or an object behavior, which is analyzed with respect to different physical conditions. In this work finite element method (FEM) modeling is used in creation of a principal structure and optimization of target-aligned heliostat.

Finite element method is a numerical discretization method that is aimed to find a solution of a complicated problem by replacing it by a simpler one for partial differential equations [6]. Authors in [7] give following steps in simulation process with use of FEM:

- Idealization
- Discretization
- Solution

The goal of the first step (idealization) is to describe a physical system by a mathematical model. In [7] mathematical model is given as an abstraction of the physical reality and results generated by the mathematical model are physically re-interpreted.

The second step is a discretization of the mathematical model. Mostly mathematical model is not simple to solve. The model is described by a system of partial differential equations with respect to interface and boundary conditions in space and time. The problem of such models is an infinite number of degrees of freedom (number of independently varying parameters of the system). With use of discretization, the number of degrees of freedom becomes finite and practical for numerical simulations. An example of geometric discretization of the heliostat's model in finite

elements is presented in 4.1.4. In further these elements are used to represent a solution field (the third step in simulation). Every element is described by a system of functions at a set of nodal points (see **Figure 24**). The solution is computed at these node points. By assembling of all solutions a model behavior can be described. In sketch below a simplified view of the simulation process, described above, is given.

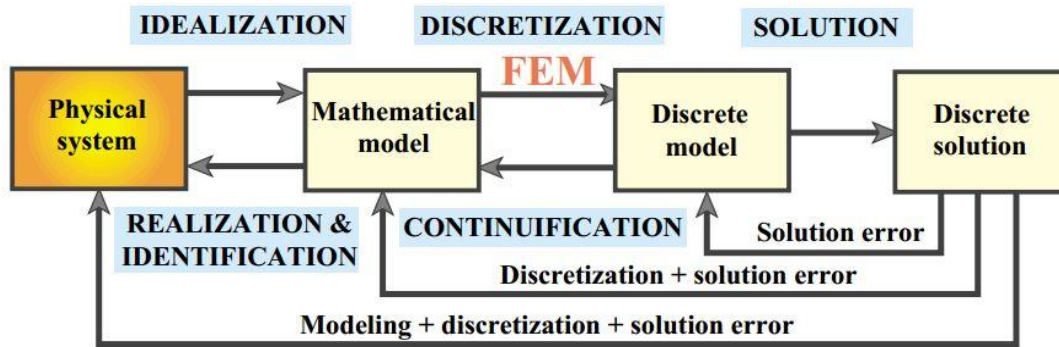


Figure 23: *Physical simulation process [7]*

From the scheme above it can be seen that each step in simulation has a source of error. Authors of [7] identified several reasons of error occurrence. The first one is modeling errors. Such error is difficult to evaluate by reason of model validation as it requires a comparison with experiment results.

Another important source of errors is a discretization error. Generally, a discrete model (as a product of discretization procedure) is an approximation to the exact solution [7]. The way of how this error can be partially eliminated is to increase number of elements, so discrete model becomes more precise. But in this case procedure of solving becomes computationally expensive.

In following subsection, the mesh elements to which the FEM model will be subdivided is presented.

3.1.1 Mesh elements

The main idea of finite element meshing is a geometry discretization into small elements (see **Figure 24**), over which a set of equations describing the solution is possible to define.

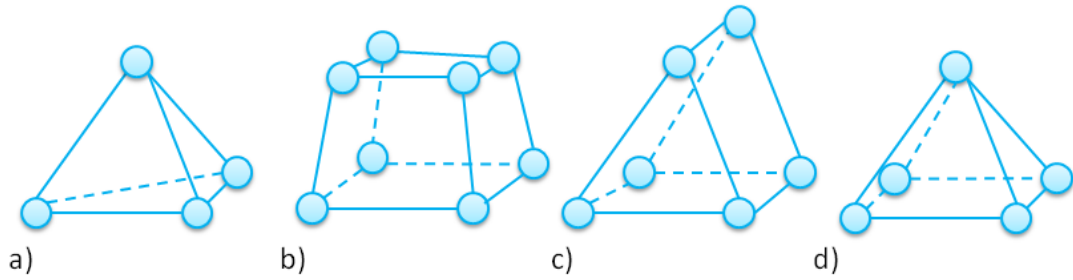


Figure 24: Mesh elements: a) tetrahedral b) hexahedral c) prismatic triangular and d) pyramid

Blue circles of each element represent nodes of element. The solution is computed at the node points. To be able to interpolate this solution throughout the element to cover the total solution field, a polynomial basis is used. The modeling procedure described in this work falls under category of finite static linear modeling. For such kind of simulations, COMSOL uses Newton-Raphson method [8] to solve a system of equations. This method is very effective for linear dependences because a solution can be figured out in one step.

Another point of FEM technique, which has to be denoted, is an element order. Usually modeling environment utilizes a second-order Lagrangian element for geometry (and solution) discretization. In sketch below, a second-order Lagrangian element is depicted.

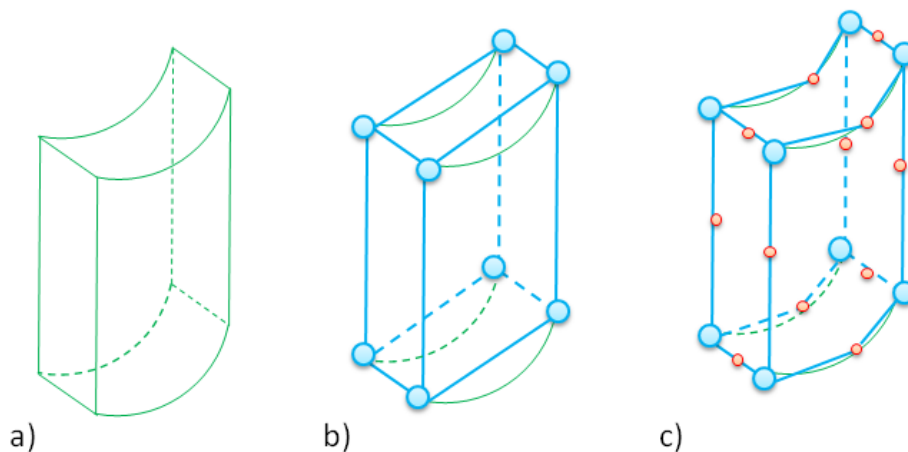


Figure 25: Cylindrical shell a) represented by the first b) and the second-order c) Lagrangian element

As we can observe, mesh element is presented not only with node on vertices (as it shown in Figure 25). Every edge of the element is presented by three points and the

edges approximated via a polynomial fit. In true, there are more nodes (in the volume center, at each quadrilateral face) but for clarity they are omitted.

The subsection presented further give a description of two mechanical properties, which are used in the model presented in subchapter 4.1.

3.1.2 *Mechanical properties of solid materials*

In solving deformation issue a static linear elastic model is used. Prefix static means that model behavior will not be studied over time and all physical parameters are assumed to be constant. In addition, it has to be mentioned that the model is considered to be isotropic (property values are identical in all orientations). Prefix linear elastic says that model is obeying Hook's law. In equation (3.1) a general Hook's law is presented.

$$\epsilon = \frac{\sigma}{E} \quad (3.1)$$

The law is given as stress-strain relationship [9]. Mechanical stress σ has the units of GPa (or N/m²). This physical quantity expresses how under certain conditions (acting of external or internal forces (gravitation, magnetic, inertial force)) each neighboring particles of a material act on another with a certain force. Equation (3.2) describes a mechanical stress, where symbol F_{app} is an applied force to the contact surface with area A .

$$\sigma = \frac{F_{app}}{A} \quad (3.2)$$

Stress of a straight bar is depicted in sketch below as an example of tensile stress.

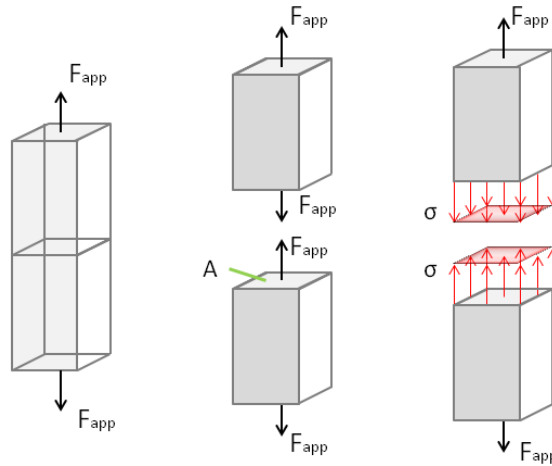


Figure 26: *Idealized stress in a straight bar*

Strain ϵ represents a displacement of particles of deformed body from their initial position. Strain is a dimensionless quantity defined as the change of the length Δl divided by the initial length l of a material (see equation (3.3)).

$$\epsilon = \frac{\Delta l}{l} \quad (3.3)$$

In Figure 27 an example of strain determination is shown.

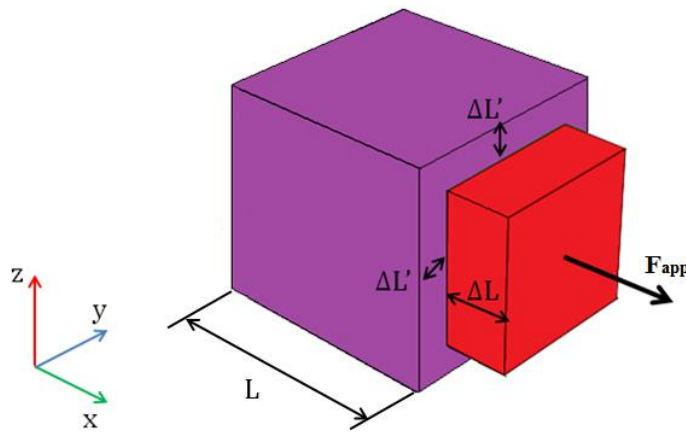


Figure 27: *Determination of the strain*

More detailed description of physical quantities mentioned above is well described in [9]. Constant of proportionality E is known as Young's modulus (module of elasticity). This module is aimed to predict the deflection occurred in statically determinate structure.

In Figure 27 a following feature can be noticed. The material, which is stretched, tends to contract in the directions transverse to the direction of stretching. Such behavior can be described by Poisson's ratio ν as a ratio of relative contraction to relative expansion of the material (see equation (3.4)).

$$\nu = \frac{\Delta L'}{\Delta L} \quad (3.4)$$

For example illustrated in Figure 27, modified Hook's law can be used to determine a displacement (deformation) of material in three directions.

$$\begin{cases} \epsilon_x = \frac{\sigma_x - \nu(\sigma_y + \sigma_z)}{E} \\ \epsilon_y = \frac{\sigma_y - \nu(\sigma_x + \sigma_z)}{E} \\ \epsilon_z = \frac{\sigma_z - \nu(\sigma_x + \sigma_y)}{E} \end{cases} \quad (3.5)$$

Graphical interpretation of the stress-strain relationship described in this subchapter is given in diagram below.

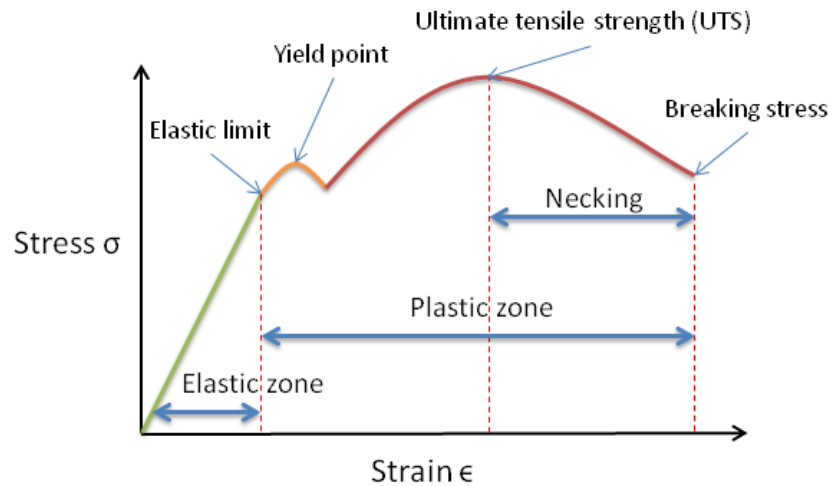


Figure 28: Example of stress-strain curve

For the model task an elastic interval is a point of interest. In this interval, the material returns to its original state after when applied force is not in action.

As we can understand from this part of work, in heliostat model linear elastic property is assignment to a heliostat structure. Such definition allows deformation of 3D model without fear of that the structure will go into a plasticity zone (no return to initial

state). Young's modulus and Poisson's ratio will be the criteria of material selection to reach deformation requirements.

3.2 Deflectometry

Deflectometry or Fringe Reflection Technique (FRT) is an optical method for assessment of specular surfaces quality. Authors of [10] gives following characteristic of the method: "It is a fast and reliable technique with high lateral resolution, which produces local surface gradient maps as a result and – after further software evaluation – local shape and curvature maps of the mirror". High lateral resolution, mentioned in this quotation, is a possibility of the measurement system to distinguish structures in a plane perpendicular to camera axis (see **Figure 29**).

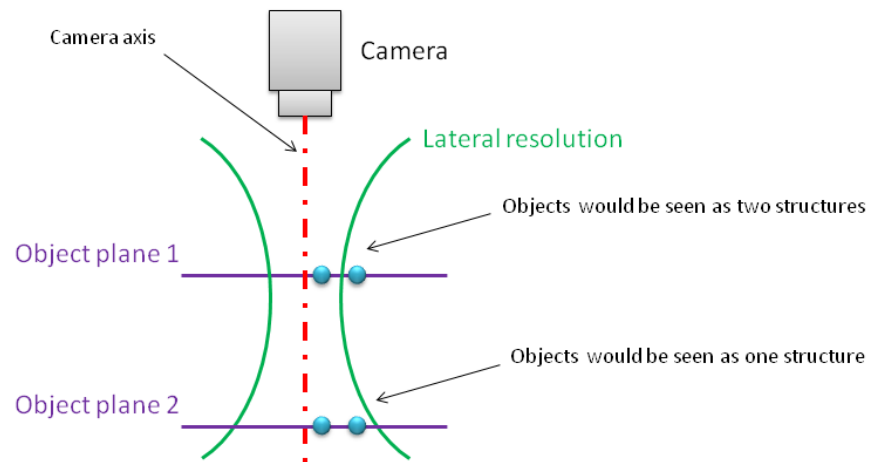


Figure 29: *Lateral resolution of deflectometry system*

The sketch above shows how objects can be registered by the camera with respect to object plane position and range of system's lateral resolution.

The basic principle of the measurement is given in sketch below.

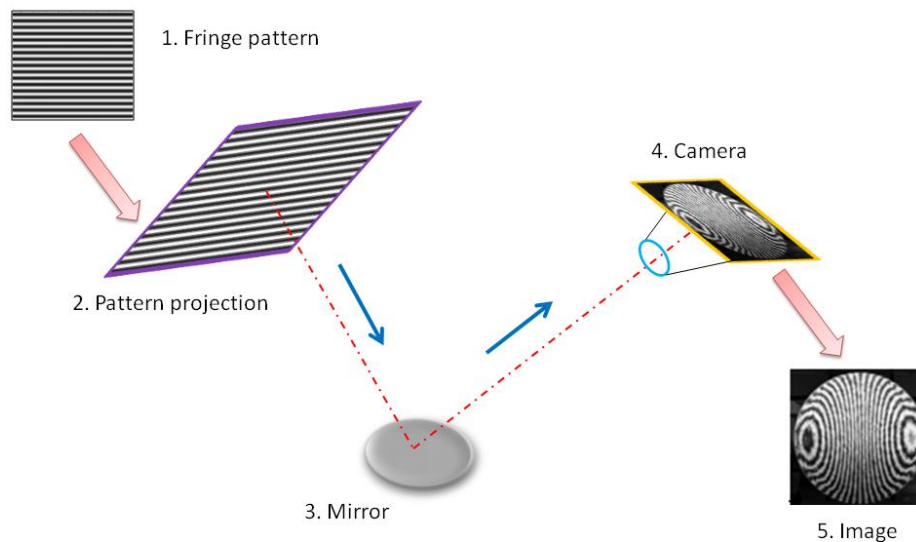


Figure 30: *Measurement principle of deflectometry*

Multiple sinusoidal phase shifted pattern is projected on a screen (pattern projection); the tested specular surface (mirror) reflects it toward the camera, depicted as CCD (charge-coupled device) chip (orange frame with an image) and lens (blue ellipse). Camera displays an image, which can be processed by software-tool for fringe evaluation. Fringe distortions, detected by the camera, are analyzed during the image processing. This allows determination of the surface normal vectors for each camera pixel.

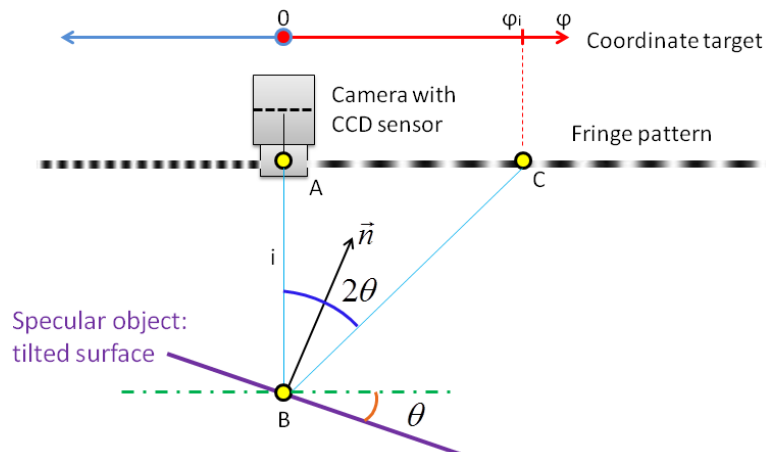


Figure 31: *Simplified measurement model (2D) of the FRT setup*

In sketch above the FRT setup is illustrated. The center of camera's aperture is depicted by point A . This point is located at the origin of lateral coordinate target system, which is attached to fringe pattern. Point B is an intersection point of vision ray of camera pixel i and specimen's specular surface. Imaging ray of pixel i , reflected from

the mirror's surface intersects the fringe pattern at C . Segment AC on sinusoidal pattern is represented by phase φ_i . Through this information, the mirror's surface normal vector \vec{n} at point B can be determined for every camera pixel. Doubled mirror angle 2θ is determined on basis of phase φ_i and the object distance from the camera (distance AB). It is worth to be noticed that depicted example (see **Figure 31**) point B represents the center point of specular surface and with use of calibration procedure distance AB is figured out. Further, the description of another non-contact optical method, which is used in mirror quality, is presented.

3.3 Photogrammetry

The name “photogrammetry” is derived from the three Greek words *phos* or *phot* which means light, *gramma* which means letter or something drawn, and *metrein*, the noun of measure. There is no accepted definition for photogrammetry. In general, photogrammetry is the science of making measurements from photographs (see **Figure 32**).

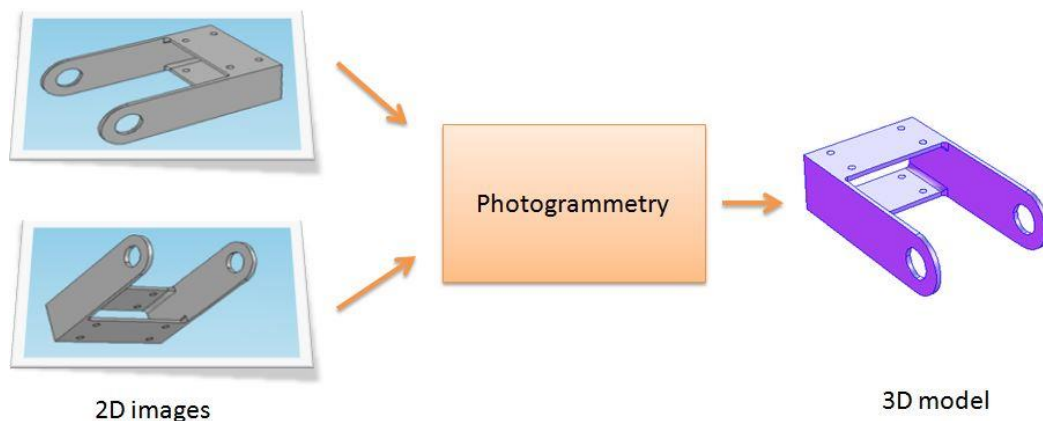


Figure 32: Principle of photogrammetry.

Such technology of generating 3D information from 2D measurements on photos can be categorized in multiplicity of ways. Authors in [11] classify photogrammetry with respect to:

- Camera position and object distance
- Number of measurement images
- Method of recording and processing
- Availability of measurement results
- Application or specialist area

Also, in [11] we can see that photogrammetry has a broad application in different spheres. Each kind of photogrammetry has its own unique features and technical nuances. Therefore, it is necessary to determine what kind of the optical method has to be used for measurement of shape of specular surface of the heliostat device. In this work, a close-range photogrammetry is assumed.

Before starting of any measurement, it is necessary know what information is expected to be obtained and does used technique allows figure out required data. For our task spatial coordinates defining the shape quality of the mirror surface is the subject of our interest. With use of photogrammetry it is possible to find out coordinates of objects with high accuracy. Authors in [12] assert that standard uncertainty of 23 micrometers can be reached with use of this technique.

In spite of diversity of photogrammetry, this optical method has basic principles that are valid for all kind of measurement. These basic concepts are represented further.

3.3.1 Camera

There are a lot of factors that influence the quality of photography. This section is focused on description of some concepts of recording device for photographic measurement.

The choice of recording device is one of the important steps for getting a quality photographs. The device contains a big number of functions which are interrelated. One of such important functions is called “field of view”. This term means how much camera sees and is a function of the focal length of the lens and the format (size) of digital sensor.

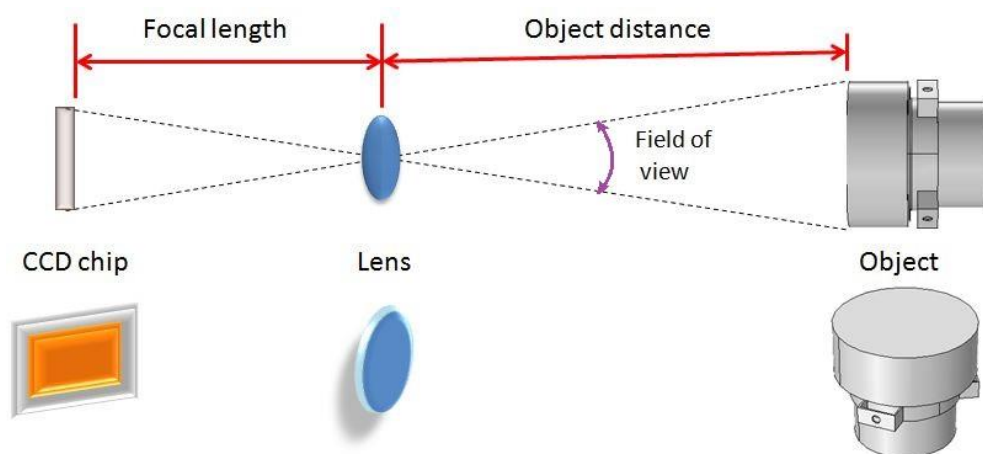


Figure 33: Relationship between chip size, lens focal length and field of view

From the illustration above we can observe a relationship between field of view, size of CCD and focal length of lens. It is clear that bigger field of view can be given with bigger size of CCD sensor or with increasing of distance to object. Also parameters of lens can be changed to reach required field of view. And it is important to find a compromise between these parameters for normal images.

Another important point, that has to be taken in account, is lens focusing. The ability of well focusing of lens makes image sharper. Depth of focus (also called range of sharpness) is a complex function with such arguments as: focal ratio, focal length of the lens, CCD format size, objects size and so on. As we can see, it is a function of many factors. Detailed description of relations between these parameters is beyond the scope of this work.

For understanding the basic principles of measurement with camera, the camera will be visualized as a positive lens and a sensor located on focal plane of the lens.

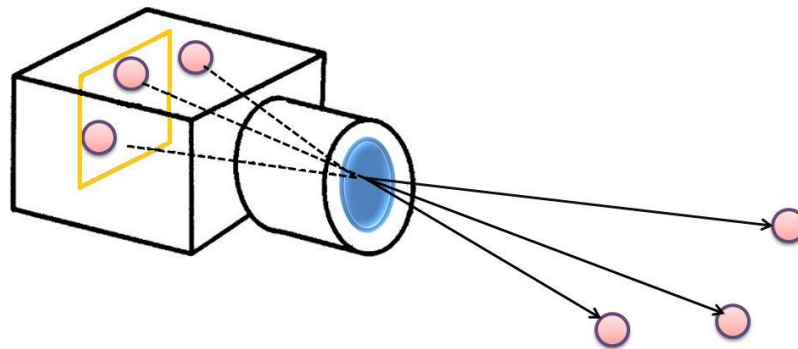


Figure 34: *Targeting the objects by pin-hole camera*

Figure above shows the detection of a few targets which are imaged by the camera. It should be noticed that not all points are detected by CCD sensor (illustrated as orange frame). The depicted arrows call lines of sight (in [13] is described as a chief ray through camera's lens, radiating to the object). If the placement of camera is known, it is possible to find out the spatial coordinates of sight line vector. Then the coordinates of investigated point can be established. But for determination of point's coordinates it is necessary to resort to triangulation technique proposed in next section.

3.3.2 *Triangulation*

Analytical photogrammetric triangulation is a method, using numerical data, of point determination involving the simultaneous orientation of all the photographs and taking all interrelations into account [11]. By mathematically intersecting converging

lines in space, the precise location of the point of interest can be determined (see **Figure 35**).

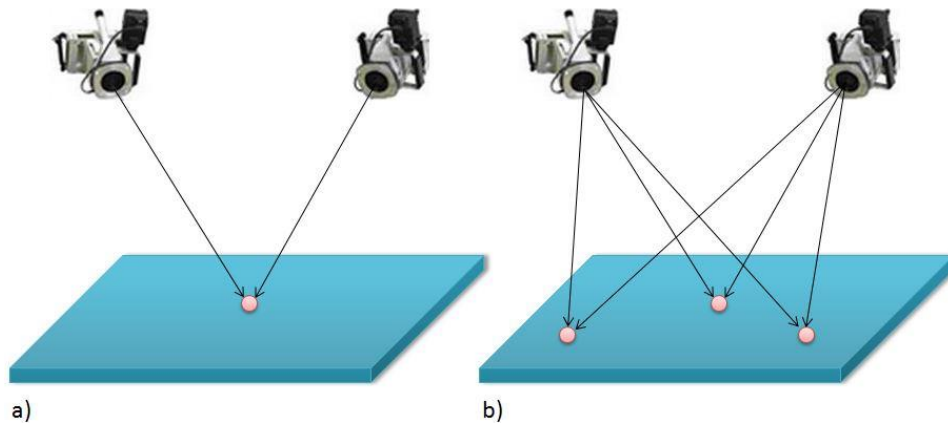


Figure 35: *Single a) and multiple b) target triangulations*

Figures above present to overview an example of using of triangulation principle in photogrammetry. With respect to our application, case with multiple targeting will be used for identification of spatial coordinates of attributes of deflectometry measurement.

A line of sight can be developed from pictures taken from at least two different locations and measuring the same target. As has been said in previous section, if the position of camera is known, the spatial coordinates of object can be determined. For this aim, lines of sight (from each image) can be mathematically intersected to produce the coordinates of each targeted point.

In description of different concepts of photogrammetry measurement, position of camera has been assumed as given. The section after the current describes the procedure called resection, which is aiming to determine a camera location and orientation in 3D measurement.

3.3.3 *Resection*

Knowing of exact location of camera and its orientation (aiming) is an important point in the identification of coordinates of an object in three-dimensional space. All spatial coordinates of points that are known from photographs are used for calculation of final position and aiming of the camera. The position of camera is defined by xyz -coordinates and the orientation is defined by aiming angles (see **Figure 36**).

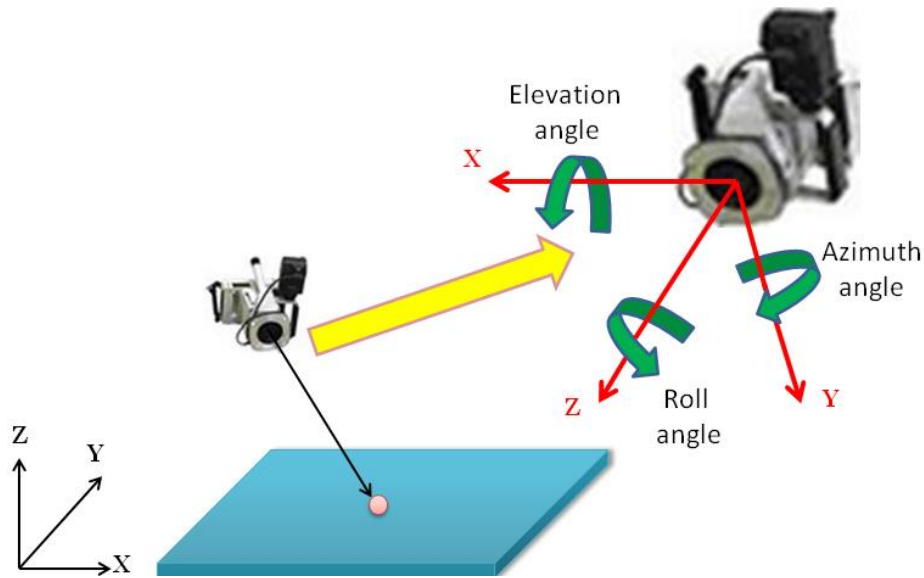


Figure 36: *Coordinate system of camera*

It is important to have information about both the position and aiming direction. Figure 36 makes clear that knowing only the position of origin of camera coordinate system is not sufficient. From the same location camera can be aimed in any direction. It means that three values define target position and six values are needed to define a picture (three angles for aiming and three coordinates for position).

3.3.4 *Bundle adjustment*

From previous two sections the question may arise. On one side, for triangulation, we must know the orientation of the photographs. On another, to orient the photographs, spatial coordinates of targets has to be determined. So, how to get started here? With use of bundle method the problem can be solved.

The bundle method of photogrammetric triangulation, more usually known as bundle adjustment, is of vital importance of to close range photogrammetry. This method allows find out coordinates of the object and orientation of the photographs simultaneously.

It is hard to overstate the importance of bundle triangulation in close range photogrammetry. Nevertheless, this method needs some initial information to start with.

In order to get started, the preliminary orientation for each photograph has to be determined. One of the ways is to use reference targets with known coordinates in user-defined coordinate system. Besides measured points on investigated object, photographs must obtain information about reference points. Due to image processing, reference points (targets), with known three-dimensional coordinates, can be detected. From that,

the image location can be determined in space. When photograph is oriented, the spatial coordinates of identified reference points are converted into two-dimensional coordinate system of the image (photograph). From that moment, image has information about spatial coordinates of known (coordinated) targets. The points on investigated object are found by image processing detection algorithm and their spatial location can be figured out relative reference targets in 2D image system of coordinate.

The procedure described above is given more detailed in section 4.3.

4 Implementation

In following part of this text, the practical aspects of performed work with methods described in previous chapter are given. A detailed description of how heliostat model has been modeled in COMSOL Multiphysics is shown at the beginning of this chapter. Subsection 4.2 is aimed to show how measurement of the heliostat prototype was performed in deflectometry laboratory in the Fraunhofer ISE. At the end, realization of photogrammetry tool with use of OpenCV Library is outlined.

4.1 FEM model of heliostat

4.1.1 Geometry

The principal geometry of heliostat structure is given in figure below.

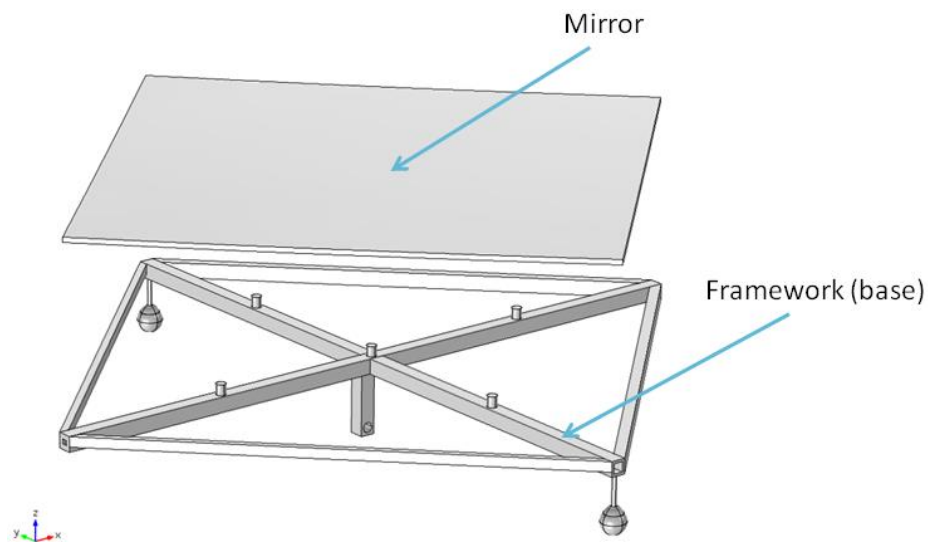


Figure 37: Basic structure of 3D model of the heliostat device

The geometry is based on one domain of framework (base) and mirror plate domain. At the beginning, let's take a look at frame construction. The frame of the device consists of several sub-domains (see **Figure 38**).

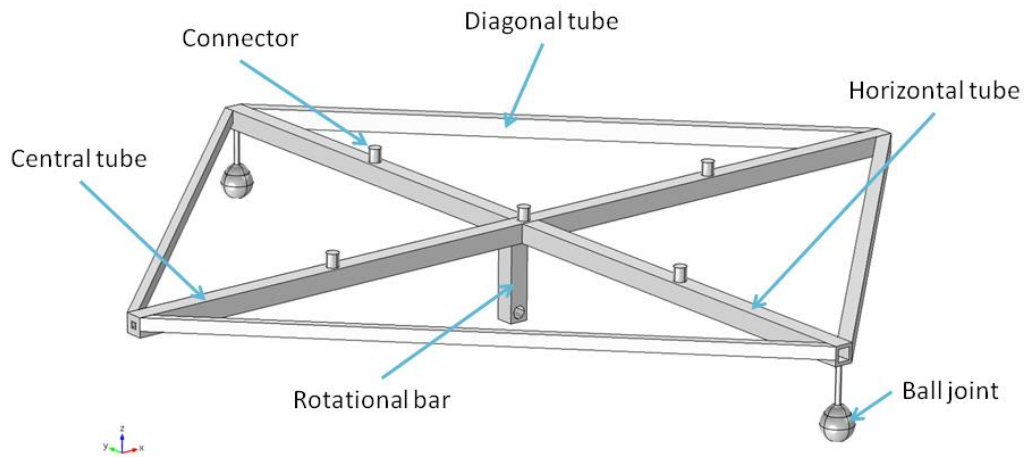


Figure 38: *Frame elements of the heliostat model*

Main central tube with rectangular cross-sectional shape is crossed by horizontal one. Ends of each tube are connected by diagonal tubes. A rod (rotating bar) with circular hole is attached to the central tube. The whole heliostat structure revolves around this rotating bar. It is important to note that this rotational component is placed not in the middle of the central tube. This rotation rod is aimed to make a non-linear elevation axis (see **Figure 39**) with ball joints, which are attached to horizontal tubes. In turn, a ball joint consists of two domains: a bearing stud and socket enclosed in a casing.

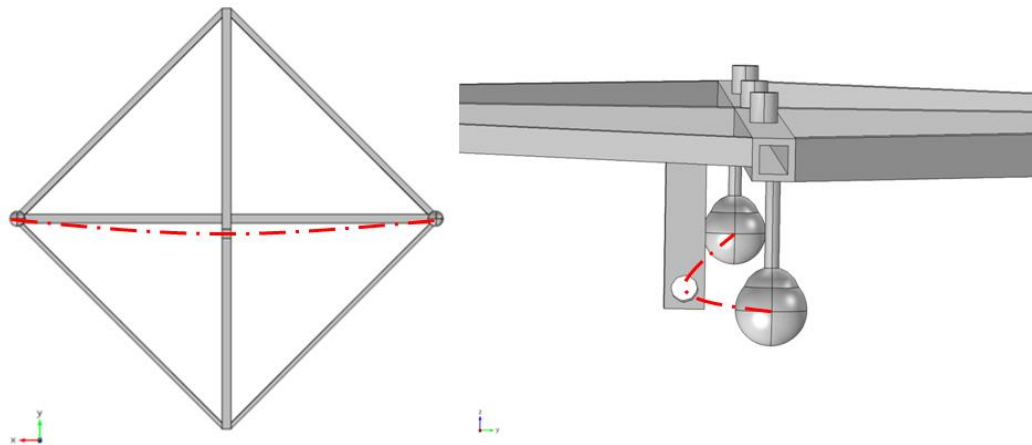


Figure 39: *Non-linear elevation axis*

Such geometric layout allows splitting a heliostat motion in two stages. First stage of heliostat motion is rotation of the frame around non-linear rotation axis. The second stage of motion is intended to cause a certain conditions under which the required deformation of the construction is achieved. At a certain moment of motion (rotation), ball joints do not allow further rotation of the frame. Under such conditions,

the further application of force to the structure leads to deformation. Also, the direction of applied force will result to deformations in different parts of the heliostat's frame. This point will be described more detailed in subsection 4.1.3.

To induce mechanical stress in mirror plate through the deformed frame, the base of the heliostat is connected to the mirror by connecting cylinders (connectors) depicted in Figure 38. The initial shape of the mirror plate is assumed to be deformed for some initial incident angle. In Figure 40 you can see how mirror with deformed shape has been realized in modeling environment COMSOL.

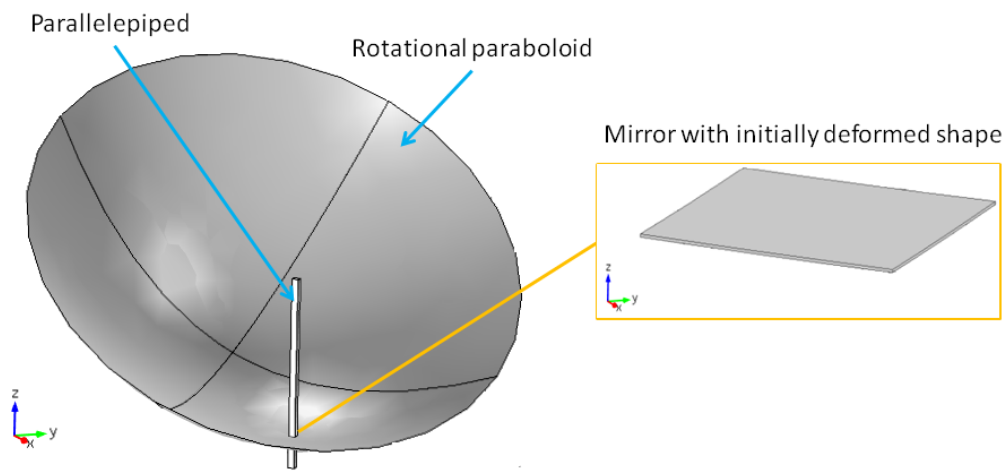


Figure 40: *Geometry of mirror plate as a product of intersection of rotational paraboloid and parallelepiped.*

With respect to required incident angle and slant range, the paraboloid is oriented in such a way that its intersection with the parallelepiped gives required mirror geometry. It is worth to note that lengths of diagonals (vertical and horizontal axis) are the same, but they have different curvature. Therefore, the projection of the mirror has rhomboid shape. In accordance with this, parallelepiped's profile, which intersects paraboloid, has rhomboid cross-sectional shape.

4.1.2 *Material properties*

Next step in modeling is assignment of some material properties to geometric domains. The modeling software COMSOL disposes of a big database of materials [14]. For each material a certain number of parameters, which describes different physical properties, is suggested. The modeling environment requires a definition of three parameters when solving static mechanical deformation task. These parameters are

material density, Young's modulus and Poisson's ratio. The description of last two parameters is given subsection 3.1.2.

In figure below is shown how the physical properties of two materials are assigned to two geometric domains.

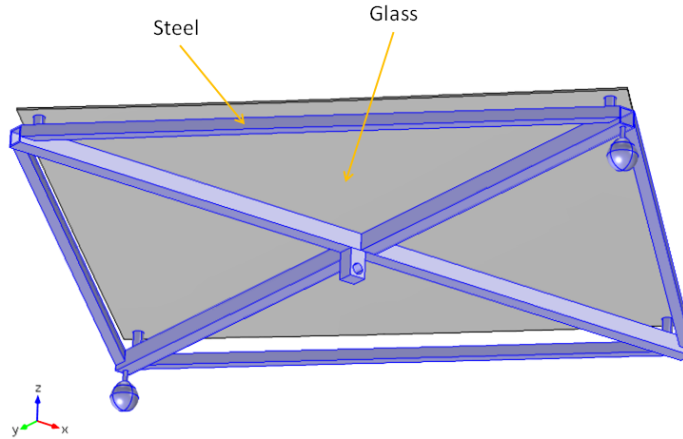


Figure 41: *Geometric domains of the FEM model with assigned materials*

As we can see, for the frame construction (purple domain) is made of steel AISI 4340. Mirror plate (grey) is defined as silica glass. More detailed information about materials is given in Addendum 1. In despite of wide range of materials, only silica glass could be used for mirror plate domain, because only this material had sufficient number of required parameters. For the frame, mechanical properties of standard steel were selected.

4.1.3 *Initial physical conditions*

To make our model to do what it supposed to do, a certain physical conditions has to be defined. Figure 42 and Figure 43 illustrates to what domains what physics have been applied.

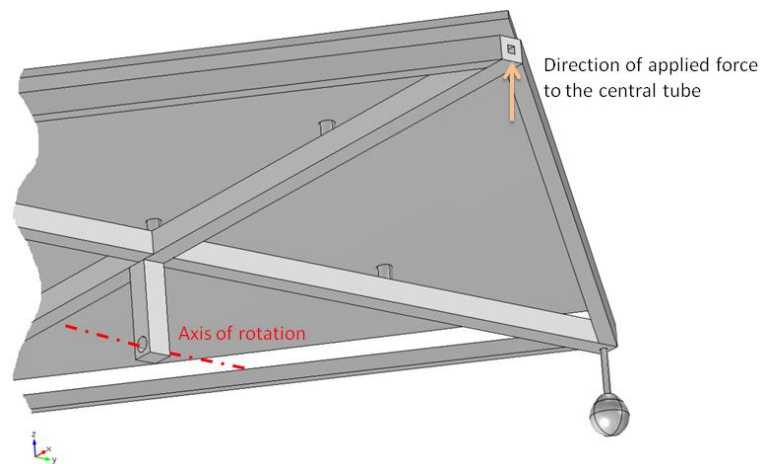


Figure 42: *Direction of applied force and rotation axis of the model*

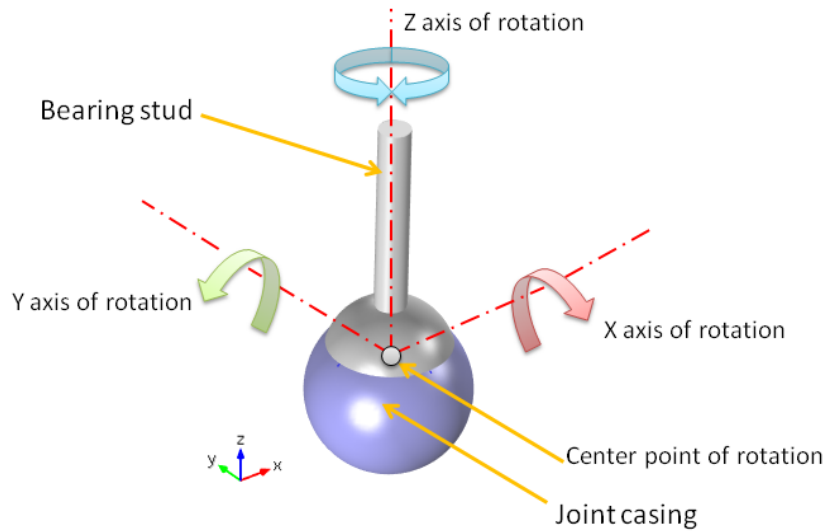


Figure 43: *Ball joint physics (rotation with respect to three degrees for freedom and fixed external boundary)*

In Figure 42, a rotation axis and direction of applied force are illustrated. The internal boundaries (depicted in blue) of the hole are fixed in such a way that the heliostat's frame can only rotate (rotating rod has one degree of freedom) about axis of rotation.

Assignment of physical conditions to spherical joints is shown in Figure 43. In the model, outer boundaries of casing are fixed (depicted in blue). Bearing stud is able to rotate in three directions (has three degree of freedom).

As it was mentioned in geometry chapter, an important role in frame deformation plays the direction of applied force. In Figure 44, mirror shapes with respect to two opposite oriented forces are sketched.

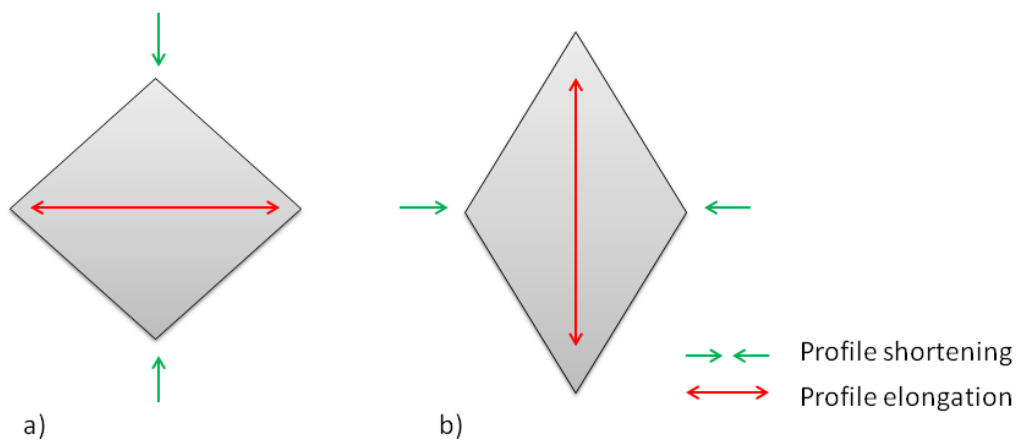


Figure 44: *Reflective surface profile a) with force directed toward to the mirror a) from the mirror b)*

Sketches above demonstrate reshaping of the mirror with respect to applied force orientation. With decreasing of incident angle, mirror in sagittal plane becomes more linear (see **Figure 44 a**) is depicted as profile elongation) whereas in tangential plane curvature is getting more rapid (profile shortening). Reverse principle (see **Figure 44 b**) is valid for increased incident angle where profile elongation in tangential plane is achieved with force whose vector is directed from the mirror.

4.1.4 Mesh

For our model issue a simple tetrahedral element is chosen (see **Figure 45**). It is also possible to use other elements at some parts of the model structure, but it requires essentially user effort. Since we are interested in deformation quality of the mirror (its surface) it is necessary to reach better mesh quality in this domain. Quality of the mesh in frame structure is not important for us, therefore for this domain, mesh can be coarser (number of elements is small). This allows use computational resources mainly for surface deformation task. Example of mesh quality of the model is presented below.

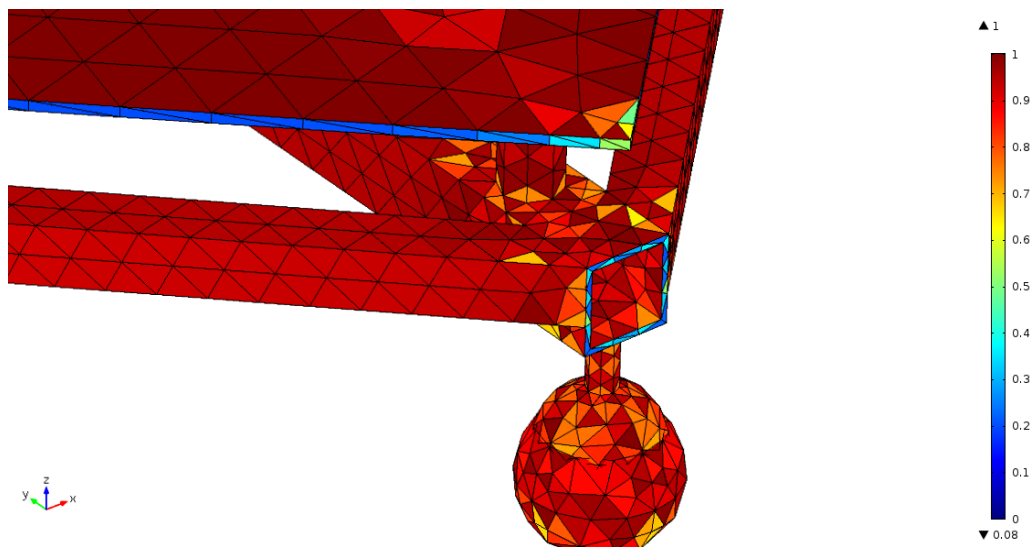


Figure 45: *Mesh quality of part of the model*

Regions with index 1 (imaged as dark red tetrahedrals) represent model components with best mesh quality. Groups with orange (almost yellow) elements signalize about their poor quality and solution in these tetrahedrals can be inaccurate. For accurate solution, mesh has to be refiner in regions where the field gradients whose solution is sought is high. Also, it is worth to say that mesh quality is defined by minimal quality of mesh element. In Addendum 2 the mesh statistics of specular surface of the heliostat device is given.

When the geometry is meshed, the model is prepared for simulation procedure.

4.1.5 Post processing

The result of simulation of the heliostat structure can be observed in Figure 46.

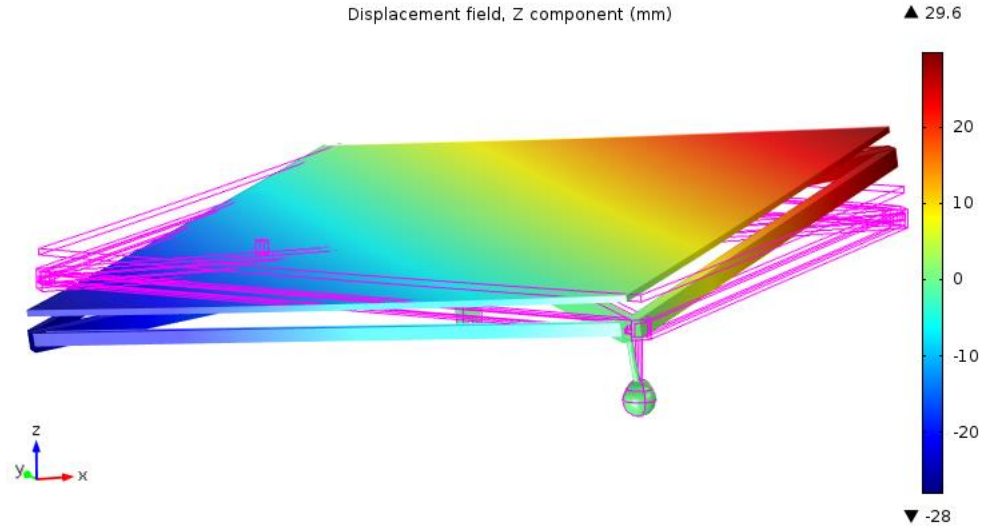


Figure 46: Model displacement in Z component

In this illustration, deformation in z-displacement of the whole geometry is presented. Violet contours display initial state of the model. Model displacement in z-direction is given with rainbow coloring. For evaluation of 3D model quality, it is necessary to compare deformed surface of the mirror, obtained by simulation, with theoretical surface. Being guided by this, data of spatial coordinates of deformed surface are extracted.

With use of comparison algorithm, which has been written in Matlab, simulated and theoretical surfaces are evaluated. It is worth to note that surfaces can be compared only when normal vector of center point of each surface (simulated and theoretical) are oriented in the same direction. In figure below, an example of comparison is shown.

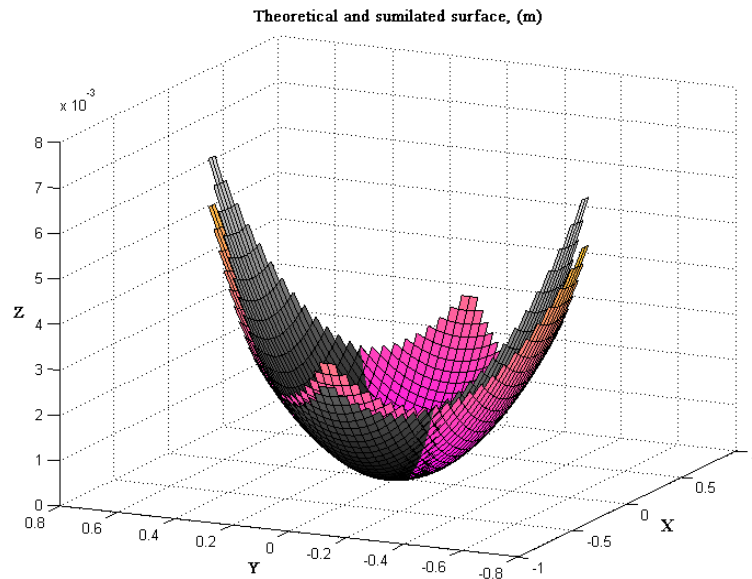


Figure 47: Comparison of theoretical (gray) and simulated (pink) surface

Because extracted data from COMSOL are non-uniformly distributed relative theoretical data, both surfaces are interpolated with the same grid. Criterion for comparison is deviation between orientations of normal vectors of interpolated surfaces (see **Figure 48**).

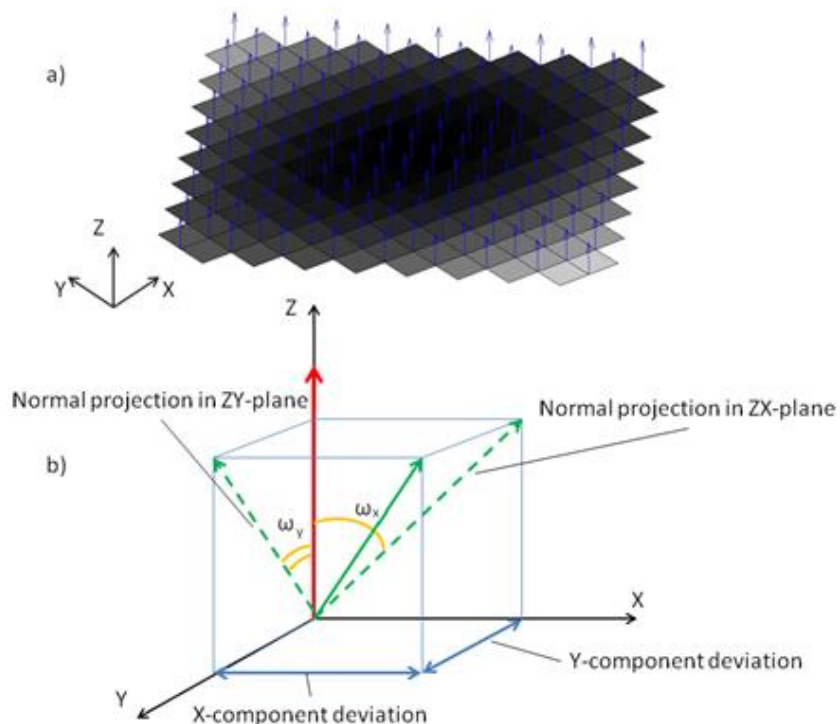


Figure 48: Normal vectors (blue arrows) of interpolated surface a) and angle difference ω of theoretical (red) and simulated (green) normal vectors at the same point on reflective surface in x and y direction b).

In Figure 48 b) can be observed how theoretical and simulated normal vectors are compared. Angles ω_1 and ω_2 determines difference between normal vectors in y and x component respectively. All these differences are calculated in milliradians for each point on the surfaces. Then with use of standard deviation σ_{sd} , which is expressed in milliradians, a variation of these differences relative mean value is determined (see equation (4.1)).

$$\sigma_{sd} = \left(\frac{1}{n-1} \sum_{i=1}^n (\omega_i - \bar{\omega})^2 \right)^{\frac{1}{2}}, \text{ where } \bar{\omega} = \frac{1}{n} \sum_{i=1}^n \omega_i \quad (4.1)$$

Parameter n is a number of points on the surface in which normal vectors are evaluated. The angle of difference is given as parameter ω . The mean difference is expressed by $\bar{\omega}$. Low standard deviation means that difference between angles is close to the mean value. Big value of standard deviation says that angle differences are spreading out in large range of values. A model with best approximation (smallest standard deviation) of required shape is used for prototype design of the heliostat.

An important step has to be performed before simulated surface is compared. It is necessary to compare initial shape of the model with theoretical shape for the same (original) incident angle. It helps to determine similarity of a surface modeled in COMSOL software and surface created in Matlab (theoretical surface).

4.1.6 Parameterization

To be able to generate different variations of heliostat model, parameterization principle is used. Parameterization task is done with “COMSOL with Matlab” option of the COMSOL software. This option allows connect COMSOL Multiphysics to the Matlab scripting environment. Using this functionality following procedures can be done:

- Model parameterization (model properties definition)
- Generation of the model
- Simulation
- Data extraction
- Analysis of simulation products (comparison algorithm)

All steps of model processing, presented above, can be presented in flow chart.

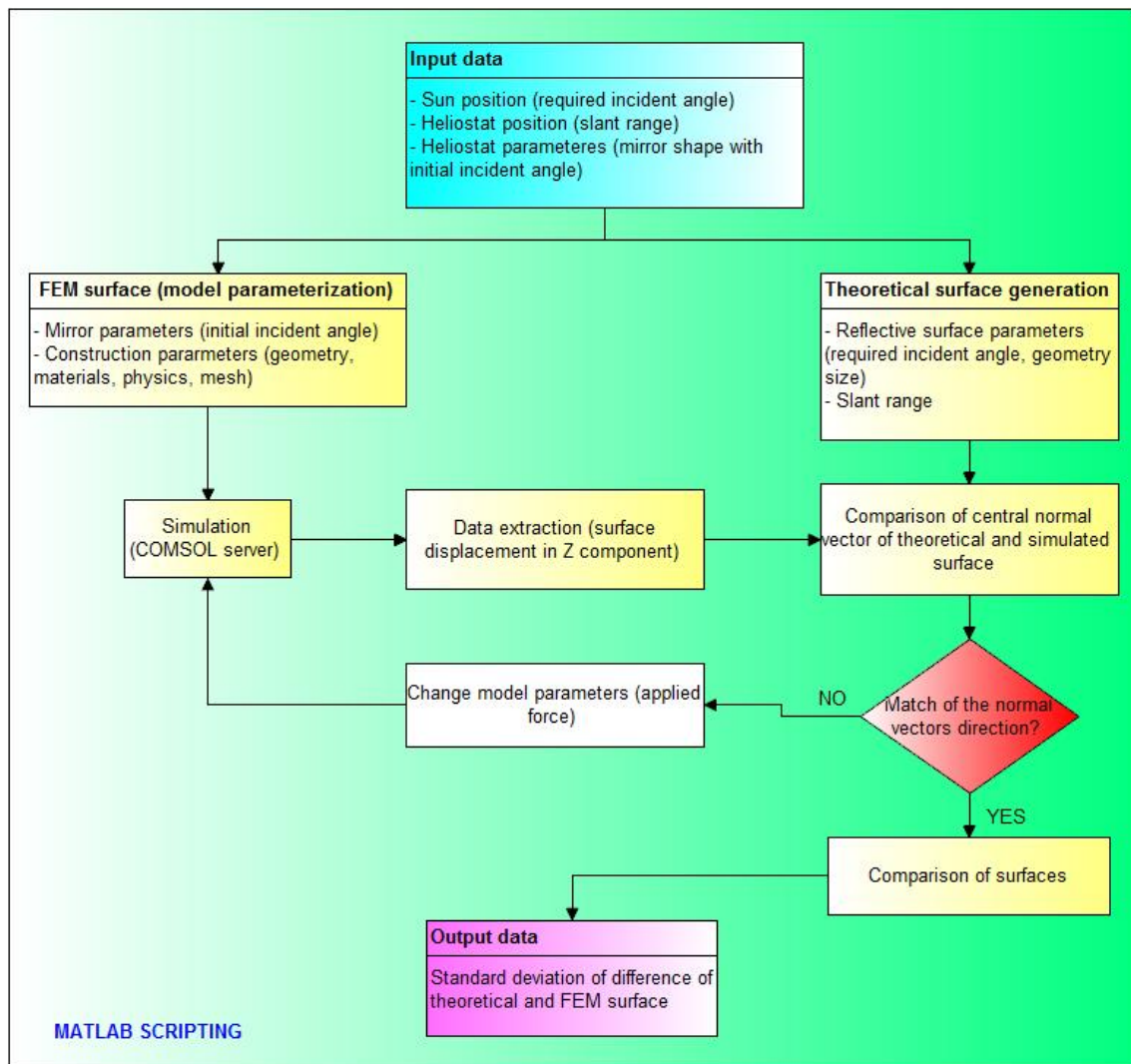


Figure 49: Flow chart of Matlab scripting for comparison procedure of surfaces with parameterized model

The diagram above shows how theoretical and FEM surface are compared with use of Matlab scripting. For each block (theoretical and FEM) a certain number of input parameters are chosen. When model of the heliostat is generated, a simulation process starts. After simulation, data that describes model deformation are processed and prepared for comparison algorithm. Theoretical and simulated surface are compared for matching of the normal vector at central point of the surface (this point is mentioned in previous subsection). If these normal vectors have the same direction, surfaces are compared as it described in 4.1.5.

With use of deflectometry measurement the quality of heliostat prototype (in particular mirror shape) will be determined. Next chapter is devoted to description of deflectometry laboratory.

4.2 Deflectometry laboratory

The Fraunhofer Institute of Solar Energy in Freiburg owns a deflectometry laboratory. The laboratory represents as a large room where some walls are painted in black and white color. White walls (and ceiling inclusively) are used for a projection of a sinusoidal pattern. From side with black wall measuring equipment is located. In a figure below a measurement setup is shown.

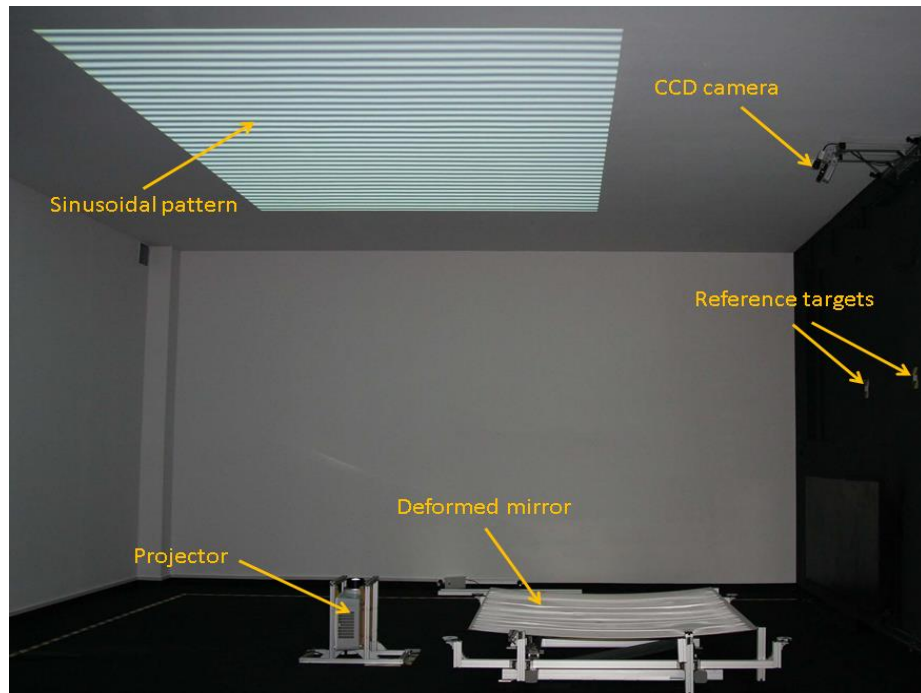


Figure 50: *Deflectometry measurement setup*

The sinusoidal pattern is projected due to beamer Sanyo XGA. The pattern is reflected from the mirror and registered by camera Guppy Pro F-146 with pixel resolution 1392x1040. In Addendum 3 it can be better observable how a certain segment of the pattern (colored in red lines) is visible for the camera field of view through the specular surface. Images obtained by measuring are processed in “Fringe Processor” software (version 3.5). The result of such processing is a curvature and absolute shape of the surface which are computed through differentiation and integration of slope data, respectively [15]. Authors in [16] assert that maximal error of measurement system at Fraunhofer ISE deflectometry laboratory is equal to 0,2 mrad.

The reference targets depicted in Figure 50 are used in calibration measurement procedure, which is the most time expensive part of the measurement. The calibration is performed with use of total station device (see **Addendum 4**). For image processing

software it is necessary to know the information about relative positions of centers of camera's lens point, specular surface and fringe pattern (see **Figure 51**).

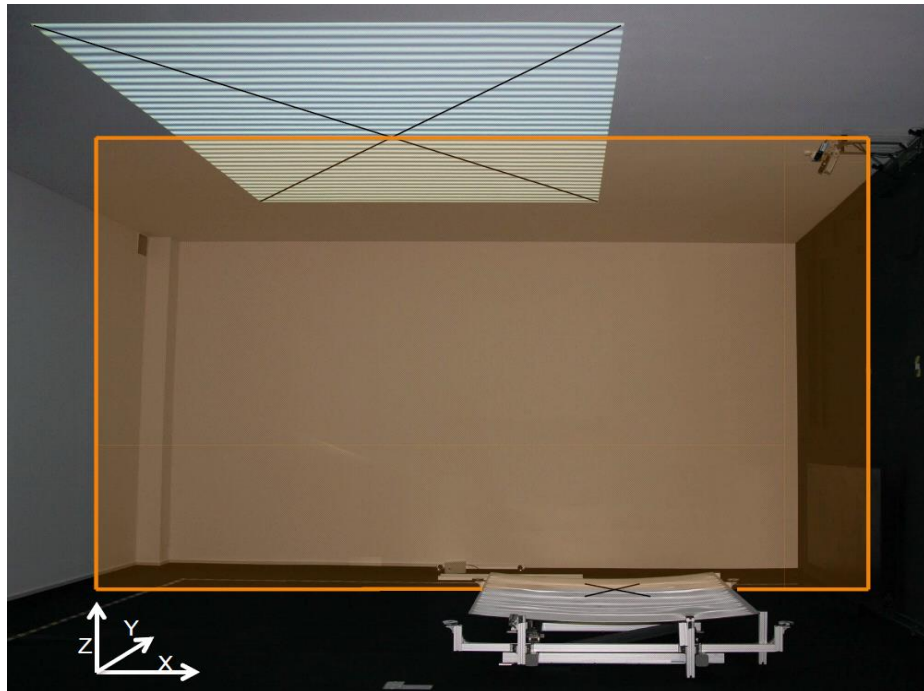


Figure 51: *Relative arrangement of objects of FRT measurement*

Therefore, positions of the objects are measured relative reference targets (with known spatial coordinates) and in further, obtained data are processed in such a way that center of the surface is an origin of system of coordinates. Camera and fringe pattern positions relative this system of coordinates are used in calibration settings of processing software (see **Addendum 5**). Also it is important to note that central points of the objects have to be in one plane (shown as orange rectangular) as it depicted in Figure 51.

Next kind of calibration that has to be executed is camera calibration. This procedure is described in next part of this text.

4.3 Photogrammetry technique implementation

The goal of this section is to describe how principles presented in subchapter Photogrammetry3.3 are realized with use of OpenCV (Open Source Computer Vision Library) and C++ programming.

OpenCV consists of different modules, which can be interpreted as static libraries. For photogrammetry task a module called “calib3d” is used. Functions implemented in this module use pin-hole camera model [17]. The model assumes

perspective transformation in projection of scene view, presented as 3D points, into photograph (image) plane. Such transformation is shown in sketch below.

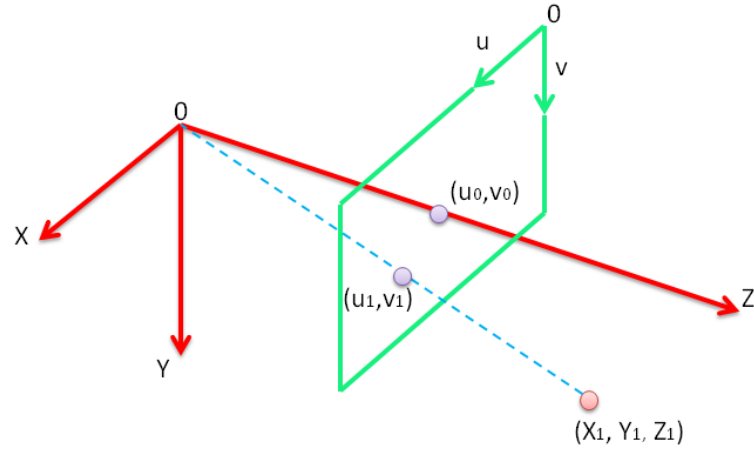


Figure 52: Transformation of 3D coordinates into 2D with use of pinhole camera principle

An object with spatial coordinates X_1 , Y_1 and Z_1 is projected on pixel system of coordinates (green frame) with components u and v . In pixel system of coordinates the object has coordinates designated as u_1 and v_1 . Coordinates u_0 and v_0 represent a principal point that is usually at the image center. By adding this principal point to coordinates u_1 and v_1 the result will be presented with respect to usual convention where origin of the image is placed at the upper-left corner. System of coordinates depicted as red one corresponds to camera system of coordinates as it shown in Figure 36.

With respect to example illustrated in Figure 52, mathematical description of transformation 3D coordinates into 2D, suggested by authors in [18], can be modified in following system of equations

$$s \cdot \begin{bmatrix} u_1 \\ v_1 \\ 1 \end{bmatrix} = \begin{bmatrix} f_x & 0 & u_0 \\ 0 & f_y & v_0 \\ 0 & 0 & 1 \end{bmatrix} \cdot \begin{bmatrix} r_1 & r_2 & r_3 & t_1 \\ r_4 & r_5 & r_6 & t_2 \\ r_7 & r_8 & r_9 & t_3 \end{bmatrix} \cdot \begin{bmatrix} X_1 \\ Y_1 \\ Z_1 \\ 1 \end{bmatrix} \quad (4.2)$$

Transformation of spatial coordinates in 2D system is given by a product of 3D coordinates (green vector), matrix of extrinsic (red matrix) and intrinsic (purple matrix) parameters. Matrix of extrinsic parameters consists of rotation matrix 3x3 with elements r_i and translation vector (matrix 3x1) with elements t_i . This matrix is responsible for resection issue: it represents a camera position relative some static scene. The rotation matrix corresponds to camera aiming while translation vector gives information about

remoteness of the camera position to world (or reference) system of coordinates. Another matrix (with intrinsic parameters), also called camera matrix, contains information about focal lengths f_x and f_y in pixel units. In case if a photograph is taken with a camera scaled by a factor, all parameters described above have to be scaled by the same factor s .

Determination of parameters, which has been described above, has to be performed in a certain order. A simplified algorithm of determination of spatial coordinates of objects of interest from taken photographs is shown below.

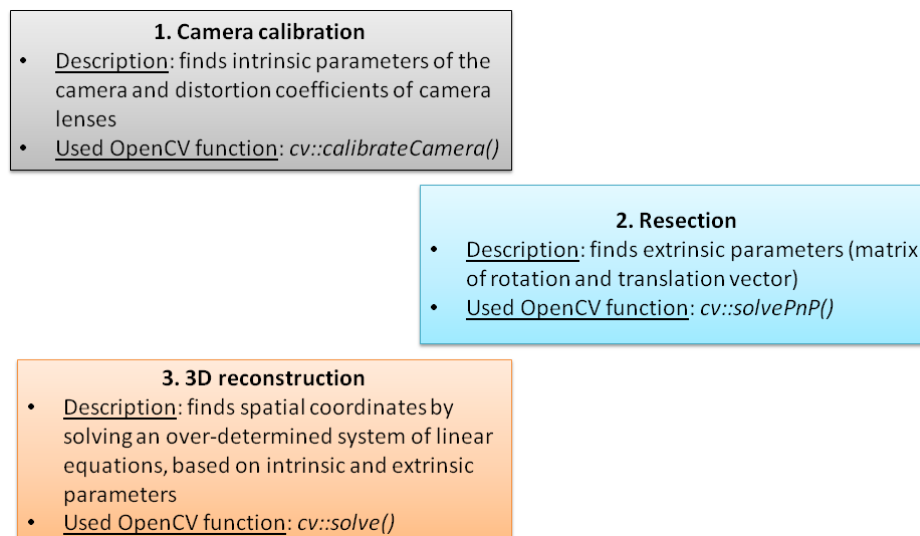


Figure 53: *Simplified photogrammetry algorithm*

At the beginning of photogrammetry measurement camera calibration has to be performed. Usually, chessboard pattern is used as calibration object (see **Figure 54**).

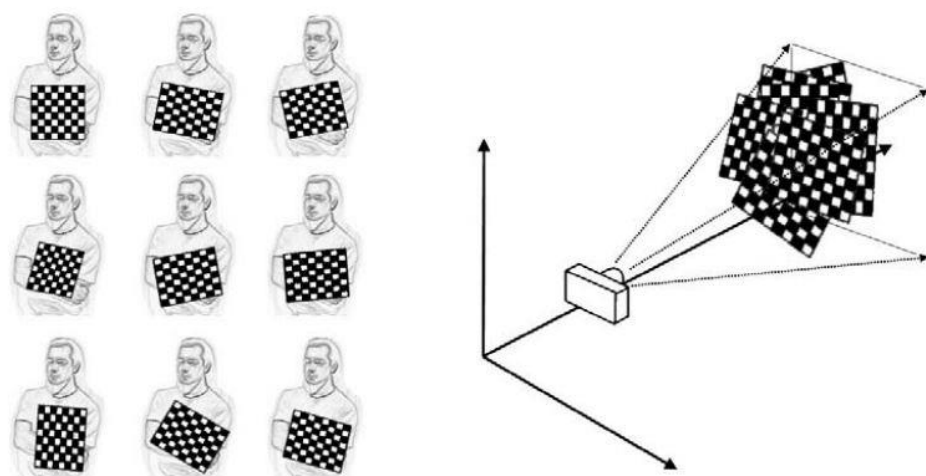


Figure 54: *Photographing (right) of variously oriented chessboard pattern (left)*

Camera calibration algorithm recognizes the pattern and processes images on the subject of pattern distortion. In this manner intrinsic (camera) parameters are found.

The second step of photogrammetry measurement is determination of camera location (resection). Such problem is solved by bundle method. As it mentioned in subsection 3.3.4, preliminary orientation for each photograph of scene of interest has to be determined. For this issue reference points with user-defined spatial coordinates has to be in disposition. The role of reference points plays fiducial markers that are placed in the scene. In this work binary coded markers are used (see **Figure 55**).

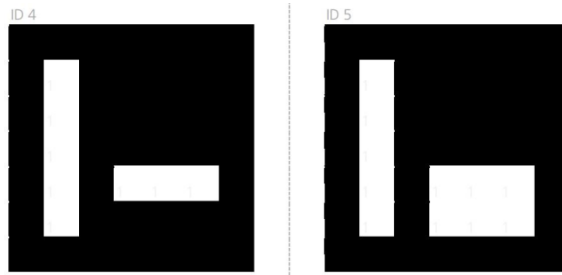


Figure 55: Binary coded markers with ID number

The marker is subdivided into bins and contains black and white values which represent 1 and 0 [20]. With help of marker detection algorithm, these markers are found during image processing. Detected markers are sorted on reference objects and markers with unknown spatial coordinates (in coordinates of these “unknown” markers we are interesting in). The sorting is done through the unique ID number (identification number), which possesses each marker. When reference markers are found their pixel coordinates at photographs is determined. Predefined spatial and found pixel coordinates of reference markers are used as input of “solvePnP” function. The output of this perspective-n-point (PnP) function is sought extrinsic parameters.

After, when photograph position is determined, 3D coordinates of non-reference markers can be calculated. That implies modification of equation (4.2) for one image.

$$s \cdot \begin{bmatrix} u_1 \\ v_1 \\ 1 \end{bmatrix} = \begin{bmatrix} f_x & 0 & u_0 \\ 0 & f_y & v_0 \\ 0 & 0 & 1 \end{bmatrix} \cdot \left(\begin{bmatrix} r_1 & r_2 & r_3 \\ r_4 & r_5 & r_6 \\ r_7 & r_8 & r_9 \end{bmatrix} \cdot \begin{bmatrix} X_1 \\ Y_1 \\ Z_1 \end{bmatrix} + \begin{bmatrix} t_1 \\ t_2 \\ t_3 \end{bmatrix} \right) \quad (4.3)$$

After, this equation has to be rewritten in following form

$$\begin{aligned}
& \begin{bmatrix} r_1 & r_2 & r_3 \\ r_4 & r_5 & r_6 \\ r_7 & r_8 & r_9 \end{bmatrix}^{-1} \cdot \begin{bmatrix} f_x & 0 & u_0 \\ 0 & f_y & v_0 \\ 0 & 0 & 1 \end{bmatrix}^{-1} \cdot s \cdot \begin{bmatrix} u_1 \\ v_1 \\ 1 \end{bmatrix} - \begin{bmatrix} X_1 \\ Y_1 \\ Z_1 \end{bmatrix} \\
& = \left(\begin{bmatrix} r_1 & r_2 & r_3 \\ r_4 & r_5 & r_6 \\ r_7 & r_8 & r_9 \end{bmatrix}^{-1} \cdot \begin{bmatrix} t_1 \\ t_2 \\ t_3 \end{bmatrix} \right)
\end{aligned} \tag{4.4}$$

Equation above can be presented as a system of linear equations. Such system cannot be calculated because number of unknown variables (coordinates X_l , Y_l , Z_l and scale factor s) is bigger than number of equations. That's why photogrammetry measurement requires at least two images for processing. With two and more photographs number of linear equations becomes bigger than number of sought variables. Such over-determined system of equations is solved with use of *solve* function. The result of all steps described in this section is an xml file with spatial coordinates of sought markers. Example of content of output xml file is shown below.

```

<?xml version="1.0"?>
<opencv_storage>
<found_markers>
<_><id>4</id>
<x>1.4677164565681800e-02</x>
<y>2.3028041532008103e-02</y>
<z>1.5149557009793035e-02</z></_>
<_><id>5</id>
<x>9.9222733504319294e-01</x>
<y>5.3136441826573400e-03</y>
<z>1.4618311475476098e-02</z></_>
</found_markers>
</opencv_storage>

```

Figure 56: Example of output results of photogrammetry algorithm (spatial coordinates are given in meters).

Principle described above is realized with use of C++ language in Qt Creator. Subsection 4.3.1 contents the information of how above described algorithm is implemented in graphical user interface (GUI).

4.3.1 Algorithm implementation in GUI

As it was mentioned in previous section, the photogrammetry algorithm has been realized with use of C++ programming language. Since photogrammetry issue is only one of the functions of the GUI, the algorithm is written in individual class, content of which is given below.

Content of Photogrammetry class

```

/// Step 1: Load input .xml file
/// Step 1*: Choose a path and type filename for output .xml file (only manual mode)
/// Step 2: Mode selection (automatic or manual)
/// Step 3: Image preprocessing (sorting)
/// Step 4: Check images on minimal requirements for photogrammetry issue
/// Step 5: Check images on minimal number of objects (markers or targets)
/// Step 6: Check images on appearance of more than one marker with identical ID
/// Step 7: Storing of markers detected in all images
/// Step 8: Check markers on once appearance in the images
/// Step 9: Read spatial coordinates and ID of reference (user-defined) markers
/// Step 10: Check reference markers on once appearance in the images
/// Step 11: Searching of markers that has been detected at least on two images
/// Step 12: Processing of images after sorting
/// Step 13: Determination of center points of markers on the images
/// Step 14: Computation of extrinsic parameters (resection)
/// Step 15: Calculation (reproduction) of spatial coordinates of reference points
/// Step 16: Read spatial coordinates and ID of updated markers form temporary file
/// Step 17: Determination of center points of markers on the images (same as Step 13)
/// Step 18: Determination of spatial coordinates of updated reference markers
/// Step 19: Determination of center points of markers with unknown spatial coordinates
/// Step 20: Computation of extrinsic parameters (resection) for calculation of unknown markers
///          (same as Step 14)
/// Step 21: Calculation of spatial coordinates of new markers (same as Step 15)

```

Figure 57: *Detailed structure of photogrammetry algorithm*

From the photogrammetry class structure we can see that on initial stage of processing, each image is checked on minimal photogrammetry requirements (minimal number of photographs, presence of minimal number of reference points etc.). At this preprocessing stage the algorithm selects image, which can be used for the analysis. Afterwards, main image processing executes. At this point reproducing of spatial coordinates of reference markers is done. This information helps in accuracy measurement determination (user-defined spatial coordinates can be compared with data generated by algorithm). And lastly, the location of markers with unknown spatial coordinates is figured out.

Before starting a photogrammetry measurement it is necessary to find out camera (intrinsic) parameters. This is done by the camera calibration. A screenshot of calibration setting in GUI is shown in Addendum 6. An example of calibration procedure with use of chess pattern is given in figure below.

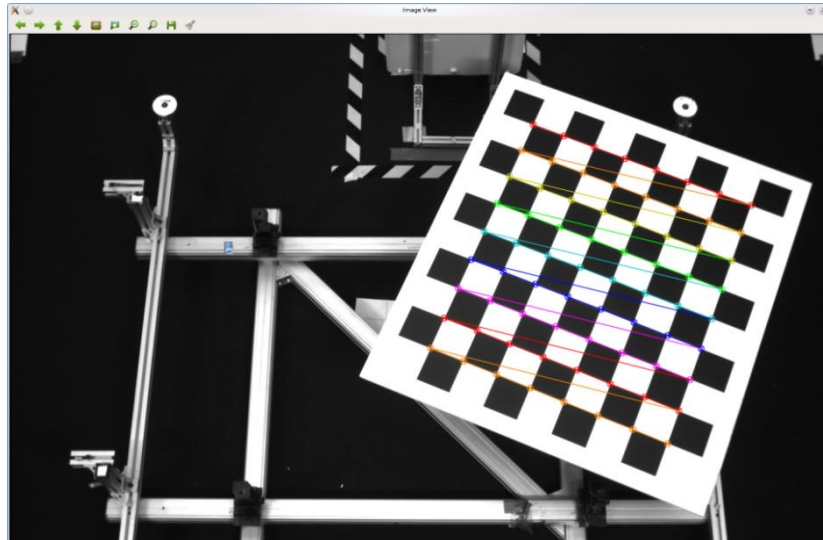


Figure 58: *Processing of the image in camera calibration*

In figure above we can observe how calibration algorithm detects chess pattern (colored lines). The result of calibration is generated in xml format where a big number of camera parameters are generated. For our task only camera matrix and distortion coefficients are the object of interest. When intrinsic parameters are obtained, list with reference markers, which are used in measurement, has to be written. This list is given in xml file in a similar format as it shown in Figure 56.

Last preparation that has to be completed, before processing of taken photographs, is to write an input file with defined paths of components required for photogrammetry processing. With respect to chosen mode/tool (see **Addendum 7**) input file has different structure. In figure below an input file for automatic mode is presented.

```

<?xml version="1.0"?>
<opencv_storage>
<experiment1>
<ImageList>
      /Experiment/ImageList/Photograph1.JPG
      /Experiment/ImageList/Photograph2.JPG
</ImageList>
<ReferenceFile>
      /Experiment/ReferenceMarkers.xml
</ReferenceFile>
<IntrinsicFile>
      /Experiment/IntrinsicParameters.xml
</IntrinsicFile>
<OutputFile>
      /Experiment/OutputFile.xml
</OutputFile>
</experiment1>
</opencv_storage>

```

Figure 59: *Example of an input file for automatic mode of photogrammetry function*

As we can see, the input file consists of four parts. The first one gives the paths to the photographs. The second one indicates a location of the file with a list of reference markers. A filename with intrinsic parameters, generated by calibration procedure, is defined further. Lastly, a path of user required output file is shown at the end of the input file. The difference between automatic mode and manual is that in manual mode list of images and definition of an output file is absent. User is guided by GUI to enter data required by photogrammetry algorithm.

The result of image processing with use of photogrammetry principle is an output file with structure shown below.

```
<?xml version="1.0"?>
<opencv_storage>
  <lost_markers>
    </lost_markers>
  <reference_markers>
    </reference_markers>
  <found_markers>
    </found_markers>
</opencv_storage>
```

Figure 60: *Output xml file structure of processed photographs*

The resulting file offers the information in three parts. The first part (orange colored) shows the ID numbers of markers of which the spatial coordinates could not be determined due to the fact that some markers appears only once in the whole set of images. Next result, which is given in green, is reproduced spatial coordinates of reference markers. This information is very important in analysis of measurement accuracy, because these data compared with references defined by user. Spatial coordinates of objects of investigation are generated in section called “found_markers”.

The functionality of implemented photogrammetry algorithm has been tested in this work. Next subsection delineates performed experiments. It helps to formulate certain rules by which photogrammetry measurement has to be guided by.

4.3.2 *Validation of photogrammetry algorithm functionality*

The reliability of implemented photogrammetry algorithm has been tested with series of experiments. The accuracy of photogrammetry measurement has been tested with respect to following parameters:

- Number of taken photographs in range from 2 to 16
- Incident angle in range from 30 to 75 degrees

- Distance to the target (500 mm and 1500 mm)
- Number of reference points in range from 4 to 16
- Distribution of reference points (uniform, non-uniform)
- Geometric layout of the camera (in Addendum 8 camera position relative target with markers is depicted)
- Method of finding of an object location from 3D-2D correspondences (in [17] CV_ITERATIVE and CV_EPNP methods are suggested)

In photograph below a photogrammetry measurement setup is presented.

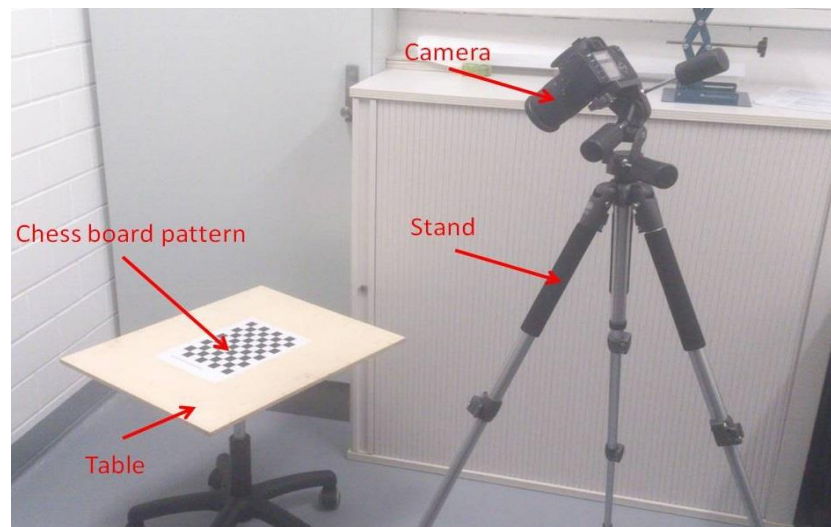


Figure 61: *Photogrammetry measurement setup*

For experiments a camera Canon EOS 350D (pixel resolution 3456x2304) has been used. With help of stand the camera orientation and distance to target has been adjusted relative table with marker pattern (see **Figure 62** and **Addendum 9**) and chess board pattern as it shown in figure above. The camera pose changes relative pattern due to rotation of the table by a certain step. Such approach is used to take every photograph from different location relative chess board (on camera calibration stage) and marker pattern.

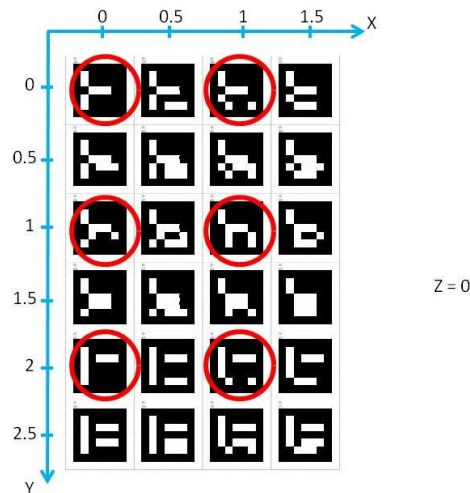


Figure 62: *Sketch of marker pattern with circled reference markers. Scale is defined by user-defined units*

Taken photographs have been loaded in implemented photogrammetry algorithm and processed with respect to tested parameters. For example, we are testing a dependence of number of reference markers on measurement accuracy. Photogrammetry algorithm detects all markers in photographs, but only some of them have predefined 3D coordinates (in Figure 62 depicted in red circles as an example). On basis of it, camera pose is found. Afterwards, spatial coordinates of other markers are determined. Since pattern is given as uniform distributed square markers, the spatial coordinates of “unknown” markers are known for the user. Therefore, these coordinates can be compared with coordinates obtained from the algorithm and measurement accuracy can be analyzed. This test can be executed for arbitrary number of reference markers. The results of all experiments are given in Addendum 10. It has to be noticed that measurement accuracy is determined by maximal error. With respect to this criterion the best result was obtained with maximal error of 0,6055 mm. The error is given as the square root of the sum of squares of x , y and z components.

On basis of performed experiments and analysis of the results, certain rules of use of photogrammetry technique were formulated:

- Measurement accuracy increases with increased number of taken photographs
- The minimal incident angle for marker detection is equal to 45 degrees
- Bigger area is overlapped in one photograph (distance to the target) – less number of pixels contains the object and that leads to worse accuracy

- For determination of camera position and orientation (resection), uniformly distributed reference targets give best approximation of spatial coordinates reproduction
- For precise photogrammetry measurement, geometric layout has to be wide enough (see **Addendum 11**)
- The implemented photogrammetry algorithm has better accuracy with use of CV_ITERATIVE perspective-n-point method

It is necessary to note that all of parameters studied in this work are interrelated. That's mean, bigger number of photographs cannot guarantee an accurate result if these images were taken with bad geometry layout. The same principle is valid for other factors.

5 Analysis of measurements and simulations

5.1 Optimization of the model with FEM simulations (prototype model)

This section gives a description of an optimization of model parameters (in particular geometric proportions) to achieve required deformation. In Table 1 model input parameters are given for optimization issue.

Parameter	Value
Initial incident angle	30 [deg]
Minimal incident angle	5 [deg]
Maximal incident angle	65 [deg]
Slant range	20 [m]
Length of the square mirror	1000 [mm]
Frame Young's modulus (steel AISI 4340)	$205 \cdot 10^9$ [Pa]
Frame Poisson's ratio (steel AISI 4340)	0,28 [-]
Mirror Young's modulus (silica glass)	$73,1 \cdot 10^9$ [Pa]
Mirror Poisson's ratio (silica glass)	0,17[-]

Table 1: *Input data for FEM model*

For this input data a model with initial shape (with respect to initial incident angle and slant range) of the mirror is made. Minimal and maximal incident angles define an extremes at which simulated model is compared to theoretical assumption.

The model is optimized with respect to several parameters:

- Cross-sectional modulus Z of the tubes
- Distance of rotation bar to the center of central tube (see **Figure 66**)
- Height of rotation hole relative joint axis level (see **Figure 66**)
- Placement(layout) of connectors on the frame and their quantity

The first parameter which has been tested is a modulus Z . This parameter is responsible for tube rigidity (stiffness). Since our frame is made of tubes with square profile (see **Figure 63**), the modulus for this kind of profile is given by equation (5.1).

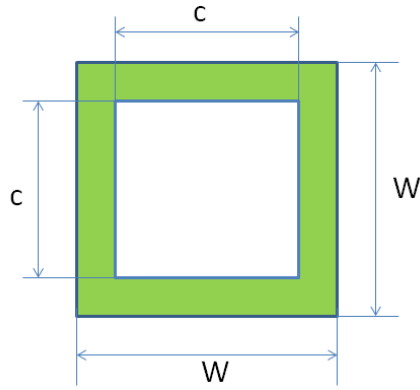


Figure 63: Square cross-sectional profile of the tube

$$Z = \frac{W^4 - c^4}{6 \cdot W} \quad (5.1)$$

For each tube the cross-sectional modulus is calculated (see **Figure 64**).

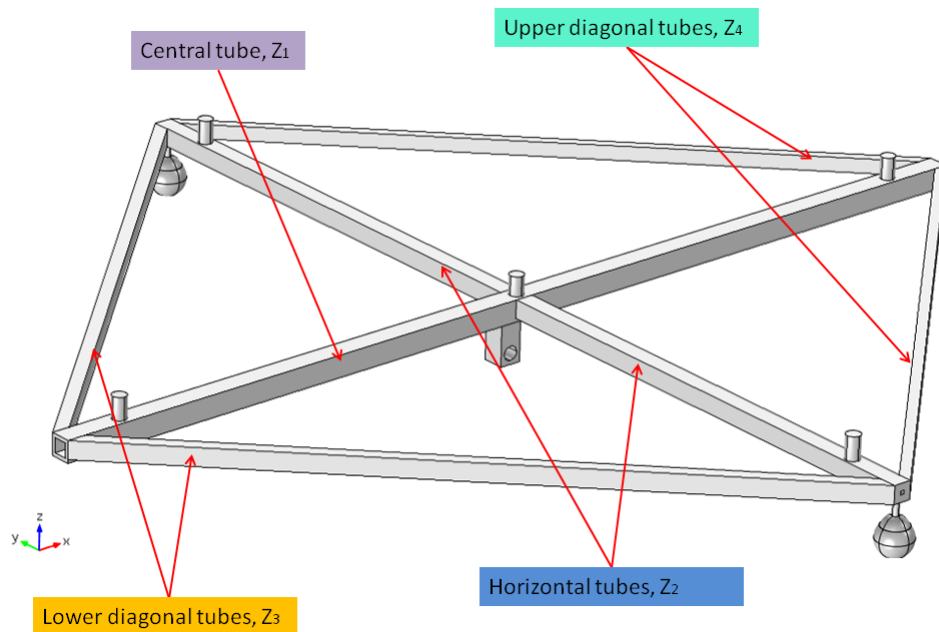


Figure 64: Tubes with designated cross-sectional module index

Modulus Z of the central tube is assumed to have a coefficient 1. Other tubes are given by the product of division their values on central tube modulus value. Diagram, which is given in Figure 65, represents the results obtained from the comparison of simulated and theoretical shape of the reflective surface of heliostat. Only a certain square tubing dimensions (width and thickness) are available on the market. From the subset of geometries different combinations were considered (see **Addendum 12**).

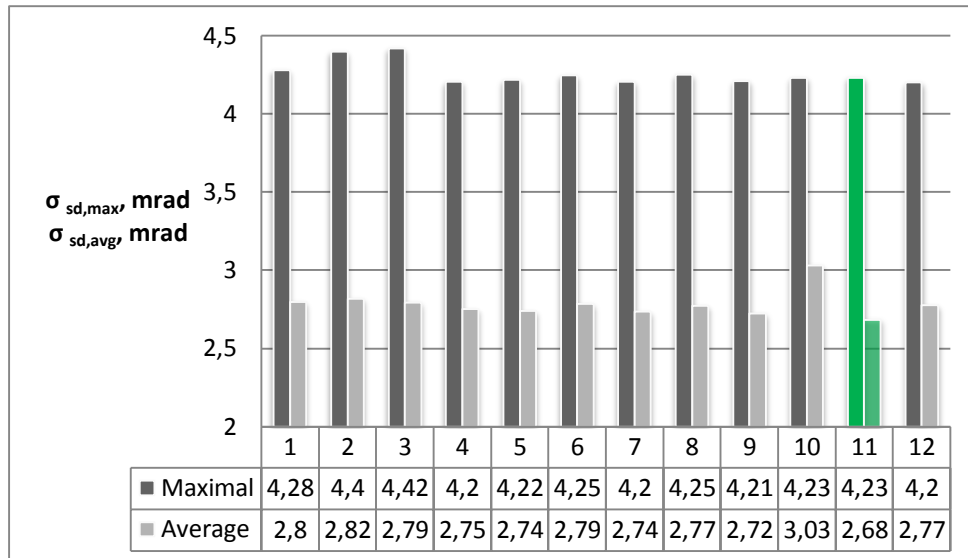


Figure 65: Maximal and average standard deviations with respect to geometric ratio of cross-sectional modules. Green bars indicate the optimal ratio of maximal and average standard deviations

The diagram is presented with respect to maximal and average values of standard deviations. The results with index 11 are taken as an optimal. Ratio with such combination of cross-sectional modules has lowest average deviation and has the sixth lowest maximal error. More detailed information is given in Addendum 13 where standard deviations $\sigma_{sd,x}$ and $\sigma_{sd,y}$ present a deviation at extreme points (minimal and maximal incident angle) between theoretically computed and simulated surfaces. Standard deviations in tangential and sagittal plane correspond to indices x and y respectively. At the end of section 4.1.5 was mentioned that it is important to compare mirror shape created in COMSOL and shape generated in Matlab. Such comparison allows detect the error between these models and say how model that has been created in FEM environment is reliable. For incident angle of 30° standard deviation $\sigma_{sd,x}$ is equal to 0,0303 mrad in tangential plane. In sagittal plane $\sigma_{sd,y}$ is equal to 0,0273 mrad. Model with best results is used in next optimization step.

Next point of optimization task is dedicated to optimal non-linear axis. The curve of non-linear axis can be adjusted by two distances as it shown in Figure 66.

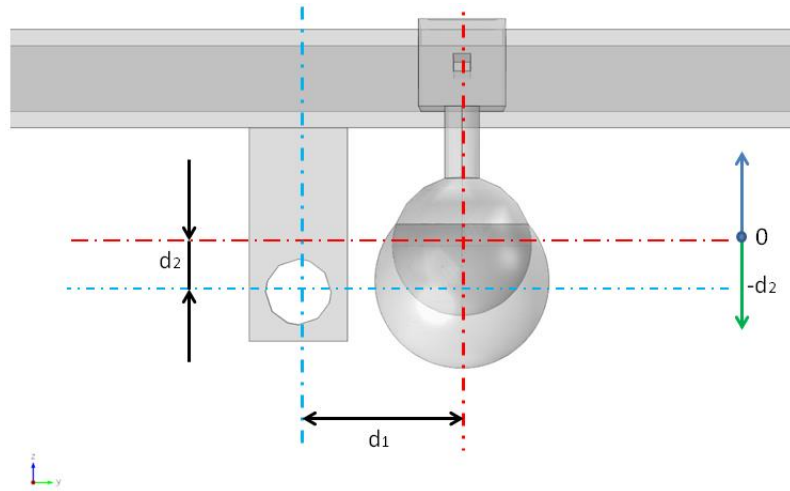


Figure 66: *Non-linear axis adjustment. Red orthogonal axes illustrate the center of the central tube and joint axis level. The blue system defines a location of the axis of rotation in rotation rod*

Parameter d_1 defines distance of rotation bar to the center of central tube. Height of rotation hole relative joint axis level (red horizontal dashed line) is designated as d_2 . Negative sign of this parameter (depicted on the right side of the figure) says that center of the hole is placed lower than ball joint rotation axis. Positive d_2 means that the axis of the rotational bar is above the joint axis level. Following diagrams show how changes of these two parameters (d_1 and d_2) impact on deformation quality with respect to maximal and average standard deviations (in Addendum 14 and Addendum 15 the results are presented in table form).

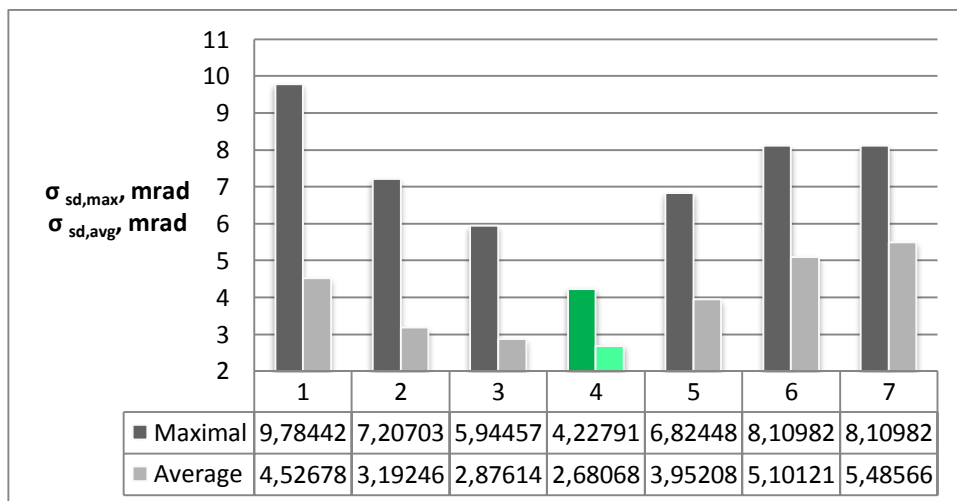


Figure 67: *Dependence of maximal and average standard deviations on increasing distance of rotation bar to the center of the central tube. Green bars indicate the optimal ratio of maximal and average standard deviations*

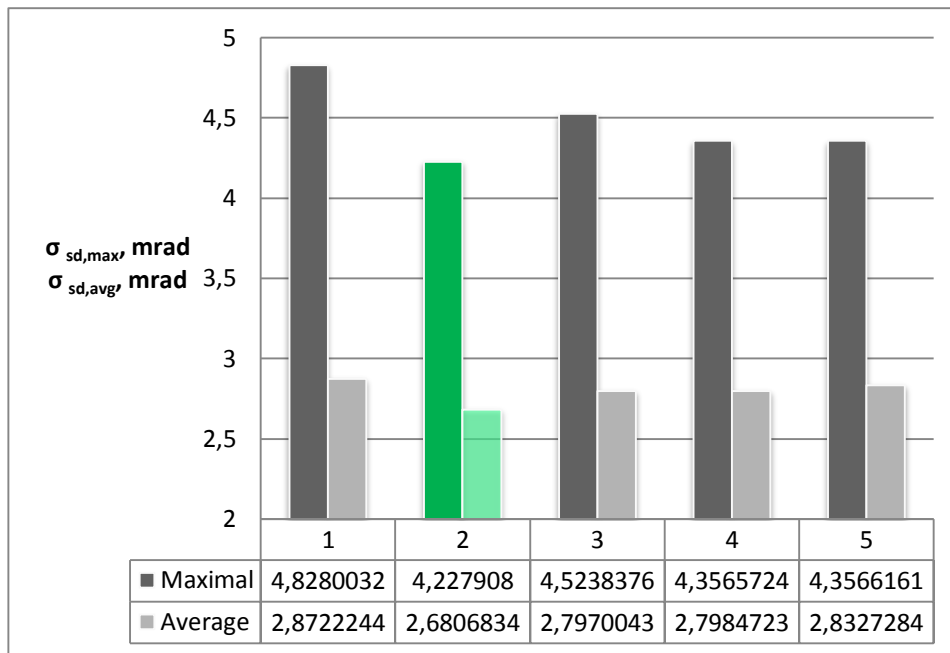


Figure 68: *Dependence of maximal and average standard deviations on the changing position of rotation bar relative to the level of ball joint axis. Green bars indicate the optimal ratio of maximal and average standard deviations*

Green colored rows in Addendum 14 and Addendum 15 have the same optimal standard deviation. Also it can be noticed that the same standard deviations have been registered in the first optimization task (see **Addendum 13**). It leads to a conclusion that initial d_1 and d_2 , which have been used in the first optimization issue, were key factors in the optimization task on the subject of geometric proportions of tubes. In other words, the initial choice of these parameters determines the further optimization of model of the heliostat.

Last point in model optimization issue is layout of connectors. The aim of this task is to determine how many connectors are needed and how they have to be distributed on the frame in order to achieve required deformation. In Figure 69 is sketched an example of layout with use of four connectors (without central connector). Parameter L_1 defines distance on horizontal tubes (sagittal plane) while L_2 is responsible for the location on central tube (tangential plane). Results of performed simulations for different layout are given in Addendum 16.

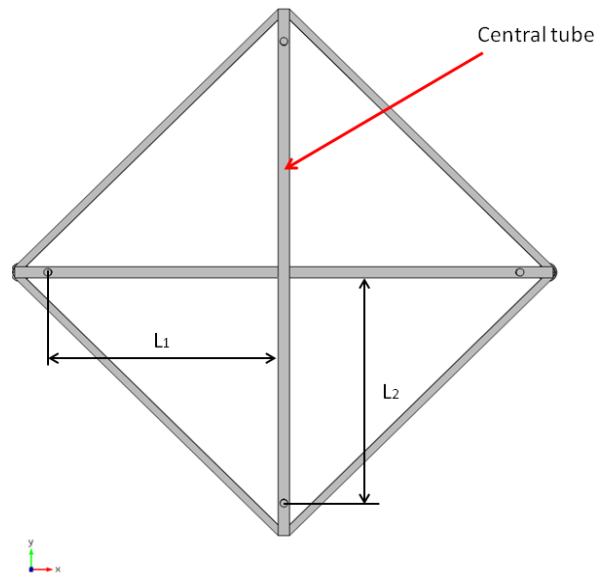


Figure 69: *Layout of connectors*

The best optimal result (marked as green row) is achieved with four connectors and widest layout. This case has lowest average standard deviation and it is equal to 2,2508 mrad. The results in Addendum 16 also say that lower standard deviation we have for connectors placed closer to mirror edges. Confirmation of this is the result registered for 5 connectors (marked as yellow row) with biggest values of L_1 and L_2 . It has to be noticed that results, which are chosen as optimal, are taken with respect to minimal applied force, which is necessary to achieve the desired mechanical stress.

Results obtained by analyzing the model optimization are taken into consideration when creating the prototype. The description of prototype of reflective part of the heliostat is given in chapter 5.2.

5.2 Measurement of quality of the heliostat

On basis of FEM model optimization, a heliostat prototype has been constructed and installed in deflectometry laboratory at Fraunhofer ISE (see **Figure 70**).

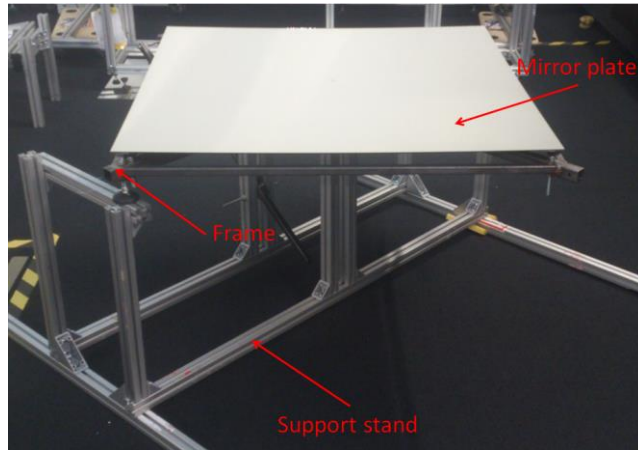


Figure 70: *Heliostat prototype in deflectometry laboratory*

As in FEM model, mirror plate is connected to the frame of the heliostat with use of connectors. A connector is represented as a ball joint, which is regulated by screwing it in the metallic frame (see **Addendum 17**). In turn, the joint is attached tightly to the mirror by adhesive tape. The whole frame of the heliostat prototype stands on the assembled construction. The frame is fixed to the stand also with use of ball joints. The inclination or tilting of the heliostat is controlled by additional rod, which has a fork form (see **Addendum 18**).

In following two subsections the setting, described above, is validated with help of deflectometry principle and photogrammetry technique.

5.2.1 *FRT validation*

The first principle, which has been used in heliostat validation, is deflectometry. The measurement setup with the heliostat prototype is given in Addendum 19. In figure Figure 71 images from the FRT measurement are presented.

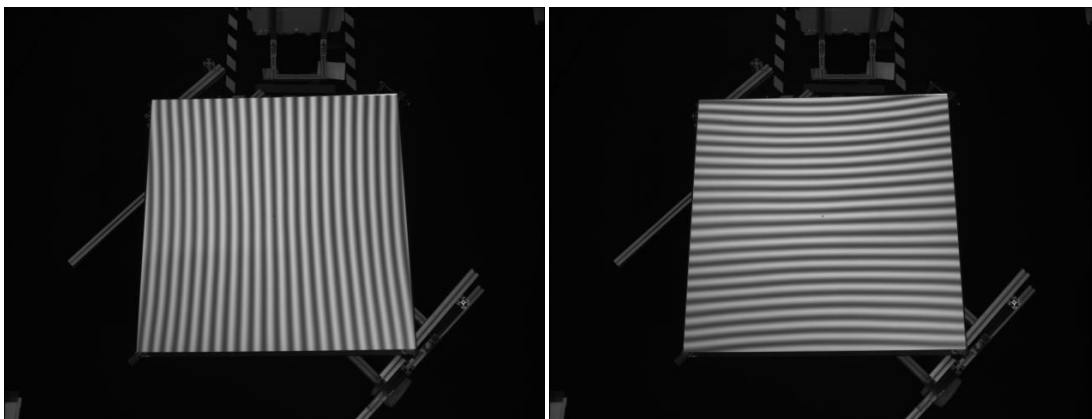


Figure 71: *Registration of the fringe pattern through the prototype reflective surface*

The sinusoidal pattern is reflected due to the mirror and the resulting images are processed in image processing software. The output data of such processing are obtained in form of spatial coordinates with origin at center point of the specular surface. From the images above we can see that mirror was measured in square profile whereas for our issue diamond profile is an object of interest. In turn to this, obtained output coordinates were adapted to conditions under which it is possible to compare measured values with theoretical. The adaptation is performed with use of rotation matrices. At the beginning, all coordinates have to be transformed in such a way that mirror has a rhomboid profile (see **Figure 44**). Then tilting of the mirror is taken in account in subsequent coordinate processing (after the first coordinate transformation angle of mirror inclination is checked in tangential plane). After these preparation steps measured surface is compared with theoretical shape in the same manner as it shown in Figure 47. Because of limitations of measurement (size of the pattern projection did not allow completely reflect the target through the mirror) three measurements were performed. In table below standard deviation in x and y directions (in reference to theoretical shape) is given for a certain set of incident angle.

θ deg	$\sigma_{sd,x}$ mrad	$\sigma_{sd,y}$ mrad
23	2,7101	2,4672
30	2,8639	2,5850
38	2,8837	2,7319

Table 2: *Standard deviation of measured specular surface of the heliostat measured with FRT method*

Analysis of these results is described in section 5.3.

5.2.2 *Photogrammetry validation*

Next technique, which has been used in deformation quality assessment, is photogrammetry. The measurement installation of this technique is given in figure below.

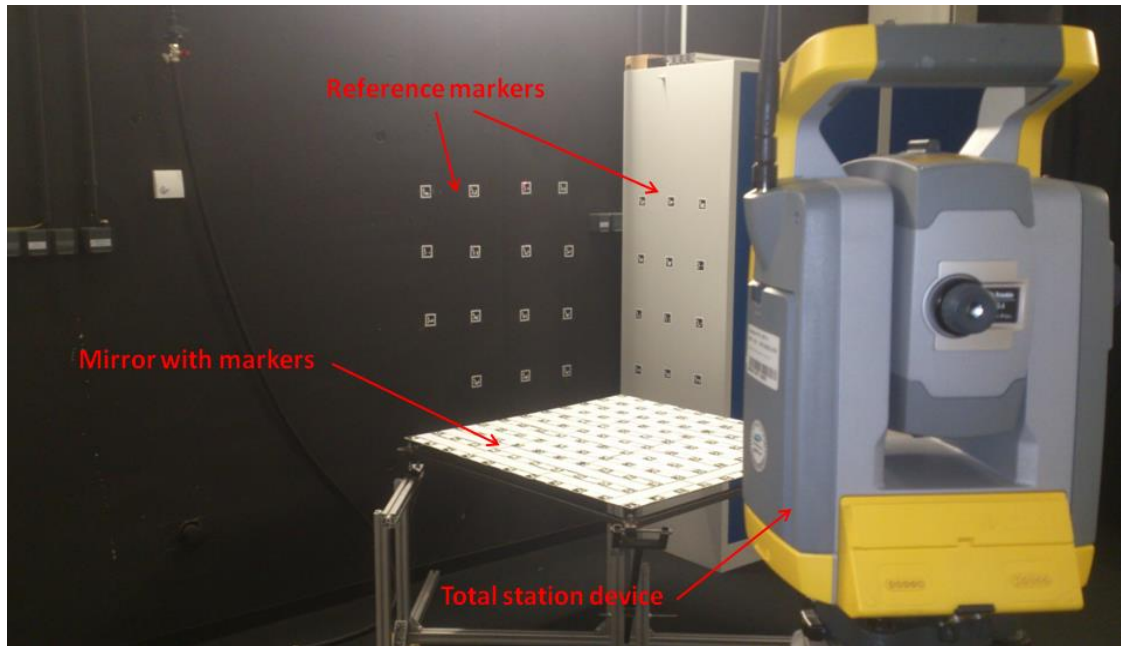


Figure 72: *Photogrammetry measurement setup. Total station device determines spatial coordinates of reference markers (on the wall and locker)*

For this measurement, the same kind of markers and camera as in subsection 4.3.2, were used. The markers were printed on sticky papers, so they could be simply placed in required place. In order to avoid reflections of reference markers in the mirror, the interval between markers on the surface has been covered by paper strips. Also as in FRT measurement, the total station device is used. With help of this an exact position (spatial coordinates) of reference markers, which are placed on the wall and locker, is determined.

During the measurement, it was found that implemented photogrammetry algorithm is not capable to process images in which visible only part of reference markers. Such kind of measurement is called partially overlapping measurement (see **Figure 73**).

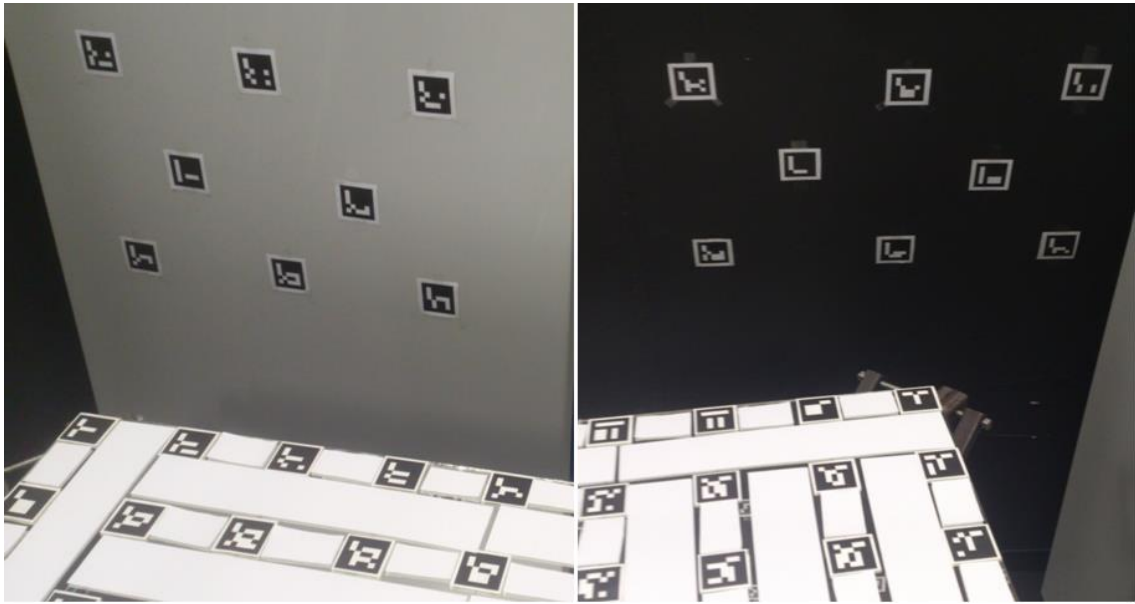


Figure 73: *Example of partially overlapping measurement of segment of the mirror plate*

From the photographs above it is seen how a segment of the mirror is registered with a different set of reference markers (no common references). The algorithm described in this work is supposed to detect all reference markers in each photograph. In this regard, there is a problem with finding of camera position. For this, photogrammetry code has to be modified and adapted for partially overlapping measurement. This kind of measurement is more complex than completely overlapping case (see **Addendum 20**). But at the same time such measurement is more accurate because the object of interest can be segmented and presented in a set of images by parts. This allows more detailed object investigation since measuring equipment (camera) is located close to the scene of interest. For realization of this principle in photogrammetry algorithm it is necessary to determine camera position on basis of sufficient (not necessarily all) number of detected reference markers. It should not be forgotten that every reference marker must be registered at least two times. It could be possible to find out position of the object under investigation only with, for example, two images, which have different set of reference targets. But in this situation measurement accuracy cannot be ascertained.

Further, there were made attempts to make set of photographs where all reference targets are detectable. But in laboratory conditions it was not possible to make images in compliance with the knowledge gained from experiments described in subsection 4.3.2.

5.3 Comparison of measured and simulated results

In figures below, the standard deviations of FEM model and heliostat prototype, which has been measured by FRT technique, are given with respect to theoretical approximation in x (blue diagrams) and y (orange diagrams) directions.

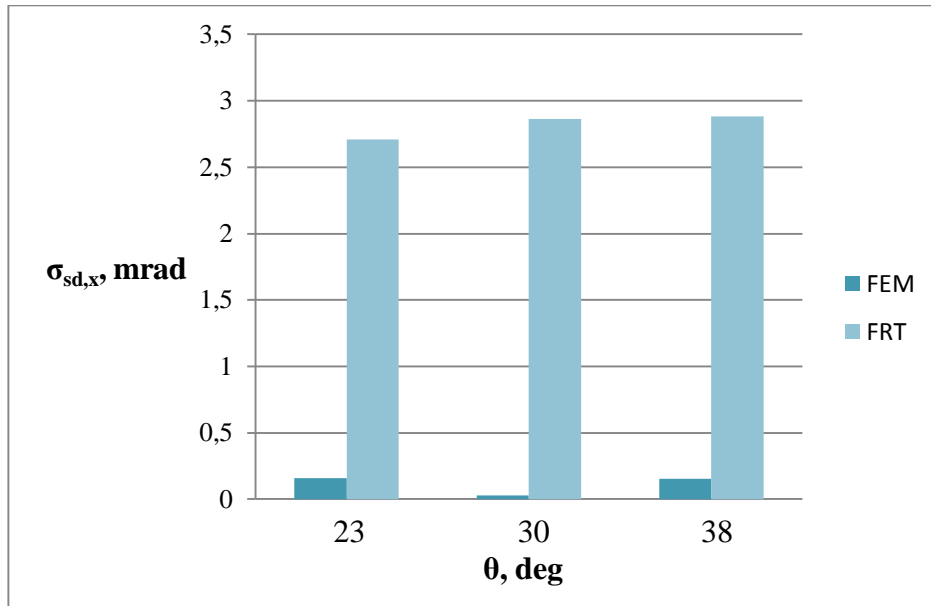


Figure 74: Difference in standard deviations in x-direction between FEM and FRT validation

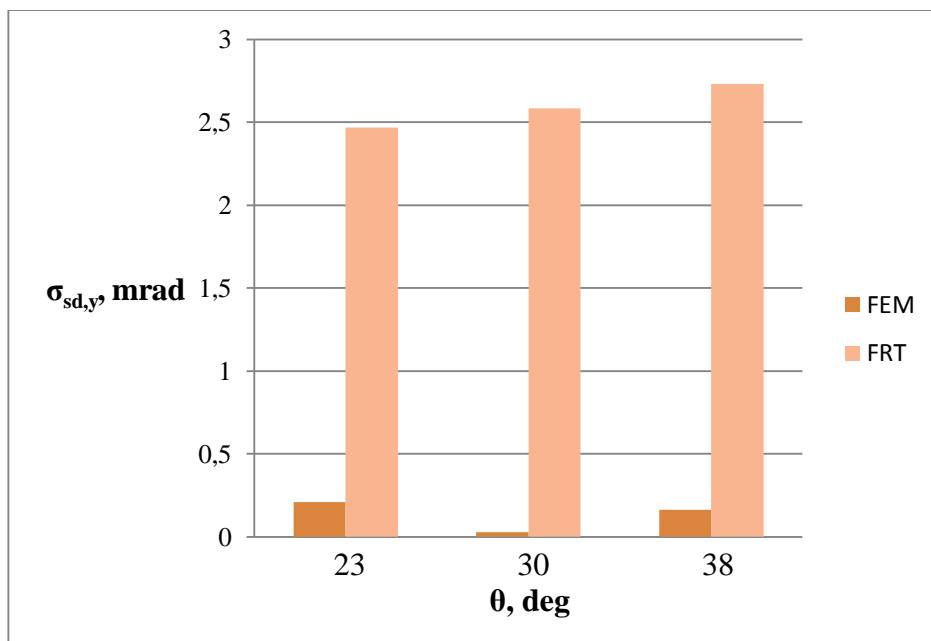


Figure 75: Difference in standard deviations in y-direction between FEM and FRT validation

Since the prototype was measured in a certain range of incident angle (from 23 to 38 degrees), the FEM model has been created (with respect to exact parameters that were used for the prototype) and tested for the same number of angle of incidence. As we can see from the table form (see **Addendum 21**) of results given in figures above, values obtained from the deflectometry measurement are differ from FEM results on about 2,65 milliradians (or 0,15°). Such result may seem to be good enough, but this information does not say how much astigmatism effect is eliminated. For this issue one more calculation has been performed.

For our comparative analysis, effective focal lengths in sagittal and tangential planes have been determined. In Figure 76 the main idea of effective focal length calculation for sagittal plane is shown.

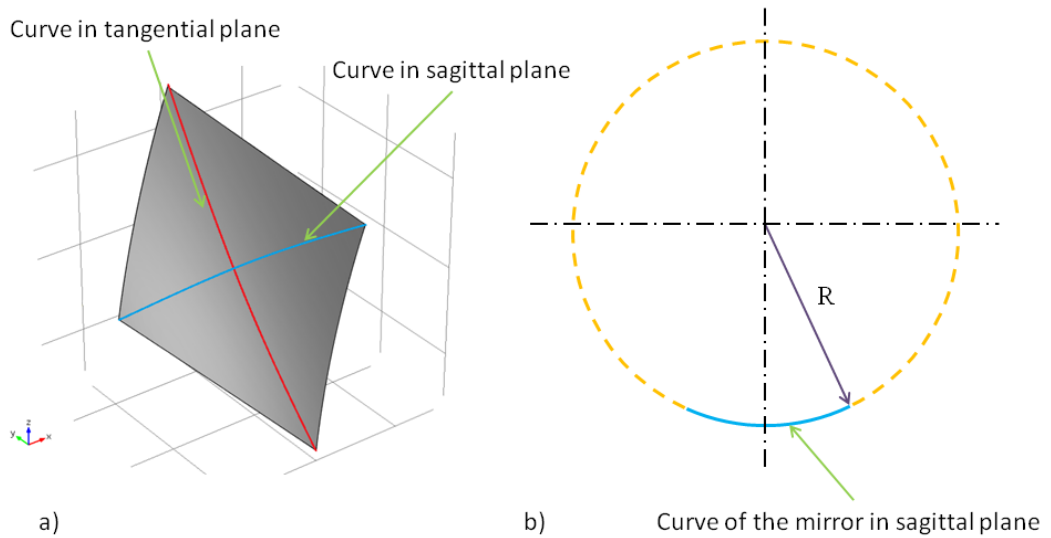


Figure 76: Curves of the heliostat surface in sagittal plane (blue) and tangential plane (red) a) circle fit with use of surface curves b)

Set of spatial coordinates, defining the curve in sagittal plane (blue curve), are used to reside on a circle. The radius of found circle is divided by two. The resulting value is used in calculation of effective focal length as it shown in equations below.

$$F_{sagittal} = \frac{R}{2 \cdot \cos(\theta)} \quad (5.2)$$

$$F_{tangential} = \frac{R \cdot \cos(\theta)}{2} \quad (5.3)$$

Given equations allow to calculate the effective focal lengths in main components (sagittal and tangential plane) of the reflective surface of the heliostat

device. Effective focal lengths calculated by equations (5.2) and (5.3) are presented in figures below.

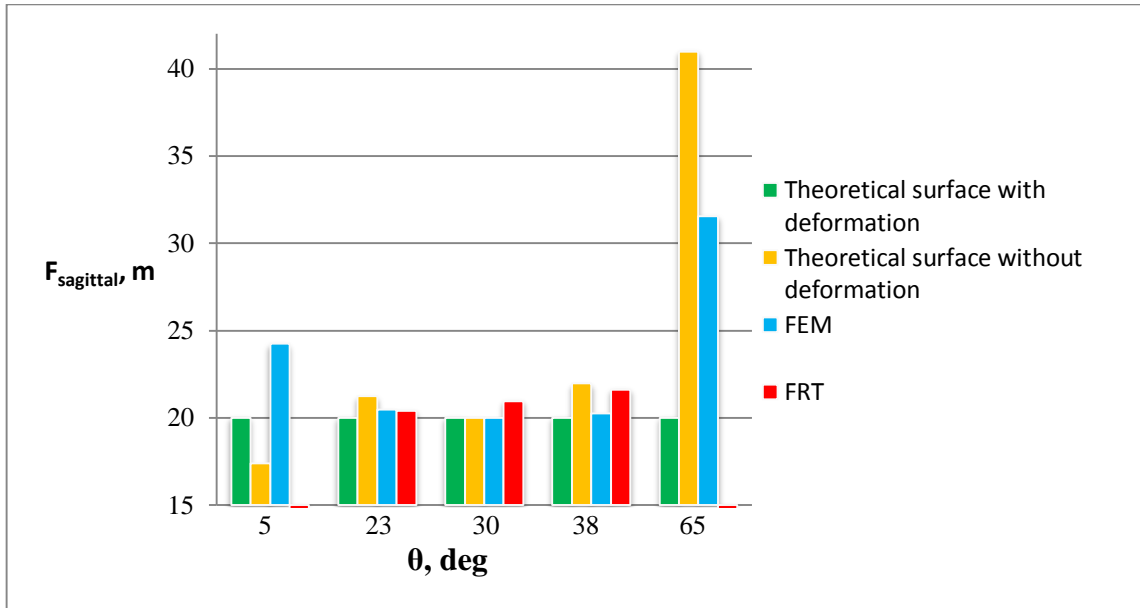


Figure 77: *Effective focal length in sagittal plane*

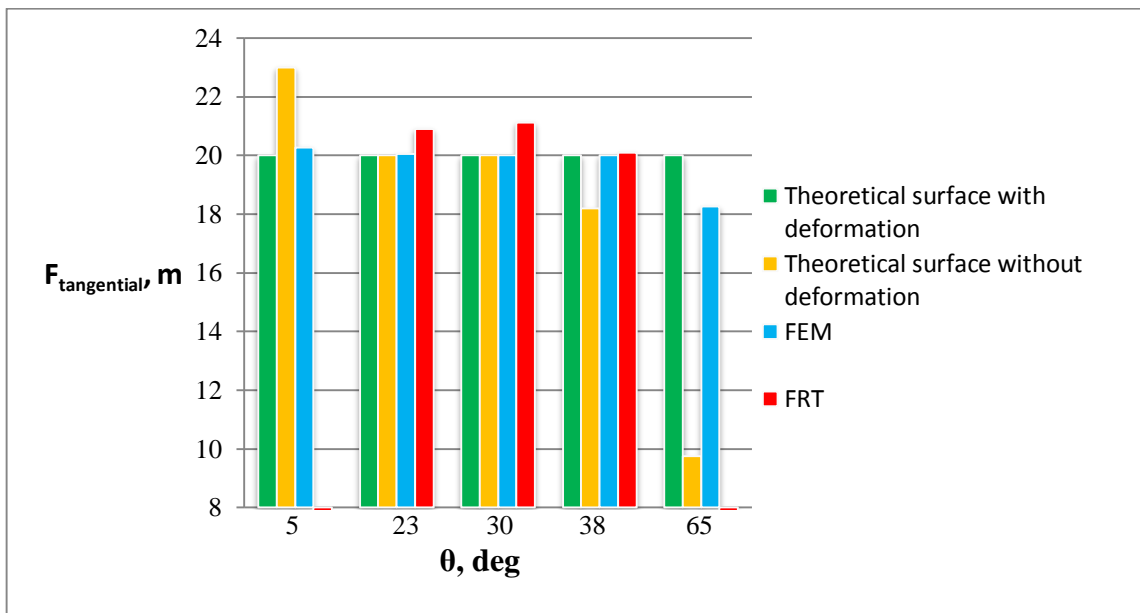


Figure 78: *Effective focal length in tangential plane*

The ideal focal length for both planes is supposed to be 20 meters. In accordance to this, results that are shown in figures above (or in table form in Addendum 22) can be assessed.

Surfaces, named as theoretical, are generated numerically in Matlab software. In connection to this, the difference of about three millimeters with respect to the ideal focal length for initially adjusted incident angle (30°) is caused by interpolation of

spatial coordinates. This error can be neglected with respect to required focal length. Therefore, surface implemented in numerical software can be taken as an exemplary (or theoretical) surface.

From Figure 77 and Figure 78 it can be seen how theoretical focal lengths with and without deformation of initially deformed shape differ. Decreasing of angle of incidence for non-deformed case makes focal length shorter in sagittal plane, whereas elongation of the focal length is observed in tangential. Focal lengths of theoretical surface with deformation almost perfectly coincide for each tested incident angle.

Good convergence of effective focal lengths has been achieved for results generated due to FEM simulations in range from 23 to 38 degrees. The biggest error of about 0,47 meters in sagittal plane has been computed. A significant error in focusing is observed at extreme incident angles. The biggest deviations from the required focal length are registered in sagittal plane. On basis of this we can conclude that at certain stage of mirror movement there is no deformation, so the solar rays are focusing far beyond the target. This is particularly evident on the result shown for incident angle of 65 degrees. The same behavior is seen in best optimization results given in Addendum 16 for 4 connectors.

Decent convergence of focal lengths has been achieved with heliostat prototype. The initial shape of the heliostat device has error of about 1 meter in both planes. But in despite of this and a small range of incident angles, a certain tendency is observed. As angle of incidence increase – focal length in sagittal plane becomes bigger as in descriptions given above. Such situation cannot be observed for angle of 23 degrees because of inaccurate initial shape adjustment. Focal lengths for this angle of incidence has good approximation in comparison with theoretical.

6 Conclusion

In this thesis, an intrinsic optical effect, the astigmatism, seen for all static shape heliostats was reviewed. A continuously changing, section of a continuously changing rotational paraboloid is used to describe the ideal shape of the heliostat surface in dependence of the incident angle of sunlight on the heliostat in order to eliminate the astigmatism effect of the heliostat device seen at the focal spot on the target. A segment with rhomboid profile is extracted from the paraboloid. This segment is taken as a specular surface, which is supposed to focus all solar rays at a point where receiver is located. In numerical software Matlab was implemented an algorithm that generates mathematical model of the surface with respect to a certain number of input parameters (sun position, location of the heliostat in a field, size of the heliostat device, etc.).

Next step of work was to develop a model of the heliostat with use of finite element method in COMSOL Multiphysics and Matlab. The model is designed with parameterization principle, so user can generate required model in programming script. With help of parameterization principle, an optimization stage in FEM modeling was performed. The aim of this stage was to figure out model components for which the mechanical stress, caused by the structure of the model, deforms the mirror surface so it has the best approximation to the theoretical one.

On basis of model optimization the heliostat prototype was installed. The functionality of the prototype was evaluated with use of two techniques: deflectometry and photogrammetry. The first technique was applied in FRT laboratory at Fraunhofer ISE. The deformation of specular surface of the heliostat prototype was measured in two positions. Because of deflectometry measurement limitations, small range of angles of incidence was tested. Even though a small number of performed measurements, the results allow assessing of efficiency of the principle used in heliostat design, the main idea of which was in deformation of the mirror through the mechanical stress caused by non-linear axis of rotation of the heliostat frame. During the analysis, it was found that developed heliostat design works properly and results of the first prototype can be taken in account when creating the modified prototypes of target-aligned heliostat. One of the main conclusions of the analysis is inability to achieve desired curvature of the mirror in sagittal plane for extreme incident angles. In future, it is necessary to carry out a series

of experiments that ascertain for which conditions mirror deformation reaches reduction of the astigmatism effect for wide range of angle of incidence.

The big part of work was devoted to implementation of the second technique applied in heliostat validation. Photogrammetry principle was implemented with use of C++ programming language and OpenCV library. The aim was to determine spatial coordinates of the mirror surface on basis of set of taken photographs of object under investigation. During the image processing was ascertained that realized photogrammetry algorithm is valid only for measurements, in which all points with known spatial coordinates are detectable in each processed photograph. In laboratory conditions was not possible to make such images. One of the ways, how to make implemented technique more universal, is to adapt the algorithm for partially overlapping measurement. The condition for this type of photogrammetry measurement is a minimal number of detected references instead of having all reference in each image.

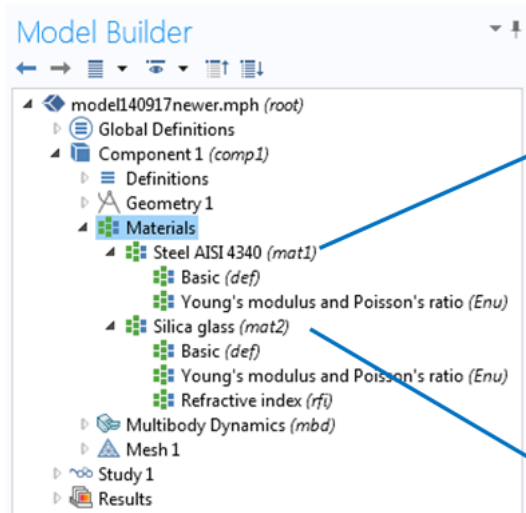
The work described in this paper helped its author to know more about one of the issues of solar tower power plant. Invaluable knowledge and experience were gained in solving of different tasks. Skills in modeling of structural mechanics with use of finite element method were improved. Also, in process of implementation of photogrammetry algorithm, the author improved his experience in object-oriented programming with use of C++.

Bibliography

- [1] J. L. Abatut and A. Achaibou, "Analysis and design of a field of heliostats for a solar power plant," *Solar Energy*, pp. 453-463, 1978.
- [2] M. Wright and P. Hearps, "Australia's 100% renewable energy supply," in *The Zero Carbon Australia Stationary Energy Plan*, p. 45.
- [3] S. Alexopoulos and H. Bernhard, "Solar tower power plant in Germany and future perspectives of the development of the thechnology in Greece and Cyprus," *Renewable Energy*, pp. 1-5, 2009.
- [4] K.-K. Chong and M. H. Tan, "Comparison Study of Two Different Sun-Tracking Methods in Optical Efficiency of Heliostat Field," *International Journal of Photoenergy*, no. Panagiotis Lianos, p. p. 2, 2012.
- [5] R. Zaibel, E. Dagan, J. Karni and R. Harald, "An astigmatic corrected target-aligned heliostat for high concentration," *Solar Energy Materilas and Solar Cells* 37, pp. 191-202, 1995.
- [6] S. S. Rao, "Overview of finite element method," in *The finite element method in engineering*, Elsevier Science & Technology books, December 2004, p. 3.
- [7] C. A. Felippa, "FEM modeling: Introduction," in *Introduction to finite element methods*, 2004, pp. 1-8.
- [8] S. C. Chapra and C. P. Raymond, "Numerical methods for engineers," New York, McGraw-Hill, 2010, pp. 169-173.
- [9] S. Timoshenko and N. Goodier, "Theory of elasticity," New York, McGraw-Hill, 1951, pp. 1-10.
- [10] A. Heimsath, P. Werner, T. Bothe and W. Li, "Characterisation of optical components for linear fresnel collectors by fringe reflection method".
- [11] T. Luhmann, S. Robson, S. Kyle and I. Harley, in *Close Range Photogrammetry*, Dunbeath, Whittles Publishing, 2006, pp. 1-29.
- [12] T. Marz, C. Prah, S. Ulmer and S. Wilbert, "Validation of Two Optical Measurement Methods for the Qualification of the Shape Accuracy of Mirror Panels for Concentrating Solar Systems," *Journal of Solar Energy Engineering*, pp.

- 1-7, 2011.
- [13] M. Harvey, "Fundamentals of photogrammetry," in *Applications of 3D measurement from images / edited by John Fryer, Harvey Mitchell and Jim Chandler.*, 2007, pp. 10-35.
- [14] "COMSOL Multiphysics Reference Manual," November 2013, pp. 515-560.
- [15] W. Li, T. Bothe, C. Kopylow and W. Jüptner, "Evaluation methods for Gradient Measurement techniques," 2004, pp. 300-311.
- [16] A. Heimsath, G. Bern and P. Nitz, "Shape accuracy for solar mirrors - comparison of two methods using fringe reflection technique," in *SolarPACES 2011, 17th Solar Power And Chemical Energy Systems International Symposium, September 20-23, Granada, Spain, 2011.*
- [17] "Camera calibration and 3D reconstruction," in *The OpenCV Reference Manual*, April 21 2014, pp. 379,390.
- [18] R. Laganiere, "Estimating Projective Relations in Images," in *OpenCV 2 Computer Vision Application Programming Cookbook*, Birmingham, Packt Publishing Ltd., May 2011, p. 226.
- [19] G. Bradski and A. Kaebler, "Computer Vision with OpenCV Library," in *Learning OpenCV*, Sebastopol, O'Reilly Media, Inc., September 2008, p. 382.
- [20] J. Kohler, A. Pagani and D. Stricker, in *Visualization of Large and Unstructured Data Sets – Applications in Geospatial Planning, Modeling and Engineering*, OASIS, April 2011, pp. 36-44.
- [21] F. Penski, "Charakterisierung von Spiegeln für solarthermische Kraftwerke," Freiburg, 2014.

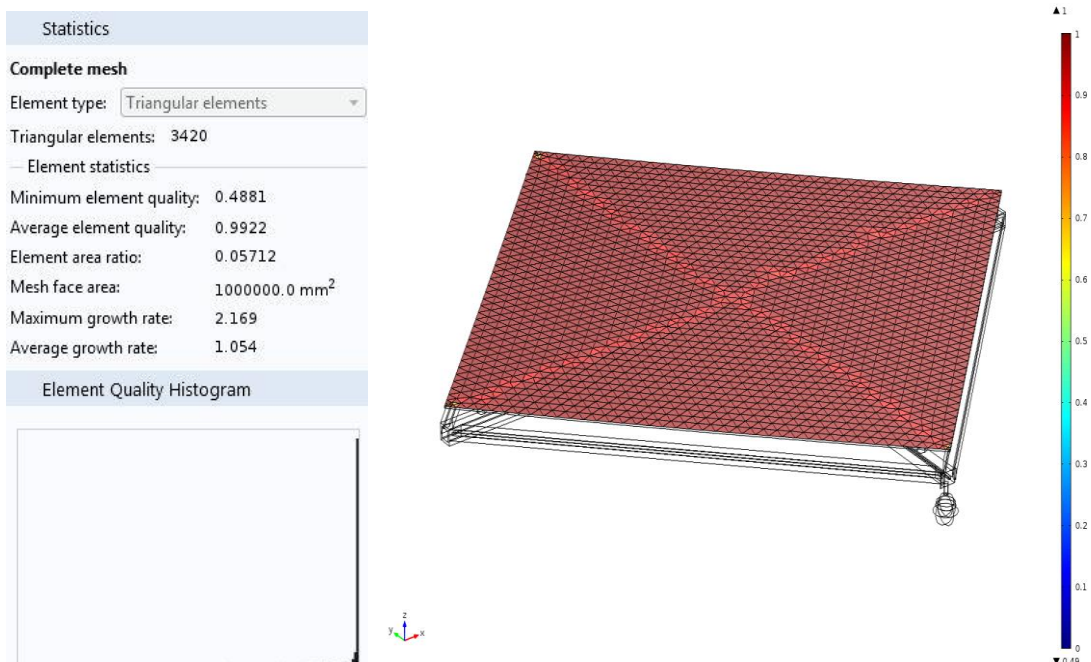
Addendum



Property	Name	Value	Unit
✓ Density	rho	7850[kg/...	kg/m ³
✓ Young's modulus	E	205e9[Pa]	Pa
✓ Poisson's ratio	nu	0.28	1
Relative permeability	mur	1	1
Electrical conductivity	sigma	4.032e6[...	S/m
Coefficient of thermal expansion	alpha	12.3e-6[1...	1/K
Heat capacity at constant pres...	Cp	475[J/(kg...	J/(kg-K)
Relative permittivity	epsilononr	1	1
Thermal conductivity	k	44.5[W/(...	W/(m-K)

Property	Name	Value	Unit
✓ Density	rho	2203[kg/...	kg/m ³
✓ Young's modulus	E	73.1e9[Pa]	Pa
✓ Poisson's ratio	nu	0.17	1
Relative permeability	mur	1	1
Electrical conductivity	sigma	1e-14[S/...	S/m
Coefficient of thermal expansion	alpha	0.55e-6[1...	1/K
Heat capacity at constant pres...	Cp	703[J/(kg...	J/(kg-K)
Relative permittivity	epsilononr	2.09	1
Thermal conductivity	k	1.38[W/(...	W/(m-K)
Refractive index	n	1.45	1
Refractive index, imaginary part	ki	0	1

Addendum 1: Model builder tree with definition of parameters used materials



Statistics

Complete mesh

Element type:

Triangular elements: 3420

— Element statistics

Minimum element quality: 0.4881

Average element quality: 0.9922

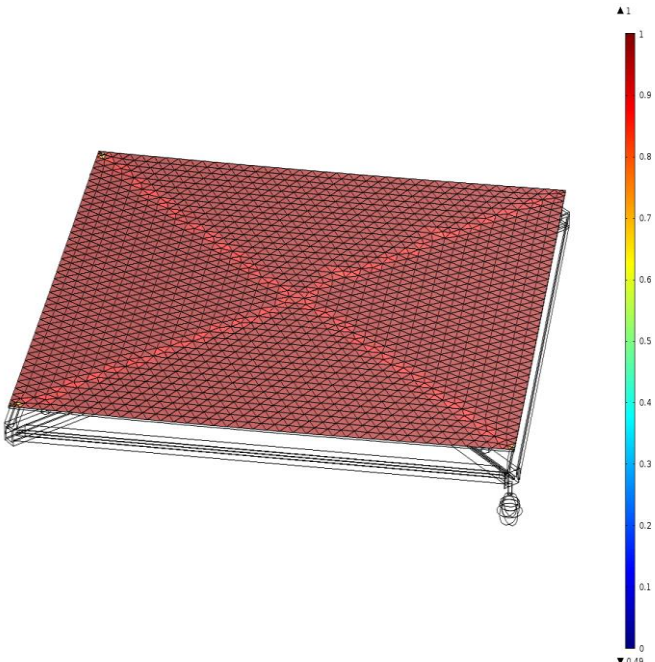
Element area ratio: 0.05712

Mesh face area: 1000000.0 mm²

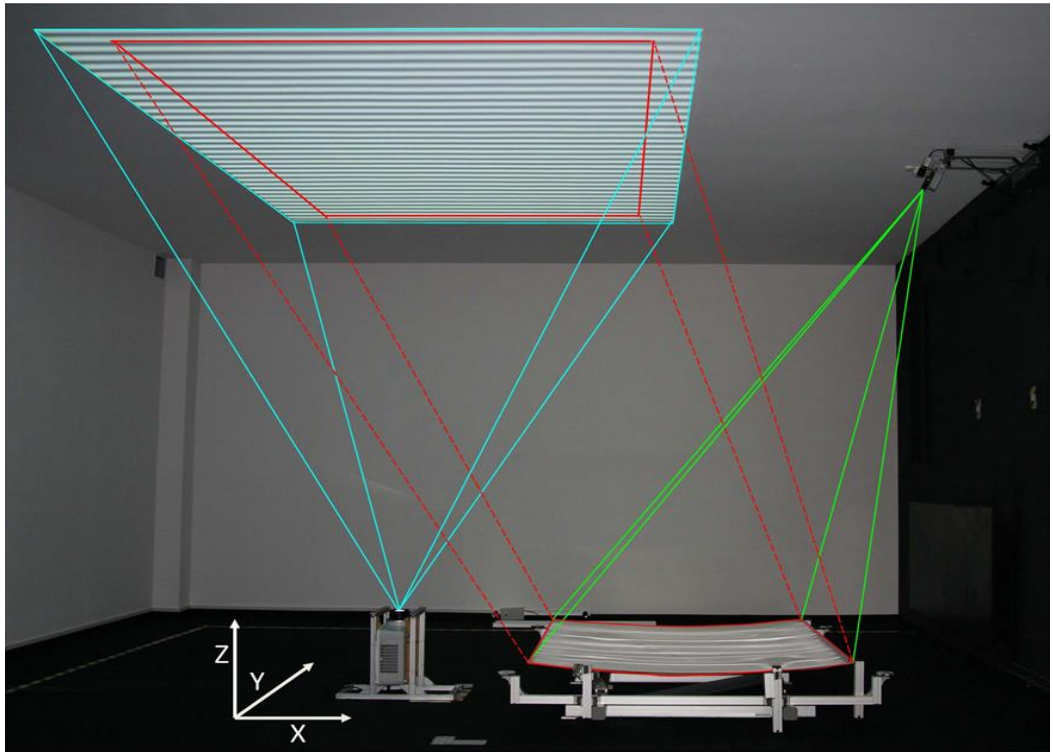
Maximum growth rate: 2.169

Average growth rate: 1.054

Element Quality Histogram



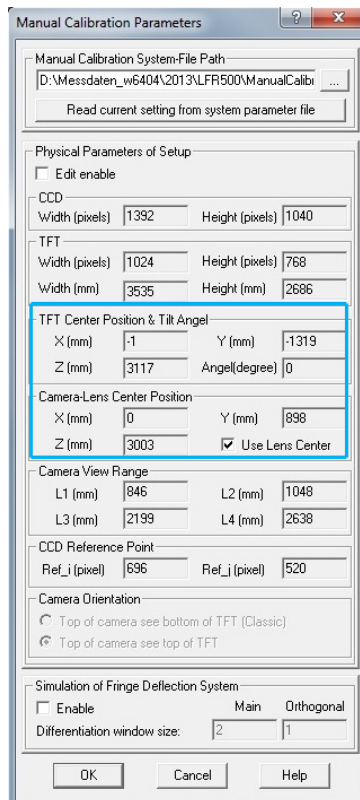
Addendum 2: Mesh statistics (left) of the heliostat surface (right)



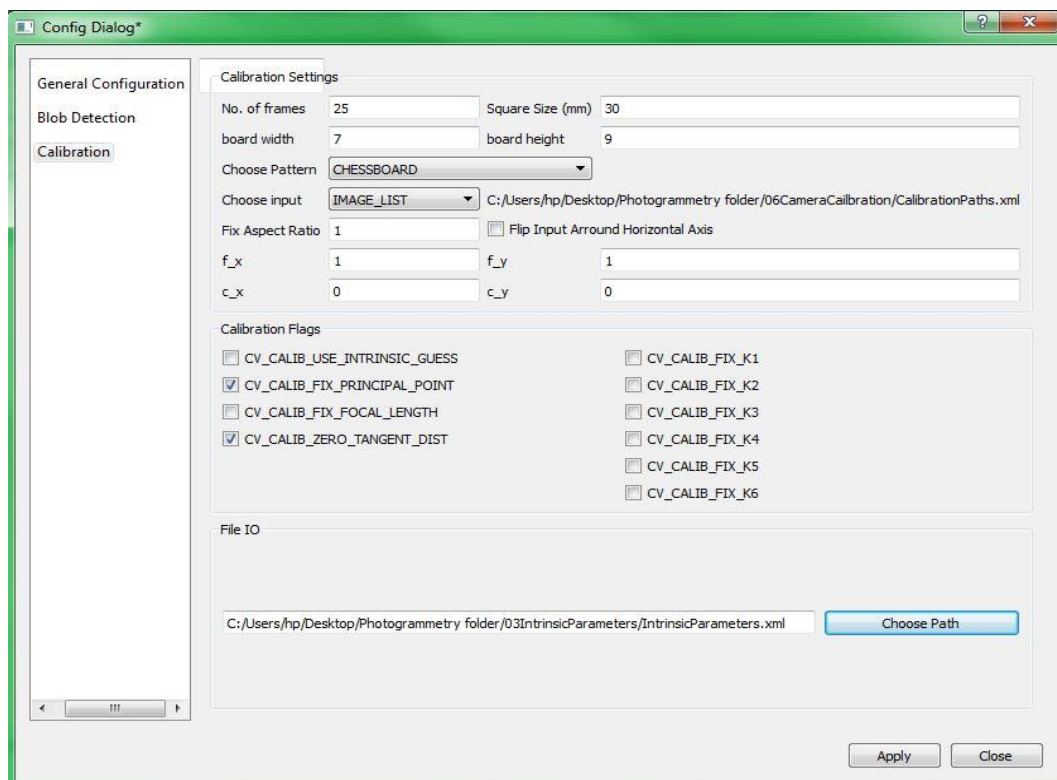
Addendum 3: Visualization of segment of sinusoidal pattern through the mirror
[21]



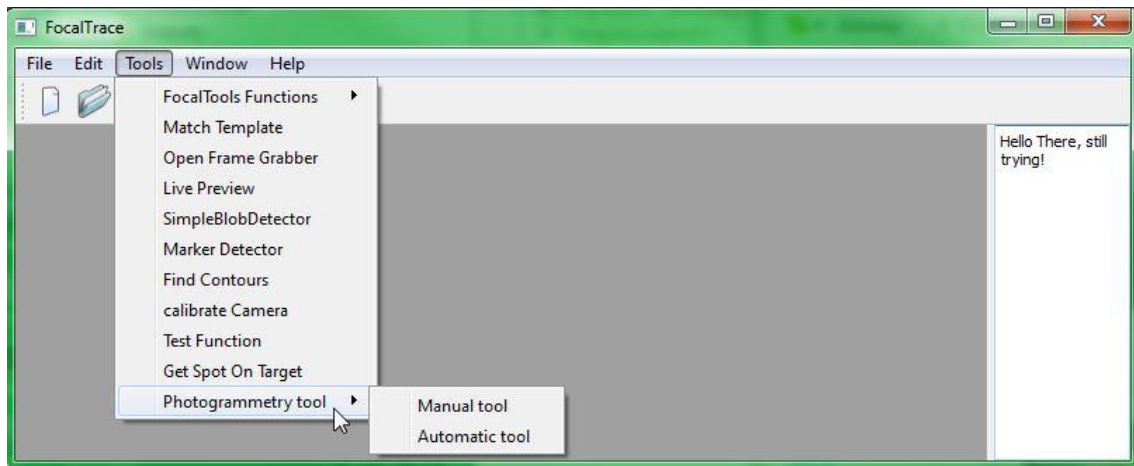
Addendum 4: Total station device (left) with remote controller (right)



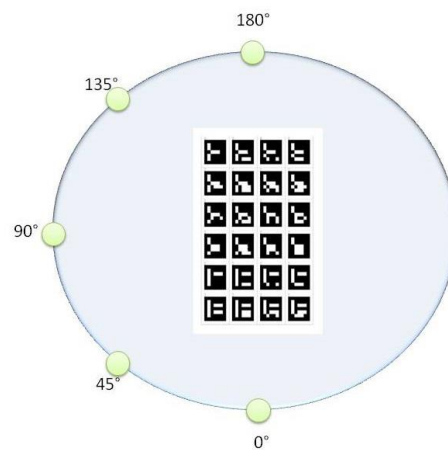
Addendum 5: Calibration settings in Fringe Processor software. (TFT expresses the position of center point of the fringe pattern) [21]



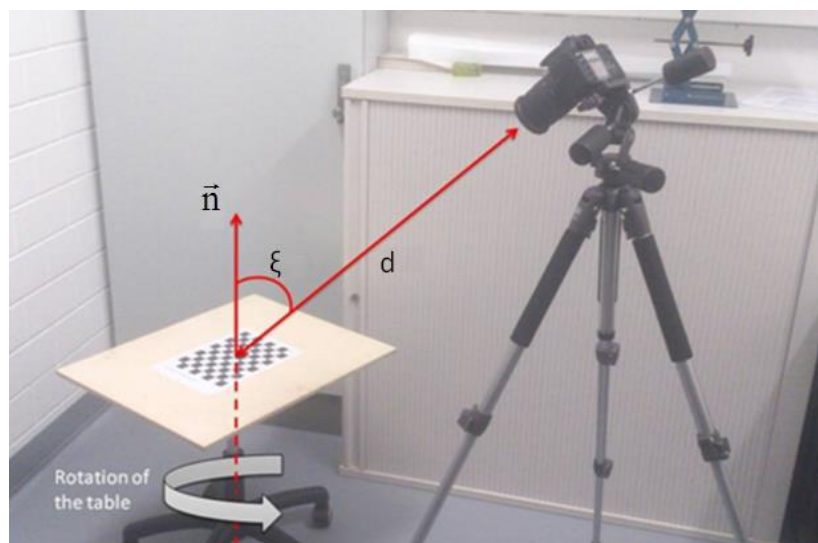
Addendum 6: Camera calibration settings



Addendum 7: Graphical user interface with photogrammetry tool submenu



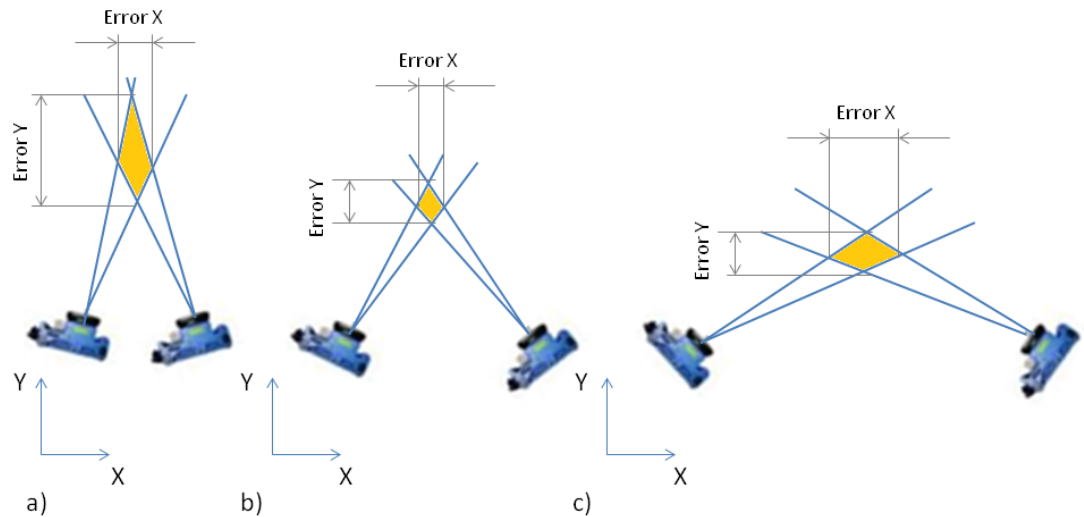
Addendum 8: Positions of the camera relative the target. Pairs of images composed relative position with zero angle is tested



Addendum 9: Camera position with respect to incident angle ξ and distance to the target d

Parameter	Value, unit	Maximal error, mm
Number of images	2	1,9895
	3	1,9895
	4	2,0933
	5	2,1885
	6	2,2231
	7	2,0328
	8	2,2577
	9	2,4134
	10	2,4047
	11	2,3009
	12	2,1625
	13	2,0241
	14	1,8944
	15	1,8165
	16	1,7819
	Incident angle	15°
30°		-
45°		1,7819
60°		1,8598
75°		0,7872
Distance to the target	500 mm	5,2506
	1500 mm	5,8474
Number of references	4	3,9704
	8	2,6037
	12	1,2629
	16	1,3148
	20	0,6747
Distribution of references	Uniform	3,9704
	Non-uniform	4,0569
SolvePnP method	EPNP	0,6747
	ITERATIVE	0,6055
Geometric layout	45°	1,6435
	90°	1,4273
	135°	1,3148
	180°	1,1418

Addendum 10: *Table of measurement results of implemented photogrammetry technique. Green row indicates the best result achieved with use of ITERATIVE perspective-n-point method*



Addendum 11: a) Narrow, b) medium and c) wide geometric layout

Index	Central tube		Horizontal tube		Upper diag. tube		Lower diag. tube	
	W, mm	T, mm	W, mm	T, mm	W, mm	T, mm	W, mm	T, mm
1	30,0	5,0	30,0	5,0	26,5	3,5	26,5	3,5
2	30,0	5,0	30,0	5,0	26,5	3,5	22,5	3,5
3	30,0	5,0	30,0	5,0	22,5	3,5	22,5	3,5
4	30,0	5,0	26,5	3,5	22,5	3,5	22,5	3,5
5	30,0	5,0	26,5	3,5	22,5	3,5	22,5	5,6
6	30,0	5,0	26,5	5,0	22,5	5,6	22,5	3,5
7	30,0	5,0	26,5	5,0	22,5	3,5	22,5	3,5
8	30,0	5,0	26,5	3,5	22,5	5,6	22,5	5,6
9	30,0	5,0	26,5	5,0	22,5	3,5	22,5	5,6
10	30,0	5,0	26,5	5,0	22,5	5,6	22,5	3,5
11	30,0	5,0	26,5	5,0	20,0	2,0	22,5	3,5
12	30,0	5,0	26,5	5,0	22,5	3,5	20,0	2,0

Addendum 12: Set of dimensions of the tubes used in optimization procedure.

Symbol W is a width of the tube, T – tube thickness

Index	Z_1/Z_1	Z_2/Z_1	Z_3/Z_1	Z_4/Z_1	$\sigma_{sd,x} (65^\circ)$, mrad	$\sigma_{sd,y} (65^\circ)$, mrad	$\sigma_{sd,x} (5^\circ)$, mrad	$\sigma_{sd,y} (5^\circ)$, mrad
1	1	1	0,61	0,61	2,4439	2,9372	1,5308	4,2807
2	1	1	0,61	0,41	2,4441	2,9390	1,4866	4,3992
3	1	1	0,41	0,41	2,3488	2,9103	1,4937	4,4161
4	1	0,61	0,41	0,41	2,2353	3,1574	1,4087	4,2045
5	1	0,61	0,41	0,50	2,1829	3,1525	1,4004	4,2182
6	1	0,72	0,50	0,41	2,2874	3,1694	1,4397	4,2451
7	1	0,72	0,41	0,41	2,1943	3,1538	1,3962	4,2037
8	1	0,61	0,50	0,50	2,2371	3,1692	1,4310	4,2515

9	1	0,72	0,41	0,50	2,1357	3,1552	1,3872	4,2100
10	1	0,72	0,50	0,41	2,2502	4,2100	1,4276	4,2309
11	1	0,72	0,26	0,41	2,0382	3,1322	1,3245	4,2279
12	1	0,72	0,41	0,26	2,3110	3,1758	1,4092	4,2019

Addendum 13: *Standard deviations at extreme points (angle of incidence) with respect to cross-sectional modules ratio*

Index	d₁, mm	$\sigma_{sd,x}$ (65°), mrad	$\sigma_{sd,y}$ (65°), mrad	$\sigma_{sd,x}$ (5°), mrad	$\sigma_{sd,y}$ (5°), mrad	Maximal, mrad	Average, mrad
1	5	2,1208	8,1098	4,8699	6,8421	8,1098	5,4857
2	10	2,1069	6,2007	3,9875	8,1098	8,1098	5,1012
3	15	2,0855	4,5941	2,3043	6,8245	6,8245	3,9521
4	20	2,0382	3,1322	1,3245	4,2279	4,2279	2,6809
5	25	2,0084	2,0905	1,4612	5,9446	5,9446	2,8761
6	30	2,0274	2,0509	1,4845	7,2070	7,2070	3,1925
7	40	1,9847	4,7582	1,5798	9,7844	9,7844	4,5268

Addendum 14: *Standard deviations at extreme points with respect to distance of rotation bar to the center of central tube*

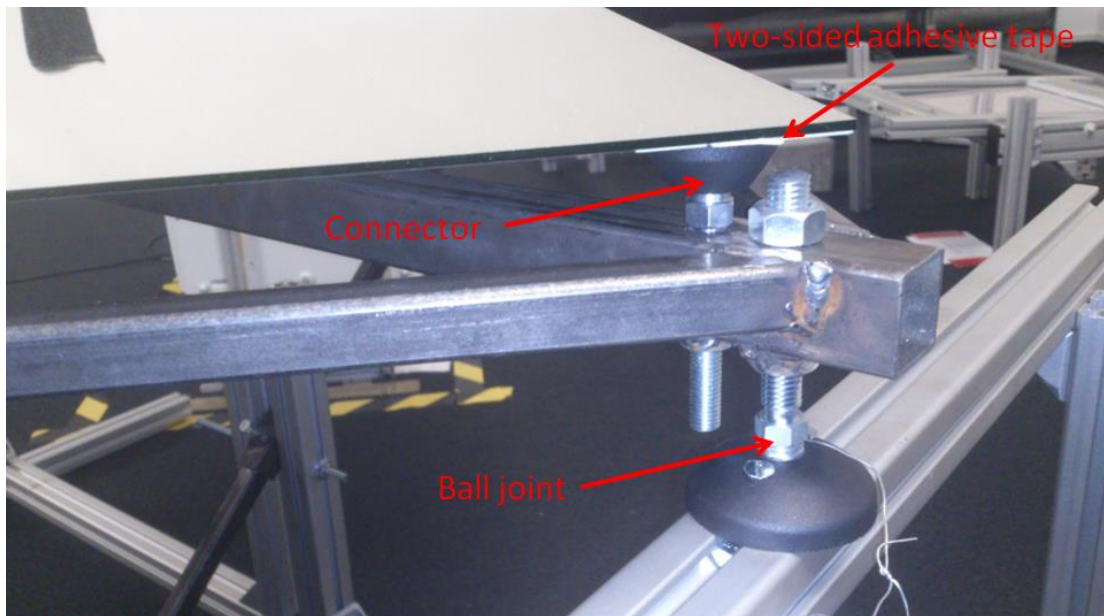
Index	d₂, mm	$\sigma_{sd,x}$ (65°), mrad	$\sigma_{sd,y}$ (65°), mrad	$\sigma_{sd,x}$ (5°), mrad	$\sigma_{sd,y}$ (5°), mrad	Maximal, mrad	Average, mrad
1	-5	1,8531	3,4788	1,3290	4,8280	4,8280	2,8722
2	0	2,0382	3,1322	1,3245	4,2279	4,2279	2,6807
3	5	2,2777	2,8417	1,5448	4,5238	4,5238	2,7970
4	10	2,5080	2,6892	1,6402	4,3566	4,3566	2,7985
5	15	2,6646	2,5338	1,7760	4,3566	4,3566	2,8327

Addendum 15: *Standard deviations at extreme points with respect to distance between joint and rotation bar height level*

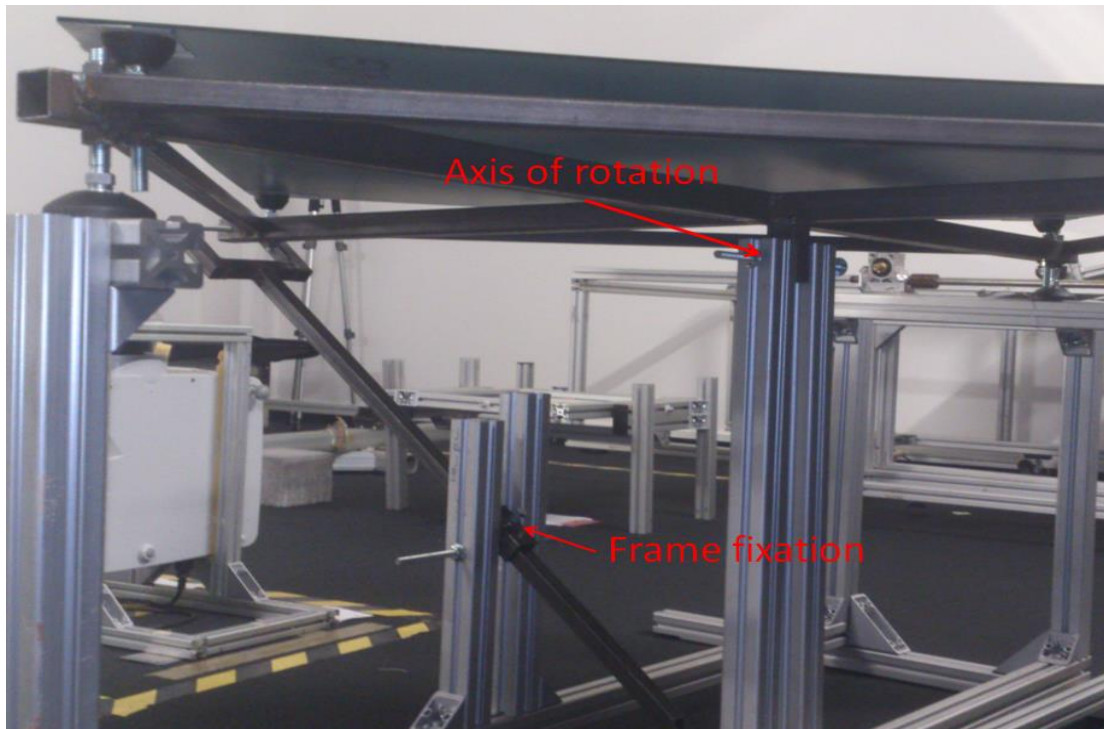
Number of connectors	L₁, mm	L₂, mm	σ_x (65°), mrad	σ_y (65°), mrad	σ_x (5°), mrad	σ_y (5°), mrad
4	265,17	265,17	1,6164	8,4456	0,8805	0,3368
	441,94	441,94	0,8343	6,9470	0,5280	1,1850
	618,72	618,72	1,0730	5,9103	0,7339	1,7875
	662,91	662,91	0,9079	5,8311	0,5503	1,7137
	618,72	265,17	2,2291	3,2842	1,2094	3,9304

	618,72	441,94	1,3193	4,4870	0,7591	3,0423
	441,94	618,72	0,6384	7,7543	0,4169	0,5861
	441,94	265,17	1,8338	5,6540	0,9805	2,4503
	265,17	441,94	1,2130	9,0546	0,7868	0,5374
	265,17	618,72	1,3336	8,9398	0,7672	0,4879
5	265,17	265,17	1,9682	8,0068	1,2474	0,5683
	441,94	441,94	1,8911	5,2215	1,2131	2,9742
	618,72	618,72	2,0382	3,1322	1,3245	4,2279
	662,91	662,91	2,0377	3,1335	1,2847	4,2350
	618,72	265,17	2,5300	3,0462	1,6046	4,2675
	618,72	441,94	2,1267	3,1255	1,3329	4,2322
	441,94	618,72	1,7491	5,1826	1,1634	3,0580
	441,94	265,17	2,3317	5,1553	1,5125	3,0355
	265,17	441,94	1,6429	7,9986	1,1609	0,5978
	265,17	618,72	1,7713	8,0679	1,1711	0,5409

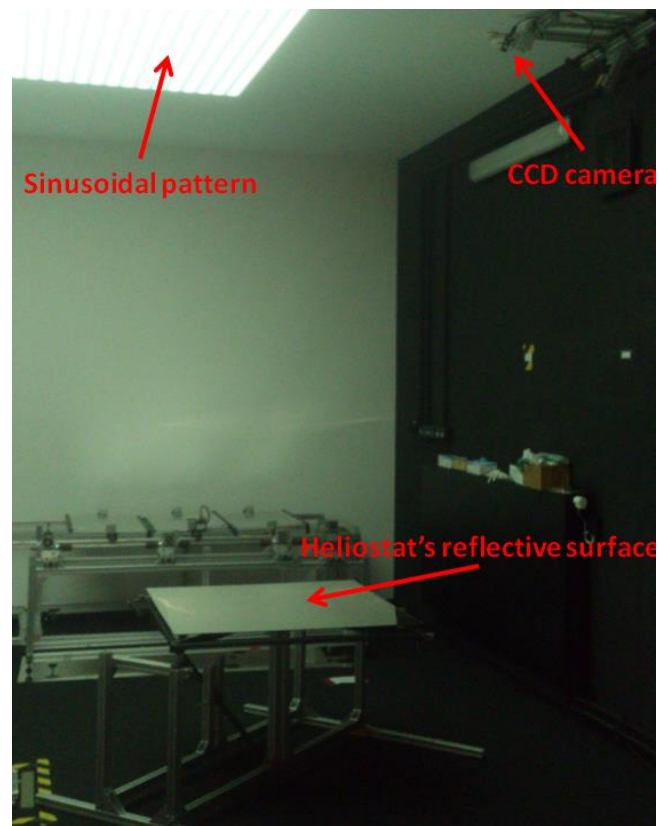
Addendum 16: *Standard deviations at extreme points with respect to connector's layout*



Addendum 17: *Connection of mirror, frame and stand of the heliostat*



Addendum 18: *Fixation of heliostat's frame in inclined position*



Addendum 19: *Deflectometry measurement setup with heliostat prototype*



Addendum 20: *Example of photographs of completely overlapping measurement. All reference markers (on the wall and locker) are visible in each image*

θ , deg	FEM model		Prototype	
	$\sigma_{sd,x}$, mrad	$\sigma_{sd,y}$, mrad	$\sigma_{sd,x}$, mrad	$\sigma_{sd,y}$, mrad
23	0,1594	0,2108	2,7101	2,4672
30	0,0301	0,0273	2,8639	2,5850
38	0,1550	0,1628	2,8837	2,7319

Addendum 21: *Standard deviation of the heliostat specular surface of FEM model and heliostat prototype with FRT validation*

θ , deg	Theoretical surface with deformation		Theoretical surface without deformation		FEM simulated surface		FRT measured surface (prototype)	
	F_{sagit} , m	F_{tang} , m	F_{sagit} , m	F_{tang} , m	F_{sagit} , m	F_{tang} , m	F_{sagit} , m	F_{tang} , m
5	20,0034	20,0032	17,3896	23,0078	24,2711	20,2751	-	-
23	20,0033	20,0021	21,2597	20,0021	20,4735	20,0413	20,3891	20,9003
30	20,0033	20,0015	20,0033	20,0015	20,0021	20,0003	20,9401	21,1157
38	20,0033	20,0008	21,9837	18,1997	20,2500	19,9978	21,6029	20,1034
65	20,0033	20,0039	40,9907	9,7607	31,5673	18,2679	-	-

Addendum 22: *Effective focal lengths of numerically calculated (theoretical), FEM simulated and FRT measured surfaces*